

# 論文要旨

光通信においてこれまで活用されていたガラス材料の素子を，シリコン材料の素子で置き換えようとする研究分野をシリコンフォトニクスと呼ぶ．シリコンはガラスよりも高屈折率で光をより強く閉じ込めるため，シリコンフォトニクスを活用することで素子面積を小さくできる．またシリコンを加工する技術はパソコンなどにも用いられる電子素子の発展と共に成熟しており，その技術を転用できる．シリコンの加工技術には大きく2つの方法があり，1つ目はフォトリソグラフィと呼ばれるものだ．フォトリソグラフィは電子素子作製において主に使用される方法で，CMOS プロセスと呼ばれることもある．2つ目は電子線描画と呼ばれる加工方法で，作製精度は高いものの時間と費用がフォトリソグラフィと比較して多くかかってしまうのが問題点である．この修士論文は，シリコンフォトニクスの中で注目を集める一つの素子構造であるフォトニック結晶についての研究をまとめたものである．フォトニック結晶の中でもフォトリソグラフィで作製されたものについて，その実用性という観点を考慮しながら研究を進めた．

第1章ではフォトニック結晶について説明をする．構造にナノメートルオーダーの周期構造を持つのがフォトニック結晶の特徴で，通常のシリコンフォトニクスの素子よりも光をさらに強く閉じ込めることができ，素子面積を小さくすることが可能である．多くの研究がこのフォトニック結晶に対しても行われており，これらの変遷と課題抽出を行う．

第2章ではフォトニック結晶の理論について述べる．

第3章ではフォトリソグラフィによるフォトニック結晶作製方法を説明し，作製精度を評価する．

第4章では作製誤差の制御と活用というテーマについてフォトニック結晶線欠

陷導波路を用いた成果について報告する．ここでは作製誤差由来の光の閉じ込め現象を空間的・確率的に制御して，最終的に最大 1 GHz の光・電気変調実験を示す．

第 5 章では光機能集積素子の一つとしてフォトニック結晶で波長分波器を実現した成果について取り上げる．ここでは熱による波長チューニングや最大 2.5 Gbps の伝送実験を示し，クロストークを低減する設計指針についても述べている．

第 6 章では本論文の結論を述べる．

# Thesis Abstract

Optical communication has been changing our life. At the beginning of the Internet, it used telephone band at the speed of kHz. Telephone band communication had been replaced with optical communication that works at a couple of 100 THz range. When optical communication started, it was limited only in the long haul large server connection. As personal computers and smart phones have been prevailing, however, optical communication has been intruding into our daily life, and traffic on the optical communication has been expanding exponentially. Small and cost effective optical devices are required in the recent situation.

Silicon photonics is the name of a research field where conventional glass optical devices are replaced with silicon ones. Silicon has higher refractive index in optical communication band and confines light more tightly than glass, which realizes smaller optical devices. Silicon has been used as a material for electronics, and the fabrication process has been matured. Silicon photonic devices have been developing quickly due to the fabrication process. The fabrication process of silicon photonic devices can be categorized in two main technologies. The first one is called photolithography. This is the technology that is also used in the fabrication of electronic devices mainly, which is usually referred as complementary metal–oxide–semiconductor (CMOS) process. The second one is electron-beam (EB) lithography. This fabrication technology is mostly used in silicon photonic devices that need better precision in their structure than electronic devices does. EB lithography is better in precision but more expensive and time-consuming than photolithography. As one of silicon photonic devices, photonic crystals (PhCs) have been investigated. When it comes to fabrication process of PhCs, EB lithography has been mainly used. This is because its precision is required for the small size of PhCs. The fabrication process of PhCs is not compatible with other silicon photonic devices, and this is problematic when considering to apply PhCs to optical

communication.

In this thesis, PhCs fabricated with photolithography is demonstrated. Their application possibility is taken into consideration.

Chapter 1 introduces studies of PhCs and extracts their problems. The size of PhCs is very small and they show interesting phenomena that have been attracting many researchers, recently.

Chapter 2 explains the theory on PhCs.

Chapter 3 describes the procedure of photolithography during PhC fabrication. Fabricated PhCs are investigated through SEM measurement.

Chapter 4 investigates randomness in PhCs using PhC line defect waveguides. The way to control and utilize randomness in photonic crystals is revealed. The effect of randomness shows up in controlled area with controlled possibility. Its applicability is proven with the demonstration of an electro-optic modulator based on randomness.

Chapter 5 investigates demultiplexers based on PhCs. They are chosen to be demonstrated because demultiplexer is a device combining multi functions into a place. The design strategy for tuning transmission wavelengths and preventing crosstalk is discussed using finite-difference time-domain calculation.

Chapter 6 summarizes this thesis.



# Contents

<b>Thesis Abstract</b> .....	i
<b>Glossary of Acronyms</b> .....	vi
<b>Acknowledgments</b> .....	x
<b>Chapter 1 Introduction</b> .....	2
1.1 Milestone works in PhCs .....	3
1.2 Previous works in random PhCs .....	13
1.3 Previous works in demultiplexers on PhCs .....	16
1.4 Objective .....	19
<b>Chapter 2 Theory</b> .....	20
2.1 Optical resonators .....	20
2.2 Photonic band structure .....	23
2.3 Design strategy of high- $Q$ PhC nanocavities .....	30
2.3.1 Light cone .....	30
2.3.2 Mode profile in momentum space .....	31
2.4 FDTD calculation .....	33
<b>Chapter 3 Fabrication of two-dimensional PhCs with photolithography</b> .....	36
3.1 Introduction .....	36
3.2 Procedure of photolithography .....	37
3.3 The analysis of PhC hole diameter .....	40
3.4 Summary .....	50
<b>Chapter 4 Utilization of randomness</b> .....	51
4.1 Introduction .....	51

4.2	Model and theory to investigate randomness in PhCs.....	52
4.3	Experimental results .....	57
4.3.1	Transmission spectra & confinement area .....	57
4.3.2	Yield rate & multi-mode confinement .....	60
4.3.3	Electro-optic modulator.....	63
4.4	Summary.....	65
<b>Chapter 5</b>	<b>PhC demultiplexers .....</b>	<b>66</b>
5.1	Introduction .....	66
5.2	Design of PhC DeMUXs .....	67
5.2.1	Design and working functions.....	67
5.2.2	Resonant wavelength and $Q$ factor analysis.....	69
5.3	Results .....	70
5.3.1	DeMUX images.....	70
5.3.2	Transmission spectra & wavelength tuning .....	71
5.3.3	Eye diagram and crosstalk.....	75
5.4	Optimization of PhC DeMUXs .....	77
5.4.1	Three failed candidates for optimization.....	78
5.4.2	Succeed strategy for optimization .....	79
5.4.3	Randomness in PhC DeMUXs .....	87
5.4.4	Calculation of large number of channels.....	89
5.5	Summary.....	90
<b>Chapter 6</b>	<b>Summary .....</b>	<b>91</b>
<b>Bibliography</b>	<b>.....</b>	<b>92</b>

## Glossary of Acronyms

<b>AWG</b>	Arrayed waveguide grating
<b>CMOS</b>	Complementally metal-oxide-semiconductor
<b>DeMUX</b>	Demultiplexer
<b>EB</b>	Electron-beam
<b>EO</b>	Electro-optic
<b>FDTD</b>	Finite-difference time-domain
<b>LC</b>	Light cone
<b>LL</b>	Light line
<b>PhC</b>	Photonic crystal
<b>PBG</b>	Photonic band gap
<b>PCWG</b>	Photonic crystal waveguide
<b>HW PCWG</b>	Hetero-width photonic crystal waveguide
<b>SEM</b>	Scanning electron microscope
<b>SOI</b>	Silicon on insulator
<b>SSC</b>	Spot size converter
<b>TE</b>	Transverse electric
<b>TM</b>	Transverse magnetic
<b>TIR</b>	Total internal reflection
<b>TO</b>	Thermo-optic
<b>WDM</b>	Wavelength division multiplexing
<b>WM</b>	Width-modulated



# Chapter 1

## Introduction

The concept of PhCs spread exponentially due to the work done by E. Yablonovitch in 1987 [1], although related concepts had been found and discussed for a hundred years. In his work, it is shown that spontaneous emission can be controlled using fully periodic structure that has an electro-magnetic band gap. At the same time, S. John showed his concept of localization of photons in PhCs when certain amount of disorder is included in PhCs [2]. He mentioned that he was first informed that the very related work of E. Yablonovitch was accepted to be publish in the same volume of the same journal [3]. The word, “Photonic crystal,” was invented by two of them to make the bandgap material stick to other researchers when E. Yblonovitch visit S. John [4]. The advantage of PhCs is its tiny mode volume ( $V$ ), which means the size of PhC devices is smaller than other photonic devices. Many studies on PhCs have been developing together with fabrication technologies. All of one-, two- and three-dimensional PhCs have been investigated. Here, in this introduction, one- and two-dimensional PhCs are summarized with previous researches. Although three-dimensional PhCs were proposed originally and show a perfect band gap in all direction, applications of three-dimensional PhCs and one- and two-dimensional PhCs are not the same. These one- and two-dimensional types are highly related to this thesis, share the same fabrication process, pursue the same application fields and consist of similar structure.

## 1.1 Milestone works in PhCs

### One-dimensional PhCs

One-dimensional PhCs itself was brought into discussion by L. Rayleigh in 1887, where he took stacked multi-layer films. Today, this stacked type of one-dimensional PhCs is sometimes used for gratings; e.g. fiber Bragg gratings and grating couplers, but one-dimensional PhCs associate mainly nanobeam type. Nanobeam structure was first proposed in 1991 by D. Y. Chu, et al. and B. Meade, et al. [5,6]. The structure proposed by them was first fabricated in 1995 by P. R. Villeneuve, et al. [7]. In this paper, fabrication technique is discussed, where they employ a feasible nanobeam structure designed to work in optical communication wavelength, 1.55  $\mu\text{m}$ . Two years later, the result of optical measurement for this structure was published, where four holes were used as Bragg mirror on each side and the cavity was created with 1.5 times longer lattice constant as shown in Fig. 1.1 [8]. Experimental  $Q$  factor was 265, where  $Q$  factor is the value to evaluate the ability to confine light and is described as Eq. (1.1).

$$\begin{aligned} Q &= \omega_0 \cdot \frac{\text{Total energy stored in a cavity [J]}}{\text{Energy loss in an unit time [J/s]}} \\ &= \omega_0 \cdot \frac{U}{-\frac{dU}{dt}} \end{aligned} \quad (1.1)$$

By transforming Eq. (1.1), we can get the decay time;  $\tau_{\text{photon}}$ , when the storage energy becomes  $1/e$ .  $\tau_{\text{photon}}$  is called as photon life time.

$$\begin{aligned} \frac{dU}{U} &= -\frac{\omega_0}{Q} dt \\ U &= U_0 e^{-\frac{t}{\tau_{\text{photon}}}} \\ \therefore Q &= \omega_0 \cdot \tau_{\text{photon}} \end{aligned} \quad (1.2)$$

There is another definition for  $Q$  factor shown in Eq. (1.3), which is defined in the frequency range.

$$Q = \frac{\lambda_0}{\Delta\lambda_{\text{FWHM}}} \quad (1.3)$$

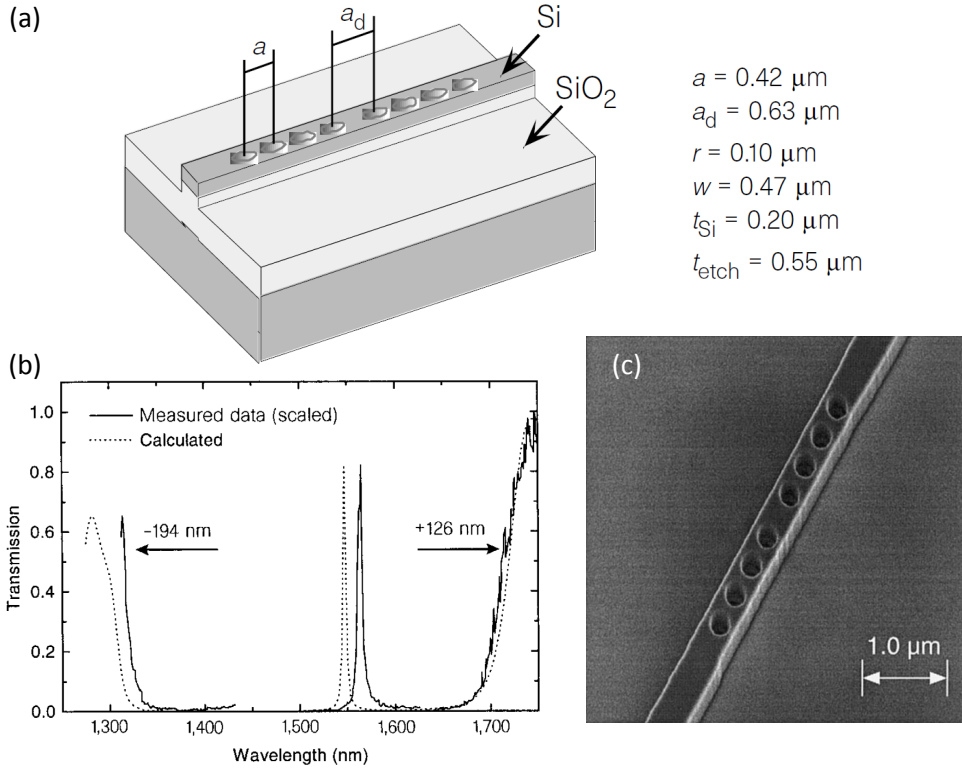


Fig. 1.1. (a) Schematic of an one-dimensional PhC waveguide microcavity with dimensions for operation at  $1.54 \mu\text{m}$ :  $a$  is the hole period,  $a_d$  is the defect length,  $r$  is the hole radius,  $w$  is the waveguide width,  $t_{\text{Si}}$  is the silicon thickness and  $t_{\text{etch}}$  is the total etch depth through both the Si and SiO<sub>2</sub>. (b) Comparison of measured transmission (solid lines) to calculated transmission (dotted line) for the structure in (a). (c) An SEM image of the fabricated structure [8] [Reprinted with permission from J. S. Foresi, P. R. Villeneuve, J. Ferrera, E. R. Thoen, G. Steinmeyer, S. Fan, J. D. Joannopoulos, L. C. Kimerling, Henry I. Smith and E. P. Ippen, “Photonic-bandgap microcavities in optical waveguides,” *Nature* **390**, 143–145 (1997).].

To evaluate a character of a cavity, there is another parameter describing what is almost similar to the size of the cavity. This is technically called mode volume,  $V$ , and the definition is shown in Eq. (1.4).

$$V = \frac{\int dV \epsilon(\mathbf{r}) |\mathbf{E}|^2}{[\epsilon(\mathbf{r}) |\mathbf{E}|^2]_{\text{max}}} \quad (1.4)$$

In the demonstration of Ref. [8],  $V$  of  $0.055 \mu\text{m}^3$  was calculated. The great feature of a nanobeam cavity is this tiny mode volume.

After the first demonstration of a PhC cavity in optical communication band with a nanobeam, various studies had been conducted theoretically and experimentally while fabrication technique had been progressing [9–11]. For example, the theoretical highest  $Q$  of more than  $10^9$  was proposed with an optimized nanobeam cavity [12]. In this paper, the optimized positions of PhC holes were considered to create Gaussian envelope of optical intensity of the cavity mode. The same discussion was first proposed in two-dimensional PhC nanocavities (this will be dealt with later in this section) [13].

PhC nanobeams have oscillation modes when they are suspended as an air-bridge structure. This mechanical oscillation caused by optical force is called opto-mechanics. Using this characteristic of a nanobeam, laser cooling is investigated in 2011 [14]. Not only from the fundamental physics side, but from the application side, was mechanical oscillation of nanobeams investigated [15,16].

## **Two-dimensional PhCs**

The history of the two-dimensional PhCs is going to be summarized below. The first modeling of two-dimensional PhCs was published in 1991 [17]. Triangle-lattice was investigated and density of the state in triangle-lattice was calculated a couple of months later [18]. The demonstration of photonic band-gap in two-dimensional PhCs was conducted at that time [19,20]. This demonstration was in microwave regime. High- $Q$  nanocavities on PhCs were first publicly mentioned by R. D. Meade, et al. from J. D. Joannopoulos's group in 1994 and theoretical aspect of PhCs, including waveguides, cavities and so on, was summarized in a book by his group, as well [21]. Two-dimensional PhCs that were intended to work in the near infrared were fabricated in 1994 [22,23] (Note that the first fabrication was presented in previous conference from another group). The experimental demonstration for these two-dimensional PhCs was conducted in 1996 and this study opened a way for PhCs where theoretical prediction can be checked experimentally. PhC nanocavities had been examined at that time, but their efficiency that can be measured as a  $Q$  factor was worse than that of microdisk cavities. In 1999, one of the milestones of PhC nanocavity design was proposed by O. Painter, et al [24]. The idea was to create a defect structure in a periodic PhC, which was a similar idea of E. Yablonovitch at the beginning of thriving of PhC studies [25]. O. Painter could

successfully transfer it into two-dimensional slab PhCs. The structure is shown in Fig. 1.2(a) and its calculated band diagram is Fig. 1.2(b).

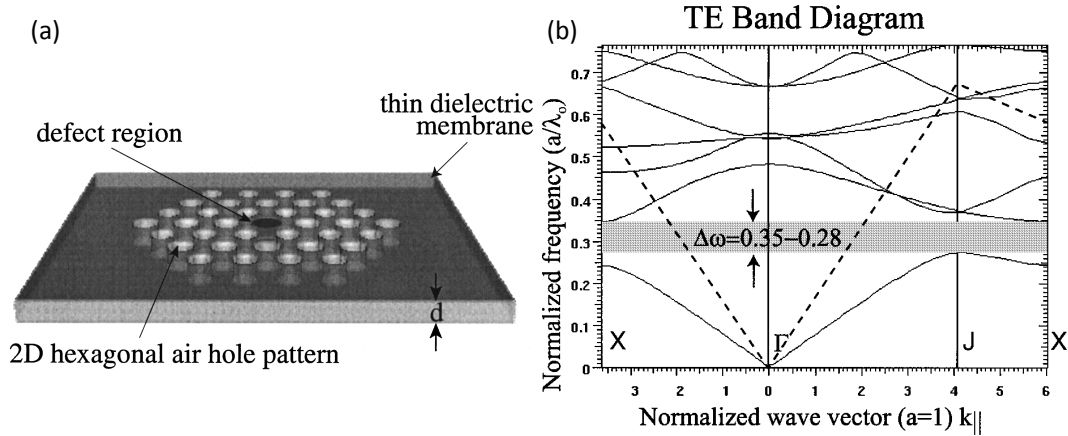


Fig. 1.2. (a) Schematic of a two-dimensional PhC nanocavity. (b) Band diagram for TE mode. The holes have an index  $n_{\text{air}} = 1$ . The material has an index  $n_{\text{slab}} = 2.65$ . The radius of the holes is defined by the ratio  $r/a = 0.3$ . The resulting TE bandgap extends between  $\Delta\omega_{\text{gap}} = a/\lambda_o = 0.28 - 0.35$  [24] [Reprinted with permission from O. Painter, J. Vučković, and A. Scherer, “Defect modes of a two-dimensional photonic crystal in an optically thin dielectric slab,” *J. Opt. Soc. Am. B* **16**, 275–285 (1999).].

Based on the PhC nanocavity design shown in Fig. 1.2(a), laser oscillation was demonstrated [26]. Indium phosphide (InP) was chosen for the PhC slab and four layers of indium gallium arsenic phosphide (InGaAsP) were stack with in the slab. InGaAsP layers work as active quantum wells. Calculated  $V$  was  $2.5 [\lambda/(2 \cdot n_{\text{slab}})]^3$ , which is corresponding to  $0.03 \mu\text{m}^3$ , where the resonant wavelength is 1509 nm. Measured  $Q$  factor was 250 and calculated one was over 1500. Fabrication technique had been improving very fast, and it became able to investigate dispersion in PhC waveguides [27]. The figures in Ref. [27] show sharp PhC holes successfully etched with the combination of electron-beam lithography and electron-cyclotron-resonance ion-stream plasma. This study is important because PhC waveguides are essential components in integrated PhC devices and a lot of researches are based on PhC waveguides. A year later, the first fabrication of PhC waveguides with photolithography was reported [28]. In this paper, the importance of photolithography is stated as “With illumination wavelengths of 248 nm or less, this technique offers both the resolution and the speed required for the mass manufacturing of PICs (photonic integrated circuits) with submicrometer features.” It can

be seen that fabrication of PhCs for mass-production started in relatively early days in the history of PhCs. The history of high- $Q$  PhC nanocavities opened with a paper in 2003 by Noda's group [29]. The strategy for pursuing high- $Q$  is investigated using L3 nanocavity (which was first named by the same group half year before [30]), which is based on how to reduce loss in a cavity. The structure of L3 nanocavities is shown in Fig. 1.3(b) and the corresponding spectra is shown in Fig. 1.3(a). They reached the conclusion that electric field with Gaussian profile is the best to reduce losses.

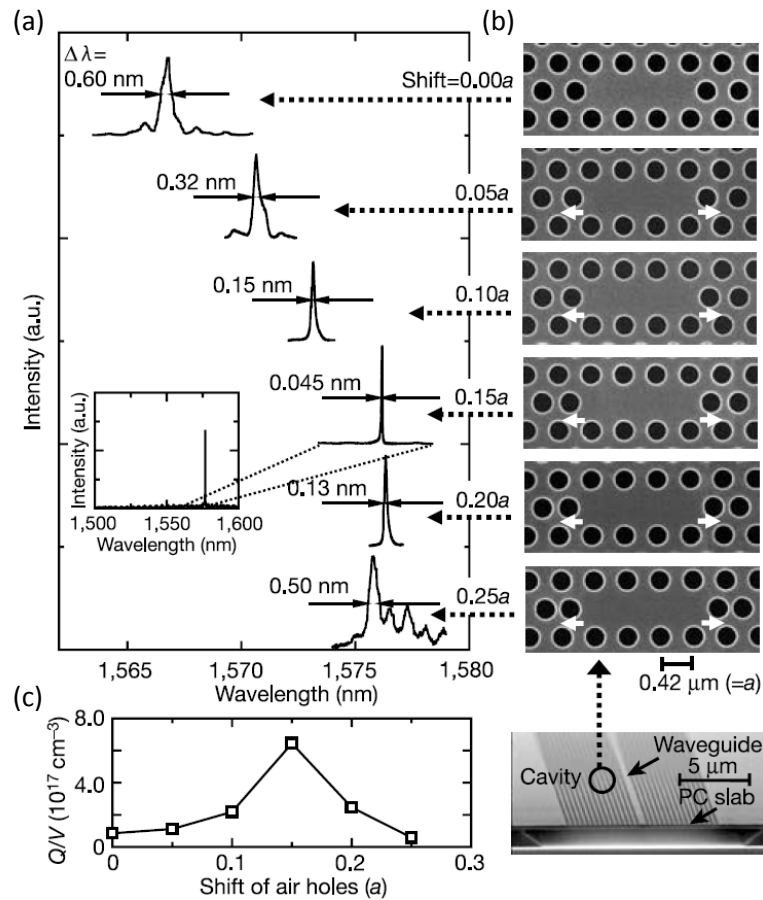


Fig. 1.3. (a), (b) Experimentally measured spectra of L3 nanocavities with various shifts of air holes and their SEM pictures, respectively. PC, photonic crystal. The inset in (a) shows the resonant spectrum of the cavity (with  $0.15a$  displacement) measured over a wide wavelength range. (c) The estimated  $Q/V$  values as a function of shift of air holes. A maximum value of  $Q/V = 6.4 \times 10^{17} \text{ cm}^{-3}$  has been realized [29] [Reprinted with permission from Y. Akahane, T. Asano, B. Song and S. Noda, "High-Q photonic nanocavity in a two-dimensional photonic crystal," *Nature* **425**, 944–947 (2003).].

Why does the electric field of a high- $Q$  PhC nanocavity have to satisfy Gaussian shape? The answer can be obtained by taking a look at Fourier transformed electric field, or  $k$ -space field. The confinement of light in the direction perpendicular to two-dimensional PhCs is achieved by total internal reflection (TIR). Light leaks when the component of wave vector at the resonant wavelength is large in the perpendicular direction. This leads to loss and low- $Q$ . Electric field and  $k$ -space are in the relation of Fourier transformation. If the  $k$ -space component inside the light cone is low, high- $Q$  PhC nanocavities can be achieved. Gaussian electric profiles has low component in light cone when it is Fourier transformed. To realize this Gaussian electric profiles, the shape of L3 nanocavity is tuned by shifting both holes at the edge of L3 nanocavity toward the outside. They investigate how affect  $Q$  factor when the amount of shift varies. From  $0.00a$  to  $0.25a$  by changing  $0.05a$ ,  $0.15a$ -shift achieves the highest  $Q$ , experimentally  $4.5 \times 10^4$ , and usually the quality of a nanocavity is evaluated  $Q/V$ , the  $0.15a$ -shifted L3 of which  $6.4 \times 10^{17} \text{ cm}^{-3}$ .  $V$  is calculated as  $0.7 (\lambda/n)^3$  in an L3 nanocavity. Since the strategy to pursue high- $Q$  had been revealed, many applicable PhC devices had been demonstrated. For instance, an all-optical PhC switch was demonstrated by T. Tanabe, et al [31]. In this research, a PhC nanocavity was formed on a PhC waveguide with a set of Grating mirrors, where those mirrors have different hole diameter to make electric field in the cavity Gaussian shape [Fig. 1.4(a)]. The cavity is L4 type and the Grating mirror has four periods on both sides. The reason why an L4 nanocavity was chosen, even though an L3 has higher  $Q$ , is that an L4 nanocavity contains two resonant modes. In this paper, resonances appear at 1530 nm and 1568 nm [Fig. 1.4(b)]. The resonant mode at longer wavelength corresponds to the fundamental mode that has higher  $Q$ , so this mode was chosen for signal and the other mode at shorter wavelength was chosen for control in the all-optical switching demonstration. This is because higher  $Q$  leads to narrower linewidth and is beneficial for larger contrast in switching demonstration. As a result, this PhC nanocavity based all-optical switching achieved a few hundred times smaller energy consumption and about ten times faster demonstration than those of a previous study based on a bulk silicon [32].

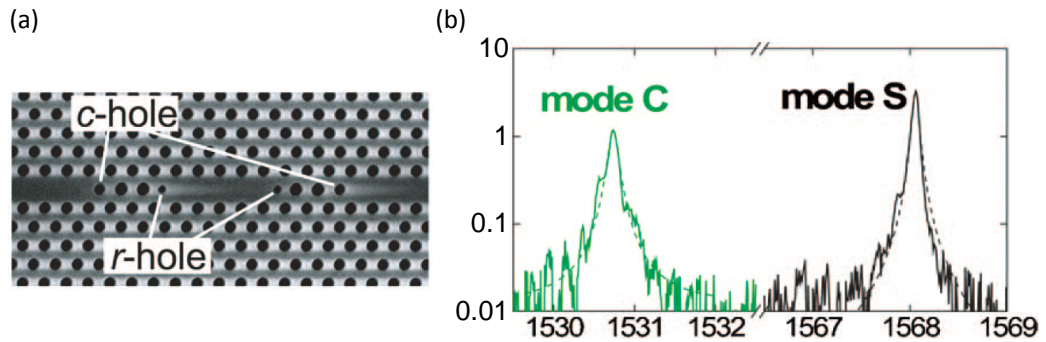


Fig. 1.4. (a) SEM image of a sample employed for the experiment. Lattice constant is  $a = 420$  nm with a hole diameter of  $d = 0.55a$ . (b) Experimental transmission spectrum of an L4 nanocavity with resonant modes at  $\lambda_{c0} = 1530.47$  nm ( $\Delta\lambda_c = 133$  pm,  $Q_c = 11500$ , and  $\tau_{cp} = 9.3$  ps) and  $\lambda_{s0} = 1568.05$  nm ( $\Delta\lambda_c = 68$  pm,  $Q_c = 23000$ , and  $\tau_{cp} = 19.1$  ps). The diameters of  $c$ - and  $r$ -holes are  $0.45a$  and  $0.3a$ . The  $r$ -holes are 60 nm shifted toward the  $c$ -holes direction [31] [Reprinted with permission from T. Tanabe, M. Notomi, S. Mitsugi, A. Shinya and E. Kuramochi, “All-optical switches on a silicon chip realized using photonic crystal nanocavities,” *Appl. Phys. Lett.* **87**, 151112 (2005).].

Until at the beginning of 2005, all PhC nanocavity designs were acceptor type or donor type, but a different type of a PhC nanocavity was proposed by Noda’s group, which is called mode-gap nanocavity [33]. Previous acceptor and donor type used a defect mode within a photonic band gap and confined light with surrounding band-gap, called band-gap nanocavity. On the other hand, a mode-gap nanocavity is formed with different parts of PhCs that are different in lattice constant or waveguide width, and this nanocavity structure is a combination of different waveguide modes corresponding to each parts. At certain wavelength, light can only exist in a certain part because of that difference in waveguide modes, so this nanocavity design can confine light. This system to confine light is based on the difference in waveguide modes, which is the reason why it is called mode-gap nanocavity. An example of band diagrams of a mode-gap nanocavity is shown in Fig. 1.6.  $Q$  of a PhC mode-gap nanocavity in Ref. [33] is  $6 \times 10^5$  experimentally, which is mainly limited by accuracy in fabrication, whereas calculation shows  $Q$  of  $2 \times 10^7$  theoretically. Another mode-gap type PhC nanocavity was proposed next year, called a width-modulated line defect nanocavity [34]. As this width-modulated line defect nanocavity is mode-gap type, this consists of different PhC parts with different

waveguide modes. The mode-gap in this nanocavity is realized with the difference of waveguide width, where PhC holes at the center of a waveguide are slightly shifted toward the outside to make waveguide width wider. The detail configuration is shown in Fig. 1.5. Theoretical  $Q$  factor and  $V$  in Ref. [34] is  $7 \times 10^7$  and  $1.7 (\lambda/n)^3$ , respectively. Experimental unladen  $Q$  is  $9 \times 10^5$ .

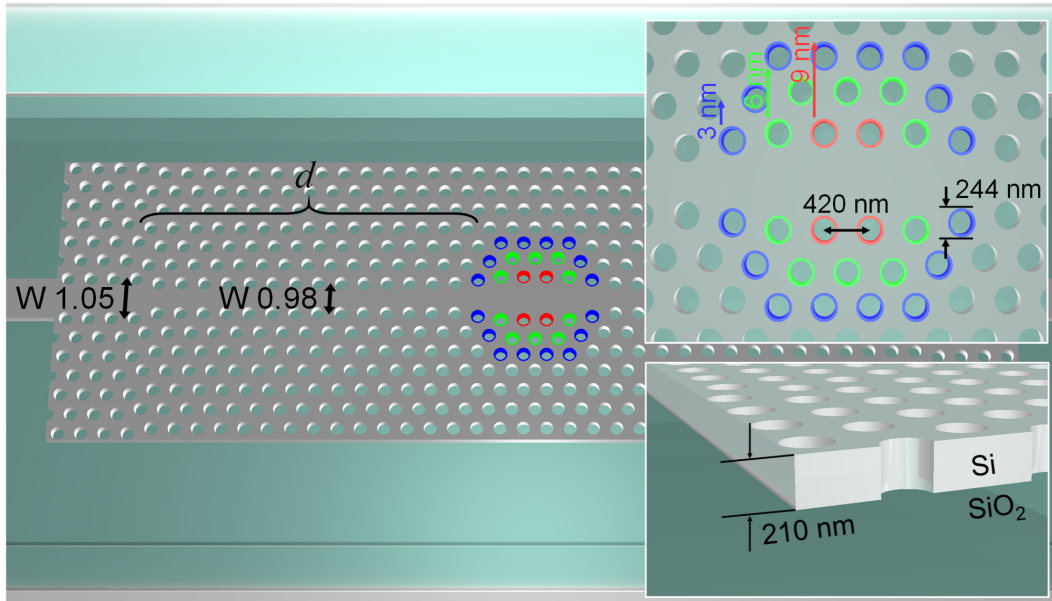


Fig. 1.5. Schematic illustration of a two-dimensional width-modulated line defect PhC nanocavity. Air holes only at the centre of the structure are slightly shifted toward the outside of the waveguide from their original position. The silicon slab is covered with SiO<sub>2</sub>.  $d$  is the number of barrier holes that set the strength of coupling and confinement. As a barrier region, W0.98 PhC waveguide is used [35] [Reprinted with permission from Y. Ooka, T. Tetsumoto, A. Fushimi, W. Yoshiki, and T. Tanabe, "CMOS compatible high-Q photonic crystal nanocavity fabricated with photolithography on silicon photonic platform," *Sci. Rep.* **5**, 11312 (2015).].

A band diagram of a width-modulated line defect nanocavity is shown in Fig. 1.6, where the hole diameter is 246 nm and silicon PhC is surrounded by silica. In Fig. 1.6, a band diagram of a W0.98 waveguide is drawn in a red line and that of a waveguide whose width is same as the region of 9-nm shift in a width-modulated line defect nanocavity is drawn in a red broken line. Photonic band-gap is corresponding to from  $0.242 (a/\lambda)$  to  $0.280 (a/\lambda)$  and a band with higher frequency within the photonic band-gap is TE mode and lower one is TM mode. In Ref. [35], TE mode was used, and there was slight

difference in the cut-off frequency of TE mode between a W0.98 waveguide and a cavity. This difference enable a nanocavity shown in Fig. 1.5 to confine light at a cavity. Those two studies revealed that mode-gap type have higher- $Q$  than band-gap type.

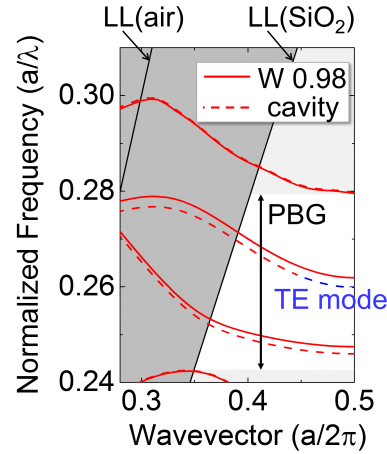


Fig. 1.6. Dispersion of a two-dimensional PhC waveguide (line defect) with SiO<sub>2</sub> cladding. The light line (LL) for both the air and SiO<sub>2</sub> claddings are shown in the graphs. The solid line is the dispersion of the W0.98 waveguides (without cavity hole shifts) that we use as barriers. The dashed line is when the waveguide width is 18 nm wider (with cavity hole shifts) than the barrier waveguide, which corresponds to the width of a W1 waveguide [35] [Reprinted with permission from Y. Ooka, T. Tetsumoto, A. Fushimi, W. Yoshiki, and T. Tanabe, "CMOS compatible high- $Q$  photonic crystal nanocavity fabricated with photolithography on silicon photonic platform,"

Although  $V$  of mode-gap PhC nanocavities is about twice as that of band-gap PhC nanocavities,  $Q$  factor of mode-gap nanocavities is about two order of magnitudes higher. The fundamental strategy to pursue high- $Q$  using mode-gap PhC nanocavities is same as when using band-gap PhC nanocavities. An optimized structure in a mode-gap PhC nanocavity was investigated, and it was proposed that five different parts with different lattice constants called a multi-hetero structure, realizes nice Gaussian electric field and that theoretical  $Q$  and  $V$  reach  $7 \times 10^8$  and  $1.3 (\lambda/n)^3$  [13]. Low energy consumption and fast all-optical switching was demonstrated in 2010 [36]. In this paper, a mode-gap type H0 PhC nanocavity was chosen because the demonstration aimed fast recovery time that is defined as Eq. (1.2). If switching recovery time of 50 ps is wanted at 1550 nm, loaded  $Q$  of less than  $10^4$  is required. The demonstration uses loaded  $Q$  and calculated  $V$  of

$6.5 \times 10^3$  and  $0.26 (\lambda/n)^3$ , respectively, and it uses the change in refractive index as the driver of switching. The structure employs InGaAsP for a PhC slab because this material has a hundred times higher coefficient of two photon absorption (TPA) and refractive index change depending on density of carriers generated by TPA. These choices of nanocavity design and material enabled to demonstrate all-optical switching with energy consumption of less than 1 fJ and speed of 20 ps at minimum. In 2011, a very low threshold PhC laser source was invented, which was pumped not optically but electrically. *p*- and *n*-doped regions were fabricated upper and lower part of an L3 nanocavity. It achieved a few order of magnitudes of less threshold due to high  $Q$  of 1130, compared with traditional quantum-well lasers. At that time, there had been lasing sources with systems extracting or injecting carriers or with gain materials inside silicon. There had not been any pure silicon lasing devices. Not until a multi-hetero PhC nanocavity demonstrated laser oscillation in 2013 did an all silicon device demonstrate an all-optical laser [37]. This device demonstrates Raman lasing with a multi-hetero PhC nanocavity that is well designed. The amount of Raman shift in silicon is 15.6 THz. The nanocavity is designed to have a pump mode apart from a Raman mode by that amount in frequency. Those modes correspond to odd mode and even mode in the multi-hetero structure. For pump mode,  $Q$  of  $1.04 \times 10^5$  is chosen at 1424.99 nm and for Raman mode,  $Q$  of  $1.40 \times 10^6$  is chosen at 1540.13 nm. The distance between these modes is 15.74 THz that is close enough to the theoretical Raman shift. The lasing threshold is 1  $\mu$ W and the laser efficiency is 4%. Finally, as one of milestones in the history of PhCs, we would like to mention a PhC nanocavity fabricated with photolithography. All of PhC nanocavities introduced above were fabricated with electron-beam (EB) lithography. Our motivation is to make PhC nanocavities more practical. Photolithography is fast and cost-effective, so it is a better candidate to replace EB lithography. We employed a width-modulated line defect PhC nanocavity [35] and the configuration is already shown in Fig. 1.5 as an example of same type of PhC nanocavities.  $Q$  factor of this photolithographic PhC nanocavity achieved  $2.2 \times 10^5$ .

## 1.2 Previous works in random PhCs

From the beginning of the development of PhC researches, randomness or disorder in PhCs have been attracting attention. The paper written by S. John focused on Anderson Localization in disordered dielectric structure and predicted that PhCs with moderate disorder would be the key for controllable strong localization. The condition for localization is mentioned as  $l \ll \lambda$ , where  $l$  is mean free path. As fabrication technique for PhCs developed, disorder in PhCs had been investigated theoretically. Randomness in a one-dimensional PhC was calculated and it was shown that transmittance at the band-edge decreases gently, or the band-tail grows, as the amount of randomness increases [38]. A proposal to utilize randomness for applicable devices was published with calculation, where calculation showed light diffusion provides amplification that can be used as laser source [39]. A research to define randomness in dielectric periodic structure was conducted by Yu. A. Vlasov, et al. in 1999 [40]. In their model, silica spheres with mean diameter of 197 nm were piled up and transmission was considered. It was confirmed that scattering loss became large as deviation in the diameter increased from zero to 6%. Next, as deviation became larger, around 20%, random regime showing a localized-like mode appeared, which is named as spatial confinement. The border of these two regimes, in this case 6% and 20%, is defined by a criteria whether the proportion of local shift of band-edge caused by randomness and band-edge frequency,  $\Delta v/v_0$ , is larger than the amount of randomness,  $\delta$ . If it is larger, it is in the spatial confinement regime. So far, studies on randomness had been limited in dielectric periodical structures. A study in 2005 started investigation on randomness in PhC waveguides [41]. This reflects the fact that fabrication technique of PhC waveguides was getting developed and many researches based on PhC waveguides had been published. Using Green-function-tensor formalism, propagation loss in a PhC waveguide is calculated and it is found that around the band-edge, or the regime where group velocity is slow, that loss becomes large. It is also found that the amount of loss becomes large as roughness in a PhC becomes large. The interesting thing is that at that time roughness, or randomness, was thought only as an undesirable factor in applications of PhC devices. Utilization of randomness in PhC

waveguides was studied in Ref. [42]. This was the first demonstration of light localization in semiconductor material and in optical frequency. Input light is injected via a tapered fiber into a W1 PhC waveguide with lattice constant  $a$  of 410 nm, and output light is caught above the PhC waveguide using an objective lens. Light localization was observed at 1575 nm with  $Q$  of  $3 \times 10^4$ , which meets the condition of Anderson localization [43]. From the same group, observation of the transition of localization around band-edge was reported in the same year [44]. A PhC waveguide that has pentagon holes fabricated with random direction of them was employed to examine the transition. High  $Q$  of  $1.5 \times 10^5$  was observed, and an interesting statement was given in its summary, “engineered structural disorder superimposed uniformly throughout a PhC lattice results in efficient light confinement.” It is certain that those high  $Q$  based on randomness can be useful for applications in sensing and lasing, but fabricating less precise PhCs intentionally is contradictive even though the fabrication technology can fabricate them more precise. Many researches that tackled randomness in PhC waveguides were conducted [45]. In Ref. [45], the optical low-coherence reflectometry (OLCR) technique was used to measure reflection in random PhC waveguides and it was confirmed experimentally that the amount of scattering in a PhC waveguide increases as propagating light slows. Also, the result of that experiment is enough to distinguish backscattering and out-of-plane scattering (“elastic” and “inelastic” scattering in the paper). Calculation results of transmission spectra of disordered PhC waveguides, which had been conducted until 2009, could not include localization and multiple scattering in the slow light regime. A new calculation method based on coupled-mode theory successfully reproduced transmission spectra of disorder-induced PhC waveguides [46–49]. Related to Ref. [42] and [44], a deeper investigation was experimentally conducted showing the transition from dispersive regime to diffusive regime [50]. Infrared camera images and a corresponding band diagram is shown in Fig. 1.7. Dispersive regime, firstly, was defined as a regime where backscattering in a PhC waveguide is dominant and localization length  $l$  is enough larger than device length  $L$ ,  $l \gg L$ . Here, localization length is defined as Eq. (1.5), where  $T$  is transmittance of the PhC waveguide at certain wavelength.

$$l^{-1} = -\langle \ln T \rangle / L \quad (1.5)$$

Secondly, diffusive regime is defined as  $l \approx L$ . In this diffusive regime, some proportion

of all backscattering phenomena in a PhC waveguide couples to waveguide modes, and this is called coherent backscattering [40,45]. The third one is localized regime defined as  $l \ll L$  (sometimes  $l \ll \lambda$ , as introduced above).

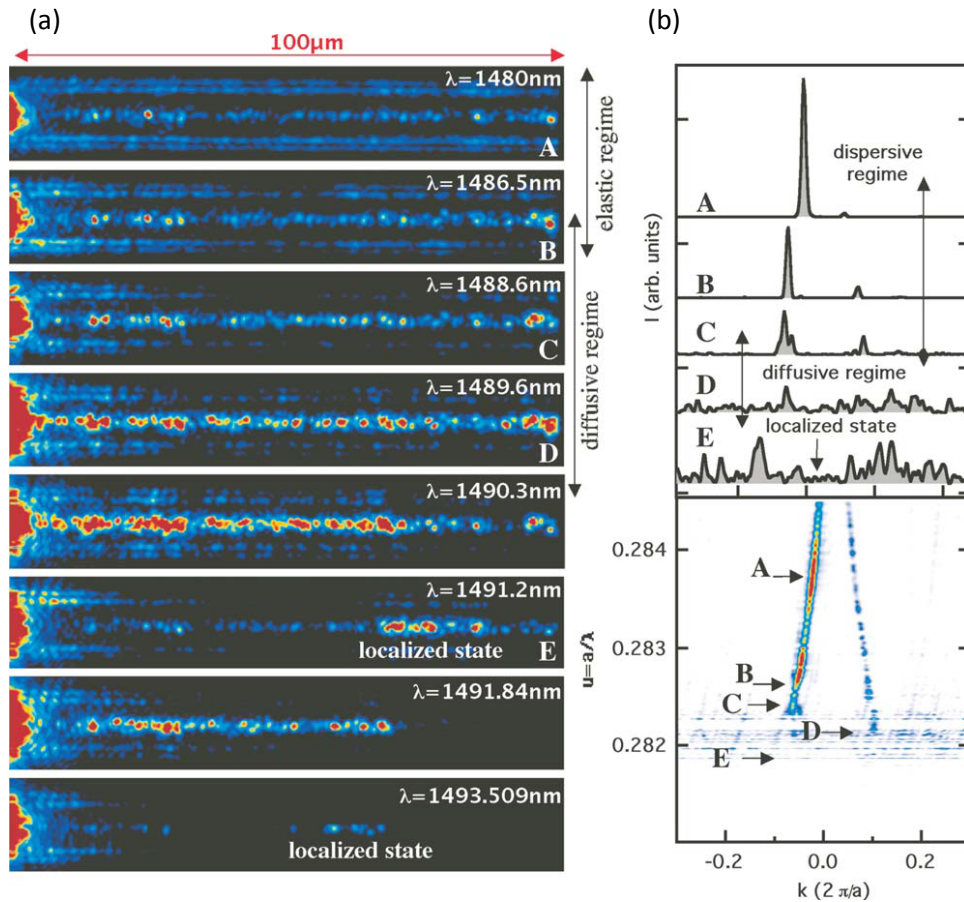


Fig. 1.7. Scanning of the light transport regimes along the dispersion curve. (a) The different light propagation regimes in the W1 photonic crystal waveguide highlighted with the real-space images of the radiated infrared field. (b) The corresponding 2D map representation of the dispersion diagram (at the bottom) as well as some of the angular spectrum profiles (at the top). The 2D representation consists in stacking the angular spectra measured at different frequencies. The position of the intensity maximum (color coded) reproduces the dispersion curve [50] [Reprinted with permission from N. Le Thomas, H. Zhang, J. Jágerská, V. Zabelin, R. Houdré, I. Sagnes and A. Talneau, "Light transport regimes in slow light photonic crystal waveguides," Phys. Rev. B **80**, 125332 (2009).].

Those disorder-induced PhC waveguides are based on randomness or probability. PhC waveguides with randomness were investigated statistically with many identical

chips [51]. This study took it consider that PhC waveguides are used in practical applications. We believe this attitude toward randomness in PhCs is necessary when considering integration of PhCs in other silicon photonics devices. Studies on randomness in PhCs can be categorize into two field. The one is fundamental physics and the other is device applications. So far, studies on fundamental physics have been introduced. There have been studies on device applications, for example random lasers [52,53]. We are more interested in the intermediate of those two, like Ref. [51]. Randomness in PhCs cannot be removed completely, so it is important to think how to deal with randomness. Since my motivation is to make PhCs more practical device using photolithography, dealing with randomness is, moreover, important. Although Refs. [52] and [53] realized laser devices based on random localization of light, the probability of and the position of localization and the direction of laser emission were not controlled. Those devices are not for practical situation. In this thesis, I utilize randomness in PhCs for practical use.

## **1.3 Previous works in demultiplexers on PhCs**

### **Silica/silicon arrayed waveguide gratings**

Optical communication, nowadays, has been supported by wavelength division multiplexing (WDM) technology [54] that was, to the best of our knowledge, first proposed in 1958. In this technology, different optical signals are delivered on different carrier wavelengths, and combined in a single optical line. Since many signals travels in just a single line, it covers large-capacity data transmission, so it has been mainly used in long-haul optical communication. As devices to combine and split those signals, or these are called multiplex and demultiplex, respectively, arrayed waveguide gratings (AWGs) was proposed in early 90's [55,56]. Until AWGs were proposed, spatial multi/demultiplexing had been investigated using, for example, diffraction on optical gratings. Those AWGs were fabricated on silica and their ability has been developing very well [57–59]. To pursue further integration of AWGs into other silicon photonic devices, silicon-on-insulator (SOI) based AWGs started developing [60–63]. The reason

why silicon photonics got attention as a candidate for demultiplexer is their small footprint. The ever-increasing data traffic in optical communication in datacenters and so on requires AWGs to be much smaller and to be used in short-haul data transmission. Those SOI based AWGs are not only compatible with other silicon photonics, or CMOS, devices, but good counterparts replacing silica based AWGs with small footprint thanks to the higher refractive index of silicon than that of silica, since higher refractive index materials confine light stronger inside themselves.

### PhC DeMUXs

Although AWGs has been investigated for years, there has been another device that can be used in multi/demultiplexing, PhCs. The first proposals demultiplexers based on PhCs were published along with simulation results from Joannopoulos's group [64,65]. And the first demonstration in two-dimensional PhCs was in 2000, where two defects along a PCWG with different resonant wavelengths work as drop filters as shown in Fig. 1.8 [66].

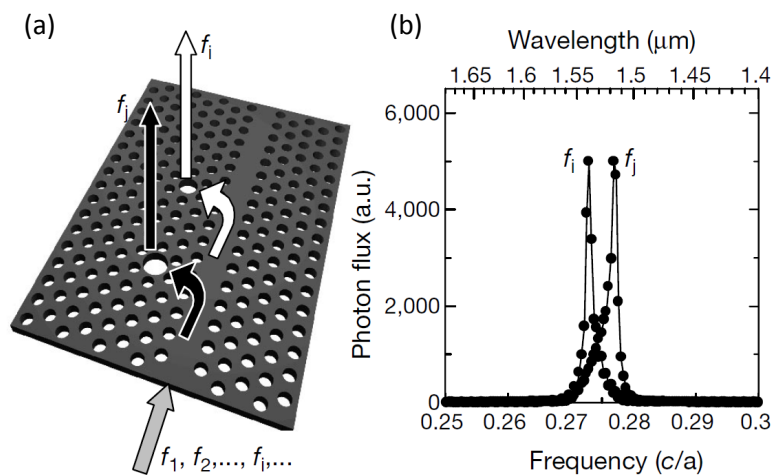


Fig. 1.8. Trapping and emission of photons by two isolated defects. (a) Schematic of defects with radius  $r_i$  and  $r_j = 0.56a$  and  $0.58a$  and resonant frequency  $f_i$  and  $f_j = 0.2729$  and  $0.2769(c/a)$  ( $1.539$  and  $1.517 \mu\text{m}$  for  $a = 0.42 \mu\text{m}$ ). (b) Calculated photon flux emitted by two defects. The top axis shows the wavelength for  $a = 0.42 \mu\text{m}$ . Photons with different frequencies of  $f_i$  and  $f_j$  are trapped and emitted to free space by the corresponding defects. In the calculation, the mutual interaction between two defects is not considered [66] [Reprinted with permission from S. Noda, A. Chutinan and M. Imada, "Trapping and emission of photons by a single defect in a photonic bandgap structure," *Nature* **407**, 608–610 (2000).].

Further investigations on various types of drop filters had been reported with calculation results [30,67,68]. Although those studies could succeed in dropping one or two wavelengths, six-channel demultiplexing was realized using a hetero PhC waveguide [69]. Many PhC demultiplexers that had been investigated drop output lights out of the PhC slab, so that configuration of the entire system needs to include a bulky part that captures output lights. On the other hand, PhC demultiplexers working in-plane have been demonstrated [70–75]. As fabrication technique becomes more precise, many researches realizing multi-channel demultiplexing have appeared [76–79].

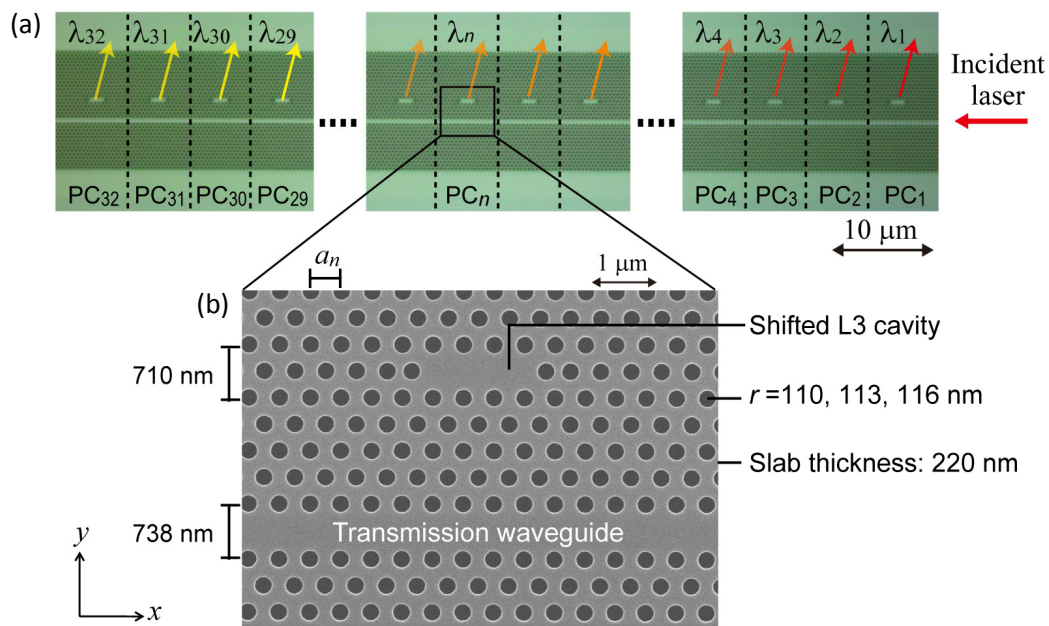


Fig. 1.9. (a) Confocal laser scanning microscope image of a 32-channel drop filter which consists of 32 photonic crystal units,  $PC_1$ – $PC_{32}$ . (b) SEM view of a  $0.2a$  shifted L3 nanocavity for the unit  $PC_n$ . The lattice constant  $a_n$  in the  $x$ -direction was  $\{410 - 0.375 \times (n - 1)\}$  nm [78] [Reprinted with permission from Y. Takahashi, T. Asano, D. Yamashita, and S. Noda, "Ultra-compact 32-channel drop filter with 100 GHz spacing," *Opt. Express* **22**, 4692–4698 (2014).].

In Ref. [78], 32 channel-100 GHz spacing capacity is achieved and the footprint is  $100 \mu\text{m}^2$  per channel. The structure is shown in Fig. 1.9. The direction of demultiplexed lights, however, is out-of-plane, and therefore, it is difficult to utilize in a practical integrated situation. On the other hand, Ref. [75] realizes in-plane demonstration, but the spacing is a few terahertz, which cannot be used in WDM. One of characteristics those

previous researches referred above is that all of them are based on L3 nanocavities. Although this L3 nanocavity described in Sec. 1.1 shows high  $Q$  with an air-bridge structure and it is easy to fabricate this design, L3 nanocavity cannot form high  $Q$  with silica-clad and is not suitable with photolithography [35]. The proposed PhC DeMUXs in this thesis work in-plane, have silica-clad and width-modulated nanocavities for their function.

## **1.4 Objective**

The objective of this thesis is to investigate the requirements for PhC devices fabricated with photolithography and demonstrate practical applications on a platform of photolithographic PhCs. Those are motivated by the recent problems in the fabrication of PhCs where EB lithography has been employed as the main method. Through evaluation and utilization of randomness, we analyze the condition of fabrication in photolithography. After that analysis, we work on more integrated devices; DeMUXs, to show the applicability of photolithographic PhCs.

# Chapter 2

## Theory

### 2.1 Optical resonators

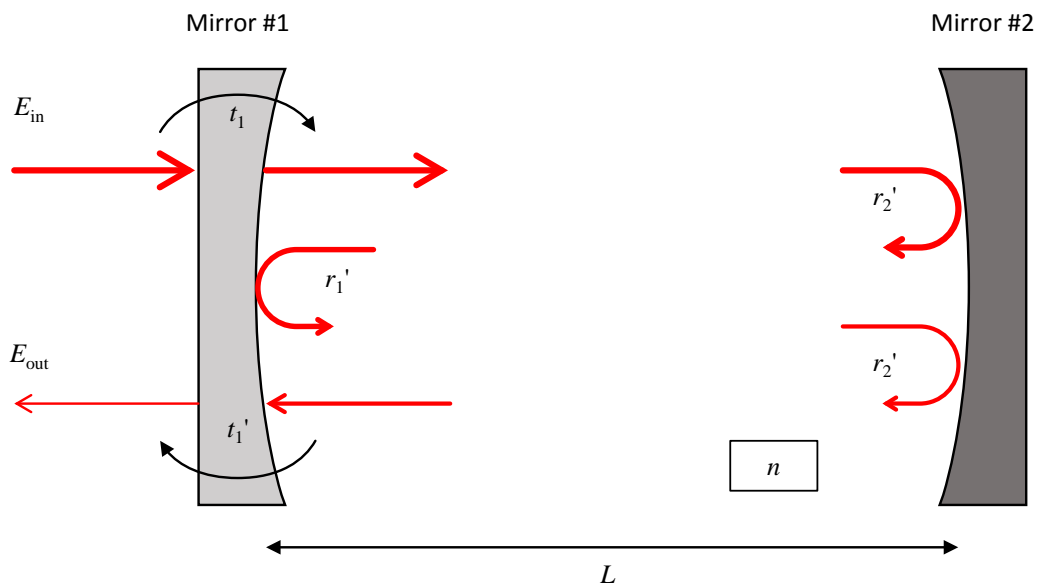


Fig. 2.1. Schematic model of a Fabry-Perot resonator. Mirror #1 is a half mirror which transmits lights from outside (inside) to inside (outside) of the Fabry-Perot resonator with transmission of  $t_1$  ( $t_1'$ ) and reflects lights with the amount of  $r_1'$ . Mirror #2 is estimated as a perfect mirror, so the reflectance  $r_2'$  is  $1 \cdot e^{j\varphi}$ , where  $\varphi$  is the amount of phase shift at the reflection.  $E_{in}$  and  $E_{out}$  are amplitudes of input and output electric fields, respectively. Parameters;  $t_1$ ,  $t_1'$ ,  $r_1'$ ,  $r_2'$ ,  $E_{in}$  and  $E_{out}$ , are all complex.  $n$  and  $L$  are refractive index inside and the length of the Fabry-Perot resonator, respectively.

As introduced in Sec. 1.1, the ability to confine light strongly is one noble characteristic of PhC nanocavities. That ability is evaluated with  $Q$  factor that is defined as Eq. (1.1), and the size of a nanocavity is evaluated with  $V$  that is defined as Eq. (1.4). In this section, using an example of a Fabry-Perot mirror, the transmission spectrum of a nanocavity is described.

Figure 2.1 shows a schematic model of a Fabry-Perot resonator, where Mirror #1 is a half mirror and Mirror #2 is a perfect mirror. Mirror #1 has transmittance from outside (inside) to inside (outside) of the Fabry-Perot resonator with transmission of  $t_1$  ( $t_1'$ ) and reflectance of  $r_1'$ . The reflectance of Mirror #2 is  $r_2'$ .  $E_{in}$  is the amplitude of input light and  $E_{out}$  is that of output light which originates in  $E_{in}$ . All parameters listed above are complex as described in Eqs. (2.1)-(2.6) below.

$$r_1' = |r_1'| \cdot e^{j\varphi_{r_1'}} \quad (2.1)$$

$$r_2' = |r_2'| \cdot e^{j\varphi_{r_2'}} \quad (2.2)$$

$$t_1 = |t_1| \cdot e^{j\varphi_{t_1}} \quad (2.3)$$

$$t_1' = |t_1'| \cdot e^{j\varphi_{t_1'}} \quad (2.4)$$

$$E_{in} = |E_{in}| \cdot e^{j\varphi_{E_{in}}} \quad (2.5)$$

$$E_{out} = |E_{out}| \cdot e^{j\varphi_{E_{out}}} \quad (2.6)$$

$n$  and  $L$  shown in Fig. 2.1 are refractive index inside and the length of the Fabry-Perot resonator, respectively. These two parameters are real.

Since  $E_{out}$  is the output light originated in  $E_{in}$  from the Fabry-Perot resonator,  $E_{out}$  can be described as Eq. (2.7).

$$\begin{aligned} E_{out} &= t_1 E_{in} \cdot (r_2' t_1' e^{-jk2nL} + r_2' t_1' r_1' r_2' e^{-jk4nL} + \dots) \\ &= t_1 E_{in} r_2' t_1' e^{-jk2nL} \cdot \frac{1}{1 - r_1' r_2' e^{-jk2nL}} \end{aligned} \quad (2.7)$$

Here,  $k$  is wavenumber at the resonance, described as  $2\pi/\lambda$  or  $2\pi\nu/c$ . The term  $e^{-jk2nL}$  describes the variation of phase when the wave propagates round-trip. Power transmission,  $T$ , of this Fabry-Perot resonator is described with input and output electric field as Eq. (2.8).

$$T = \left| \frac{E_{out}}{E_{in}} \right|^2 \quad (2.8)$$

Then, assume  $\varphi_{r_1'} = \varphi_{r_2'} = \varphi_{t_1} = \varphi_{t_1'} = 0$  and  $r_2' = 1$ , Eq. (2.9) can be obtained.

$$\begin{aligned}
T &= \left| \frac{E_{\text{out}}}{E_{\text{in}}} \right|^2 \\
&= \left| t_1 t_1' e^{-jk2nL} \cdot \frac{1}{1 - r_1' e^{-jk2nL}} \right|^2 \\
&= |t_1 t_1'|^2 \cdot \frac{1}{[1 - |r_1'| \cos(k2nL)]^2 + |r_1'|^2 \sin^2(k2nL)}
\end{aligned} \tag{2.9}$$

$t$  and  $r$  are in the relationship of Eq. (2.10).

$$\begin{aligned}
|t| + |r| &= 1 \\
R &\equiv |r|^2
\end{aligned} \tag{2.10}$$

Here, when the input wavelength is close to the resonance and satisfies  $k2nL \approx 2\pi N$  ( $N$ : integer), a condition of Eq. (2.11) satisfies.

$$\cos(k2nL) \approx 1 \tag{2.11}$$

$T$  in Eq. (2.9) can be transformed to Eq. (2.12), by inserting Eqs. (2.10) and (2.11).

$$\begin{aligned}
T &\approx |t_1 t_1'|^2 \cdot \frac{1}{(1 - |r_1'|^2)^2 + |r_1'|^2 \sin^2(k2nL)} \\
&= \frac{1}{\frac{(1 - |r_1'|^2)^2}{|t_1 t_1'|^2} + \frac{|r_1'|^2}{|t_1 t_1'|^2} \cdot \sin^2(k2nL)} \\
&= \frac{1}{1 + \frac{R}{(1 - R)^2} \cdot \sin^2(k2nL)}
\end{aligned} \tag{2.12}$$

From Eq. (2.12), it can be seen that the transmission around resonance of a Fabry-Perot resonator has Lorentzian shape shown in Eq. (2.13).

$$f(x) = \frac{1}{1 + Ax^2} \tag{2.13}$$

Next,  $\Delta\nu_{\text{FWHM}}$  is derived. FWHM represents full width half maximum, which means the width where the transmittance becomes half. From Eq. (2.12), it is seen that the maximum transmittance is 1, and when it becomes half Eq. (2.14) is satisfied. Starting from Eq. (2.14),  $\Delta\nu_{\text{FWHM}}$  is calculated as Eq. (2.15).

$$\frac{R}{(1-R)^2} \cdot \sin^2(k2nL) = 1 \quad (2.14)$$

$$\begin{aligned} \sin(k_{\pm}2nL) &= \pm \frac{1-R}{\sqrt{R}} \\ k_{\pm} &= \pm \frac{1}{2nL} \cdot \sin^{-1} \frac{1-R}{\sqrt{R}} \\ \nu_{\pm} &= \pm \frac{c}{4\pi nL} \sin^{-1} \frac{1-R}{\sqrt{R}} \end{aligned} \quad (2.15)$$

$$\begin{aligned} \therefore \Delta\nu_{\text{FWHM}} &= \nu_{+} - \nu_{-} = \frac{c}{2\pi nL} \sin^{-1} \frac{1-R}{\sqrt{R}} \\ &\approx \frac{c}{2\pi nL} \cdot \frac{1-R}{\sqrt{R}} \end{aligned}$$

The spacing of neighboring resonances is defined as free-spectrum range: FSR, and it is derived as Eq. (2.16).

$$\begin{aligned} 2nL &= N \cdot \frac{c}{\nu_N} = (N+1) \cdot \frac{c}{\nu_{N+1}} \\ \therefore FSR &= \nu_{N+1} - \nu_N = \frac{c}{2nL} \end{aligned} \quad (2.16)$$

The proportion between  $\Delta\nu_{\text{FWHM}}$  and  $FSR$  is known as the finesse;  $F$ , shown in Eq. (2.17).

$$F = \frac{FSR}{\Delta\nu_{\text{FWHM}}} \approx \frac{\pi\sqrt{R}}{1-R} \quad (2.17)$$

## 2.2 Photonic band structure

At first, an electro-magnetic wave in a dielectric material is described with Maxwell's equations.  $\mathbf{D}$ ,  $\mathbf{B}$ ,  $\mathbf{E}$ ,  $\mathbf{H}$ ,  $\mathbf{J}$  and  $\rho$  is electric flux density, magnetic flux density, electric field, magnetic field, current density and electric charge, respectively.

$$\begin{aligned} \nabla \cdot \mathbf{D} &= \rho \\ \nabla \cdot \mathbf{B} &= 0 \\ \nabla \times \mathbf{E} &= -\frac{\partial \mathbf{B}}{\partial t} \\ \nabla \times \mathbf{H} &= \mathbf{J} + \frac{\partial \mathbf{D}}{\partial t} \end{aligned} \quad (2.18)$$

$\mathbf{D}$  and  $\mathbf{B}$  can be described as Eq. (2.19).

$$\begin{aligned}
\mathbf{D}(\mathbf{r}) &= \varepsilon_0 \mathbf{E}(\mathbf{r}) + \mathbf{P}(\mathbf{r}) = \varepsilon_0 \varepsilon(\mathbf{r}) \mathbf{E}(\mathbf{r}) \\
\mathbf{B}(\mathbf{r}) &= \mu_0 (\mathbf{H}(\mathbf{r}) + \mathbf{M}(\mathbf{r})) = \mu_0 \mu(\mathbf{r}) \mathbf{H}(\mathbf{r})
\end{aligned} \tag{2.19}$$

Here, current density,  $\mathbf{J}$ , can be assumed as 0 in a dielectric without sources of light, and  $\mu_0 \mu(\mathbf{r})$  can be simplified as  $\mu_0$  because the relative magnetic permeability  $\mu(\mathbf{r})$  is very close to unity. The Maxwell's equation in Eq. (2.18) is changed as Eq. (2.20) by inserting Eq. (2.19).

$$\begin{aligned}
\nabla \cdot [\varepsilon(\mathbf{r}) \mathbf{E}(\mathbf{r}, t)] &= 0 \\
\nabla \cdot \mathbf{H}(\mathbf{r}, t) &= 0 \\
\nabla \times \mathbf{E}(\mathbf{r}, t) + \mu_0 \frac{\partial \mathbf{H}(\mathbf{r}, t)}{\partial t} &= 0 \\
\nabla \times \mathbf{H}(\mathbf{r}, t) - \varepsilon_0 \varepsilon(\mathbf{r}) \frac{\partial \mathbf{E}(\mathbf{r}, t)}{\partial t} &= 0
\end{aligned} \tag{2.20}$$

Since it is known that  $\mathbf{E}$  and  $\mathbf{H}$  have oscillation modes, those can be written as Eq. (2.21).

$$\begin{aligned}
\mathbf{E}(\mathbf{r}, t) &= \mathbf{E}(\mathbf{r}) \cdot e^{-j\omega t} \\
\mathbf{H}(\mathbf{r}, t) &= \mathbf{H}(\mathbf{r}) \cdot e^{-j\omega t}
\end{aligned} \tag{2.21}$$

First two equations in Eq. (2.20) describe initial and boundary conditions, and the third and fourth equations in Eq. (2.20) describe the relation between  $\mathbf{E}$  and  $\mathbf{H}$ . By inserting Eq. (2.21) into Eq. (2.20), Eq. (2.22) is obtained.

$$\begin{aligned}
\nabla \times \mathbf{E}(\mathbf{r}) - j\omega \mu_0 \mathbf{H}(\mathbf{r}) &= 0 \\
\nabla \times \mathbf{H}(\mathbf{r}) + j\omega \varepsilon_0 \varepsilon(\mathbf{r}) \mathbf{E}(\mathbf{r}) &= 0
\end{aligned} \tag{2.22}$$

By taking the curl of Eq. (2.22), Eq. (2.23) is obtained.

$$\begin{aligned}
\nabla \times \left( \frac{1}{\varepsilon(\mathbf{r})} \nabla \times \mathbf{H}(\mathbf{r}) \right) &= \left( \frac{\omega}{c} \right)^2 \mathbf{H}(\mathbf{r}) \\
\left( \text{s. t. } c &= \frac{1}{\sqrt{\varepsilon_0 \mu_0}} \right)
\end{aligned} \tag{2.23}$$

Next, define an operator  $\Theta$  as Eq. (2.24).

$$\begin{aligned}
\Theta \mathbf{H}(\mathbf{r}) &\equiv \nabla \times \left( \frac{1}{\varepsilon(\mathbf{r})} \nabla \times \mathbf{H}(\mathbf{r}) \right) \\
\therefore \Theta \mathbf{H}(\mathbf{r}) &= \left( \frac{\omega}{c} \right)^2 \mathbf{H}(\mathbf{r})
\end{aligned} \tag{2.24}$$

In a periodic structure, such as a photonic crystal,  $\mathbf{H}(\mathbf{r})$  can be assumed as a periodic function that has Bloch wavevector  $\mathbf{k}$ , on the basis of Bloch-Floquet theorem.

$$\begin{aligned}\mathbf{H}(\mathbf{r}) &= \mathbf{H}_{\mathbf{k}}(\mathbf{r}) = e^{j\mathbf{k}\cdot\mathbf{r}} \cdot \mathbf{H}_{n,\mathbf{k}}(\mathbf{r}) \\ \mathbf{H}_{n,\mathbf{k}}(\mathbf{r}) &= \mathbf{H}_{n,\mathbf{k}}(\mathbf{r} + \mathbf{a})\end{aligned}\quad (2.25)$$

Here,  $\mathbf{a}$  is a period of the structure and  $n$  corresponds to the label number for primitive cells that is a part of a periodic structure. Equation (2.26) is obtained when Eq. (2.25) is inserted into Eq. (2.23).

$$(\nabla + j\mathbf{k}) \times \frac{1}{\varepsilon(\mathbf{r})} (\nabla + j\mathbf{k}) \times \mathbf{H}_{n,\mathbf{k}}(\mathbf{r}) = \left( \frac{\omega_n(\mathbf{k})}{c} \right)^2 \mathbf{H}_{n,\mathbf{k}}(\mathbf{r}) \quad (2.26)$$

$\left( \frac{\omega_n(\mathbf{k})}{c} \right)^2$  are eigenvalues in this Schrödinger equation, and here,  $\omega_n(\mathbf{k})$  are functions of  $\mathbf{k}$ .

The relationship between  $\omega_n(\mathbf{k})$  and  $\mathbf{k}$  is called a “dispersion diagram” when these are drawn in a figure.

Since  $\mathbf{H}(\mathbf{r})$  is a Bloch function as described in Eqs. (2.25), it satisfies a condition below, where wavevector  $\mathbf{k}'$  is assumed as  $\mathbf{k}' = \mathbf{k} + \frac{2\pi}{a}$ .

$$\mathbf{H}_{\mathbf{k}}(\mathbf{r}) = e^{j\left(\mathbf{k}' - \frac{2\pi}{a}\right)\cdot\mathbf{r}} \cdot \mathbf{H}_{n,\mathbf{k}}(\mathbf{r}) = e^{j\mathbf{k}'\cdot\mathbf{r}} \cdot \mathbf{H}_{n,\mathbf{k}}(\mathbf{r}) e^{-j\frac{2\pi}{a}\cdot\mathbf{r}} \quad (2.27)$$

Here, since  $\mathbf{H}_{n,\mathbf{k}}(\mathbf{r}) e^{-j\frac{2\pi}{a}\cdot\mathbf{r}} = \mathbf{H}_{n,\mathbf{k}}(\mathbf{r} + \mathbf{a}) e^{-j\frac{2\pi}{a}(\mathbf{r} + \mathbf{a})}$ , it let us consider as Eqs. (2.28).

$$\begin{aligned}\mathbf{H}_{n,\mathbf{k}'}(\mathbf{r}) &= \mathbf{H}_{n,\mathbf{k}}(\mathbf{r}) e^{-j\frac{2\pi}{a}\cdot\mathbf{r}} \\ \mathbf{H}_{\mathbf{k}}(\mathbf{r}) &= e^{j\mathbf{k}'\cdot\mathbf{r}} \cdot \mathbf{H}_{n,\mathbf{k}'}(\mathbf{r}) = \mathbf{H}_{\mathbf{k}'}(\mathbf{r})\end{aligned}\quad (2.28)$$

From Eqs. (2.28), it is proven that  $\mathbf{H}_{\mathbf{k}}(\mathbf{r})$  is a periodical function in  $2\pi/a$ , and therefore, the eigenvalues,  $\omega_n(\mathbf{k})$ , also has a period of  $2\pi/a$ . In a dispersion diagram,  $\mathbf{k}$  of  $\mathbf{0}$  is usually taken as the center and the range is limited within  $2\pi/a$  as described in Eq. (2.29).

$$-\frac{\pi}{a} \leq \mathbf{k} \leq \frac{\pi}{a} \quad (2.29)$$

This range is called the first Brillouin zone. In the situation where time-reversal symmetry can be considered ( $\mathbf{k} = -\mathbf{k}$ ), the range of a dispersion diagram can be more limited as Eq. (2.30).

$$\mathbf{0} \leq \mathbf{k} \leq \frac{\pi}{a} \quad (2.30)$$

Next, a dispersion diagram is discussed. When a one-dimensional system is considered (vectors can be converted into scalar), and it has uniform dielectric of  $\epsilon(r) = 1$ , Eq. (2.26) has eigensolutions  $\omega(k) = ck$  as shown in Fig. 2.2.

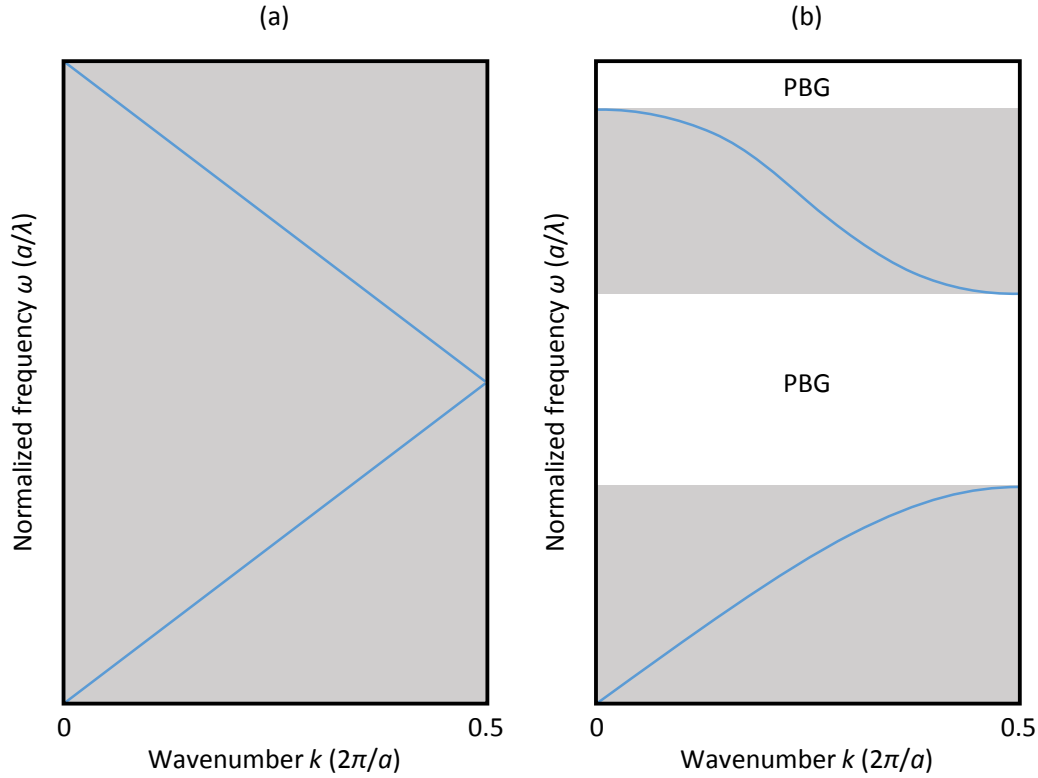


Fig. 2.2. Dispersion diagrams of (a) an uniform dielectric material,  $\epsilon(r) = 1$ , and (b) a periodically perturbed material,  $\epsilon(r) = 1 + \Delta \cdot \cos(2\pi r/a)$ .

On the other hand, consider a one-dimensional system with periodical perturbation of  $\Delta$  in dielectric constant,  $\epsilon(r) = 1 + \Delta \cdot \cos(2\pi r/a)$ . At  $k = \pi/a$ ,  $H$  in the one-dimensional system cannot transverse because  $H$  becomes a standing wave due to Bragg reflection. A standing wave can be described in two ways.

$$\begin{aligned} H_+ &\propto e^{j\frac{\pi r}{a}} + e^{-j\frac{\pi r}{a}} = 2 \cos\left(\frac{\pi r}{a}\right) \\ H_- &\propto e^{j\frac{\pi r}{a}} - e^{-j\frac{\pi r}{a}} = j2 \sin\left(\frac{\pi r}{a}\right) \end{aligned} \quad (2.31)$$

Now, the relationships between frequency and energy, and between power of magnetic field and energy are in proportion.

$$\begin{aligned}\omega_{+,k=\frac{\pi}{a}} &\propto |H_+|^2 \propto 4 \cos^2\left(\frac{\pi r}{a}\right) \\ \omega_{-,k=\frac{\pi}{a}} &\propto |H_-|^2 \propto 4 \sin^2\left(\frac{\pi r}{a}\right)\end{aligned}\tag{2.32}$$

Finally, Eq. (2.32) shows there are two different energy states at  $k = \pi/a$ . That explains why photonic band gap (PBG) appears in a periodic structure, and this can be expand into two- and three-dimensional periodic structures.

Dispersion diagrams can be calculated by solving Eq. (2.26) computationally. A free program developed by Joannopoulos's group, called "MPB," provides us solutions. Figure 2.3 shows dispersion diagrams of PhCs with lattice constant  $a$  of 420 nm and hole diameter  $d$  of 253 nm. Vertical axis is "normalized" frequency, where frequency is divided by  $a/\lambda$ . Horizontal axis is wavenumber that is also normalized and is divided by  $2\pi/a$ . Yellow area represents light cone,  $\omega > (c/n)\cdot k$ , where  $c$  and  $n$  represents the speed of light and refractive index of out of the slab. When light is in the light cone, it dissipates out of slab because the condition of total internal reflection cannot be satisfied. The structure in Fig. 2.3(a) is the perfectly periodic PhC, while that in Fig. 2.3(b) has a line defect PhC waveguide as shown in the inset. The line defect is W0.98 (98% of the original width). Two defect modes appear in the PBG, which are waveguide modes.

Figure 2.4 shows dispersion diagrams when holes of PhCs are silica,  $n = 1.44$ . Comparing Figs. 2.3 and 2.4, it can be seen that the frequency range of PBG gets narrower when the ambience of silicon is silica, so-called silica-clad. This is because the difference of refractive indices between the PhC slab and the surrounding material gets small. Another interesting point is that silica-clad PhCs has gentle slope in light line, which leads to limitation for PhC waveguide modes. In silica-clad PhC waveguides, light can have narrower frequency range to exist, or propagate.

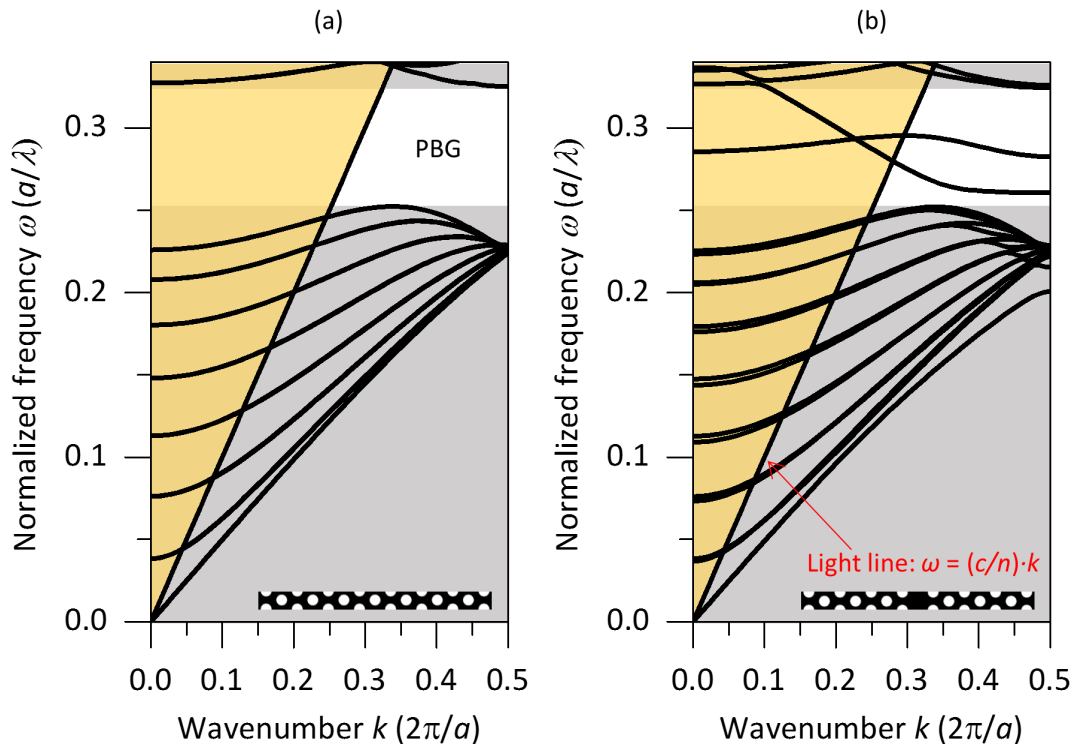


Fig. 2.3. Dispersion diagrams of two-dimensional PhCs with triangle lattice.  $\omega$  from 0.25 to 0.32 corresponds to photonic band-gap (PBG). Yellow area represents light cone where light in a PhC slab dissipate out of slab because the condition of total internal reflection cannot be satisfied. (a) Lattice constant  $a$  of 420 nm, hole diameter  $d$  of 253 nm. (b) A line defect is included in a PhC with  $a$  and  $d$  of 420 nm, and 253 nm. The line defect is W0.98 (98% of the original width). Two defect modes appear in the PBG, which are waveguide modes. Insets show the corresponding structure. Black and white area have refractive index of 3.47 and 1.00, respectively. These estimate silicon and air as their materials.

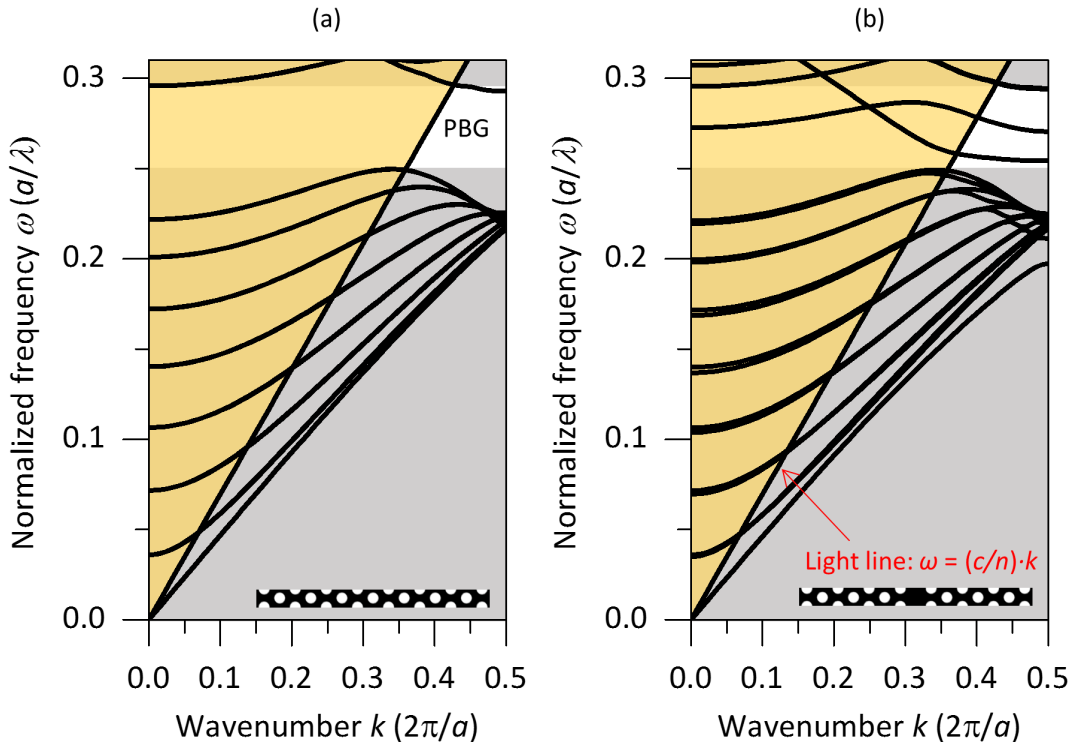


Fig. 2.4. Dispersion diagrams of two-dimensional PhCs with triangle lattice.  $\omega$  from 0.25 to 0.29 corresponds to photonic band-gap (PBG). Yellow area represents light cone where light in a PhC slab dissipate out of slab because the condition of total internal reflection cannot be satisfied. (a) Lattice constant  $a$  of 420 nm, hole diameter  $d$  of 253 nm. (b) A line defect is included in a PhC with  $a$  and  $d$  of 420 nm, and 253 nm. The line defect is W0.98 (98% of the original width). Two defect modes appear in the PBG, which are waveguide modes. Insets show the corresponding structure. Black and white area have refractive index of 3.47 and 1.44, respectively. These estimate silicon and air as their materials.

## 2.3 Design strategy of high- $Q$ PhC nanocavities

### 2.3.1 Light cone

In Sec. 2.2, it was explained that a certain wavevector stays in a periodical dielectric structure as a static wave due to Bragg reflection, which leads to the split of energy states, or PBG. Three-dimensional PhCs can satisfy the conditions of PBG in all direction, but one- and two-dimensional PhCs have PBG in one or two directions. Two-dimensional PhC nanocavities described in Sec. 1.2 confine lights with PBG in  $x$ - $y$  plane and with total-internal-reflection (TIR) in  $z$ -direction (out-of-slab direction).

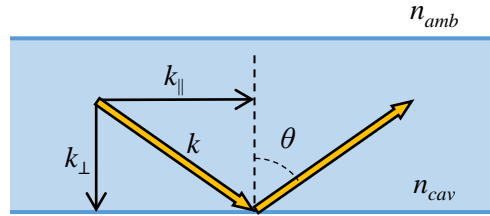


Fig. 2.5. Schematic of a wavevector;  $k$ , which is reflected at the boundary between a nanocavity and its ambience.  $n_{cav}$  and  $n_{amb}$  are the refractive indices of the nanocavity and the ambience, respectively.  $k_{\parallel}$  and  $k_{\perp}$  are components of  $k$  in the parallel and vertical direction.  $\theta$  is incident and reflex angle.

Here, we assume the refractive indices of a nanocavity and its ambience as  $n_{cav}$  and  $n_{amb}$ , and the components of wavevector  $k$  are  $k_{\parallel}$  and  $k_{\perp}$  in the direction of parallel and vertical to the slab as shown in Fig. 2.5.  $k$  satisfies Eq. (2.33).

$$k^2 = k_{\parallel}^2 + k_{\perp}^2 = \left(\frac{n_{cav}\omega}{c}\right)^2 \quad (2.33)$$

When the light that has wavevector  $k$  is in the condition of TIR, Eq. (2.34) is supposed to be satisfied, which is called Snell's law.

$$\sin \theta = \left|\frac{k_{\parallel}}{k}\right| > \frac{n_{amb}}{n_{cav}} \quad (2.34)$$

From Eqs. (2.33) and (2.34), the condition where light in the nanocavity dissipate from the slab is calculated.

$$|k_{\parallel}| < \frac{n_{amb}\omega}{c} \quad (2.35)$$

When the light is in the condition of Eq. (2.35), it will disappear. This condition is called as light cone. One can understand why it has “cone” in its name, when the problem is expand to two-dimension.

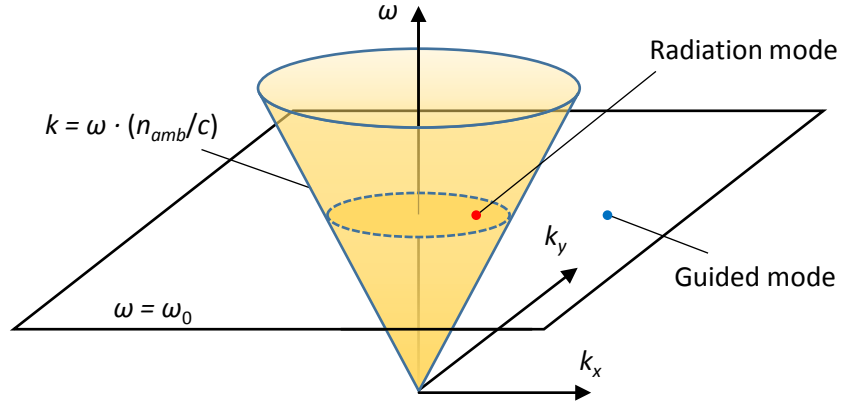


Fig. 2.6. Light cone in  $k_x$ ,  $k_y$  and  $\omega$  space. Yellow cone corresponds to light cone in which light dissipates from a slab.

Figure 2.6 shows light cone in the two-dimensional problem. The basic concept is similar to Fig. 2.5. When wavevectors of light at the frequency of  $\omega_0$  has component in the broken circle, the light cannot exist in the slab and it dissipates.

### 2.3.2 Mode profile in momentum space

Since the component in light cone leads to loss, it is important to reduce the component in light cone when high- $Q$  PhC nanocavities are designed. Those components are drawn in  $k_x$ - $k_y$  space or momentum space, so it is necessary to obtain a momentum space map.

A mode profile of a nanocavity in real space is in the relationship of Fourier transform with momentum space as Eq. (2.36).

$$\begin{aligned} x &\xrightarrow{\mathcal{F}} \frac{2\pi}{x} \\ y &\xrightarrow{\mathcal{F}} \frac{2\pi}{y} \end{aligned} \quad (2.36)$$

Figure 2.7 is an example of the relationship of mode profile in real space and momentum space.

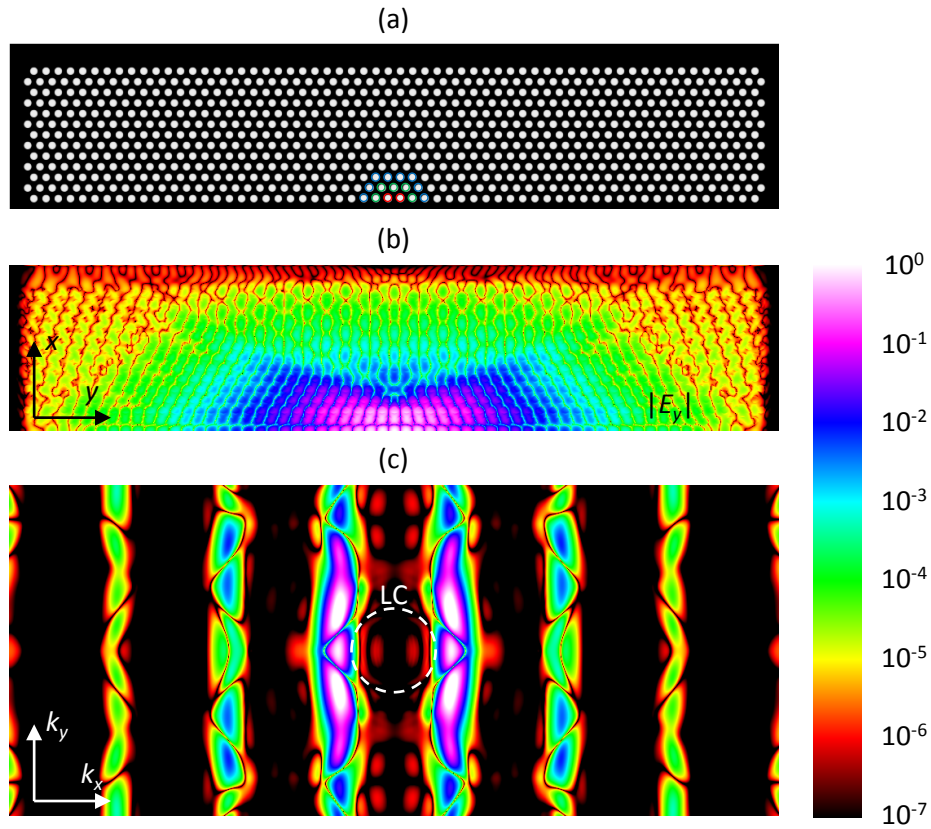


Fig. 2.7. FDTD calculation results of a width-modulated nanocavity, where  $a$ ,  $d$ ,  $n_{\text{slab}}$  and  $n_{\text{amb}}$  are 420 nm, 246 nm, 3.47 and 1.44, respectively. (a) Epsilon profile of upper half of the nanocavity. Colored circles represent the nanocavity region, where red, green and blue circles are shifted toward upper side by 9, 6 and 3 nm, respectively. (b)  $|E_y|$  profile at the resonance. (c) Momentum space profile. The broken circle at the center describes light cone (LC) when the ambience is silica,  $n_{\text{amb}} = 1.44$ . Color bar in the right is for (b) and (c).

## 2.4 FDTD calculation

Finite-difference time-domain (FDTD) is the method to calculate propagation of light in dielectric structures. It provides highly accurate solutions for the characteristics of PhCs in frequency and time domain. Simply speaking, this method calculates Maxwell's equations sequentially with a tiny time period step by step. Because of this step by step procedure, FDTD calculation takes a lot of time to finish computing. For a decade, this FDTD has been getting a common way thanks to the development of computational facilities and costs. In this section, the fundamental computational method for FDTD calculation is described using a two-dimensional model.

A two-dimensional structure is set in a  $x$ - $y$  plane, and let's assume electro-magnetic wave that has electric field in the  $x$ - $y$  plane and magnetic field in  $z$  direction. This type of electro-magnetic wave is called transverse electric (TE) wave. Here, note that  $\frac{\partial}{\partial z} = 0$  in a two-dimensional problem, the bottom two of Eqs. (2.20) are described as Eqs. (2.37).

$$\begin{aligned}\frac{\partial E_x}{\partial t} &= \frac{1}{\epsilon_0 \epsilon(x, y)} \cdot \frac{\partial H_x}{\partial y} \\ \frac{\partial E_y}{\partial t} &= -\frac{1}{\epsilon_0 \epsilon(x, y)} \cdot \frac{\partial H_x}{\partial x} \\ \frac{\partial H_z}{\partial t} &= -\frac{1}{\mu_0} \cdot \left( \frac{\partial E_y}{\partial x} - \frac{\partial E_x}{\partial y} \right)\end{aligned}\tag{2.37}$$

The first equation in Eqs. (2.37) can be, next, transformed in discretized expressions.

$$\begin{aligned}\frac{\partial E_x}{\partial t} &\rightarrow \frac{E_x \left( x, y, t + \frac{\Delta t}{2} \right) - E_x \left( x, y, t - \frac{\Delta t}{2} \right)}{\Delta t} \\ \frac{\partial H_z}{\partial y} &\rightarrow \frac{H_x \left( x, y + \frac{\Delta y}{2}, t \right) - H_x \left( x, y - \frac{\Delta y}{2}, t \right)}{\Delta y}\end{aligned}\tag{2.38}$$

In Eqs. (2.38), central difference is taken to discretize, and those are defined as Eqs. (2.39)

$$\frac{\partial E_x}{\partial t} \rightarrow \frac{E_x^n \left( i + \frac{1}{2}, j \right) - E_x^{n-1} \left( i + \frac{1}{2}, j \right)}{\Delta t}$$

$$\frac{\partial H_z}{\partial y} \rightarrow \frac{H_z^{n-\frac{1}{2}} \left( i + \frac{1}{2}, j + \frac{1}{2} \right) - H_z^{n-\frac{1}{2}} \left( i + \frac{1}{2}, j - \frac{1}{2} \right)}{\Delta y}$$
(2.39)

From Eqs. (2.39), it is clear that  $E$  and  $H$  are calculated in turns by  $\Delta t/2$ , or  $n$  of  $1/2$ . This difference comes from discretization with center difference. Finally, Eqs. (2.37) reach discretized Eqs (2.40) and components in Eqs (2.40) can be described in a map called Yee cell (Fig. 2.8).

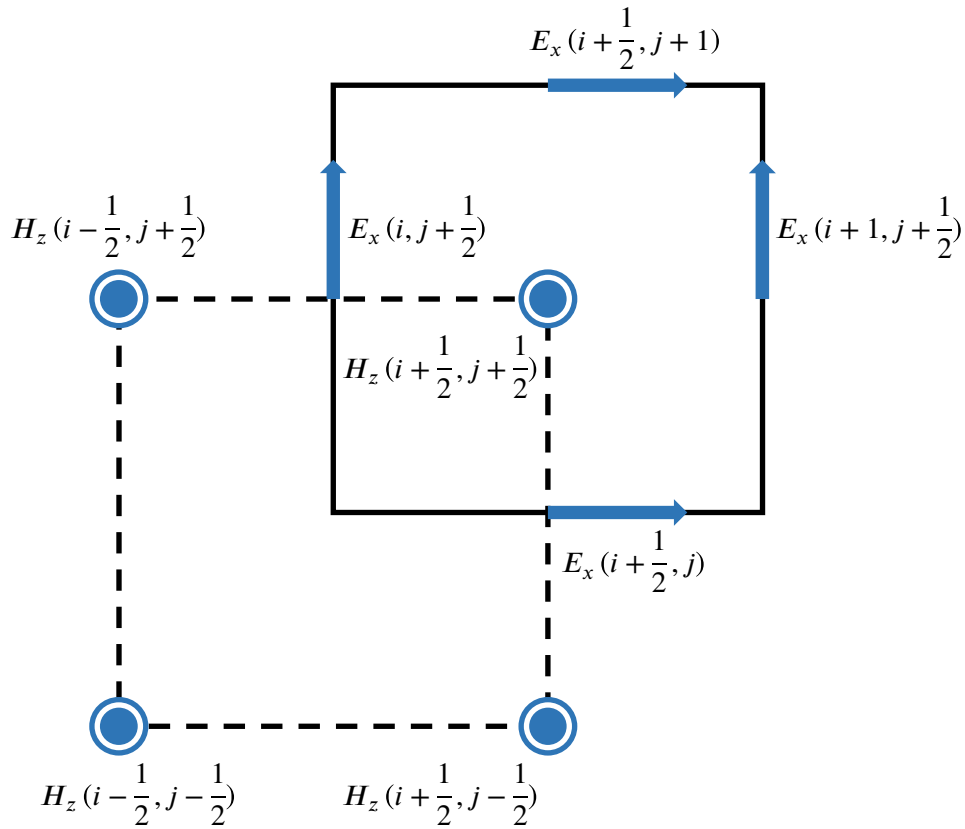


Fig. 2.8. Yee cell in FDTD calculation, which shows the space relationship between electric and magnetic fields,  $E$  and  $H$ .

$$\begin{aligned}
E_x^n\left(i+\frac{1}{2},j\right) &= E_x^{n-1}\left(i+\frac{1}{2},j\right) \\
&+ \frac{\Delta t}{\Delta y} \cdot \frac{1}{\varepsilon\left(i+\frac{1}{2},j\right)} \\
&\cdot \left[ H_z^{n-\frac{1}{2}}\left(i+\frac{1}{2},j+\frac{1}{2}\right) - H_z^{n-\frac{1}{2}}\left(i+\frac{1}{2},j-\frac{1}{2}\right) \right] \\
E_y^n\left(i,j+\frac{1}{2}\right) &= E_y^{n-1}\left(i,j+\frac{1}{2}\right) \\
&- \frac{\Delta t}{\Delta x} \cdot \frac{1}{\varepsilon\left(i,j+\frac{1}{2}\right)} \\
&\cdot \left[ H_z^{n-\frac{1}{2}}\left(i+\frac{1}{2},j+\frac{1}{2}\right) - H_z^{n-\frac{1}{2}}\left(i-\frac{1}{2},j+\frac{1}{2}\right) \right] \\
H_z^{n+\frac{1}{2}}\left(i+\frac{1}{2},j+\frac{1}{2}\right) &= \\
&H_z^{n-\frac{1}{2}}\left(i+\frac{1}{2},j+\frac{1}{2}\right) \\
&- \frac{\Delta t}{\Delta x} \cdot \frac{1}{\mu_0} \left\{ \left[ E_y^n\left(i+1,j+\frac{1}{2}\right) - E_y^n\left(i,j+\frac{1}{2}\right) \right] \right. \\
&\left. - \left[ E_x^n\left(i+\frac{1}{2},j+1\right) - E_x^n\left(i+\frac{1}{2},j\right) \right] \right\}
\end{aligned} \tag{2.40}$$

Based on Eqs. (2.40),  $E_x$ ,  $E_y$  and  $H_z$  all are calculated at every point in  $x$ - $y$  plane and in time domain.

## **Chapter 3**

# **Fabrication of two-dimensional PhCs with photolithography**

In this chapter, the fabrication technique of our PhCs are described and the evaluation of fabricated PhCs are summarized.

### **3.1 Introduction**

PhCs are small device that require nanometer scale structures. This is the reason why PhC fabrication has employed EB lithography that has been thought to be much more precise than photolithography for a long time. EB lithography is, however, costly and time-consuming and does not suit for mass-production when PhCs are considered to be used in practical applications. Photolithography has been employed to process semiconductor mainly in the field of electronic circuit devices. Technologies of photolithography has quite developed. One of the biggest advantage is its mass-productivity. This advantage derives from its procedure and technique, which is described in the following section. On contrary, one of disadvantages is its precision. PhCs require precision in nanoscale, so the accuracy of photolithography may not enough precise to fabricate PhCs. In the section after the next, precision of our PhCs are discussed through scanning electron microscope measurement.

## 3.2 Procedure of photolithography

As already mentioned above, electrical circuit devices have been developing for years. Since electrical circuit devices are based on a silicon platform, the technology to fabricate silicon devices have also been developing. The fabrication technology for them is photolithography, and there have been several researches using photolithography in the fabrication of silicon photonics devices [14,58,63,80–91]. In this section, the procedure of photolithography is described with illustrations.

The procedure of photolithography is drawn in Fig. 3.1.

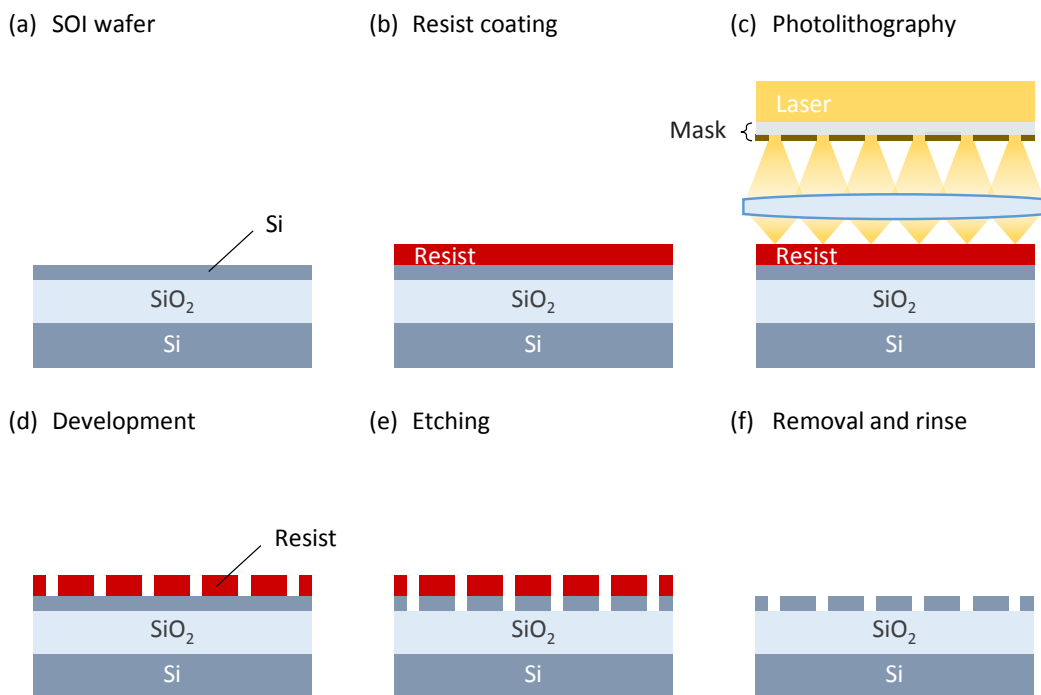


Fig. 3.1. The procedure of photolithography. (a) Typical cross-section of a silicon-on-insulator (SOI) wafer. (b) The silicon top layer is coated by a resist layer with spin coating. (c) Lithograph procedure. Laser is irradiated from the top through a mask on which patterns are depicted. Irradiated laser that passed through the mask is focused on the resist with a lens. (d) Lithographed area of the resist is removed in this development phase. (e) The silicon layer is etched through reactive-ion-etching (RIE). (f) The resist is removed and devices with the patterns are fabricated on the silicon layer.

The photomask shown in Fig. 3.1(c) is usually made of a silica plate on which a thin layer

of light-shielding material, such as chromium. When laser is irradiated to the photomask, the laser cannot pass through light-shielding area. Patterns of devices are depicted on the photomask with electron-beam (EB) lithography. EB lithography is not competitive in mass-productivity with photolithography, and using EB lithography sounds opposite to our motivation. However, once the photomask is fabricated, it can be used many times in photolithograph phase [Fig. 3.1(c)].

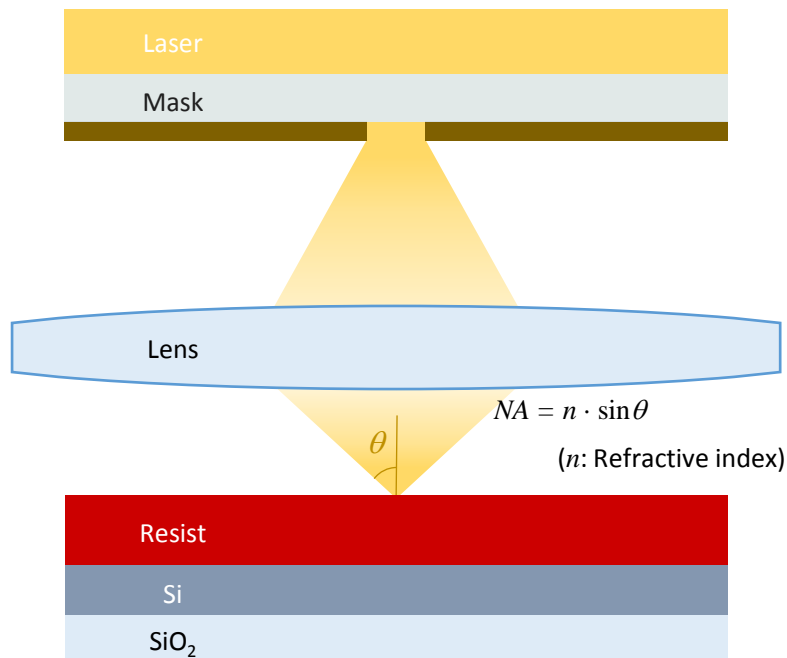


Fig. 3.2. Magnification of stepper photolithography. Its resolution is defined with  $NA$  described in the figure, where  $n$  is refractive index of the ambience. To make this  $NA$  larger, liquid ambience with higher refractive index than air is sometimes selected.

There are different two major types of photolithography, aligner and stepper lithography. In the procedure of aligner lithography, irradiated laser passing through a photomask reaches a resist layer directly. Patterns depicted on the resist layer are same size as those on the photomask. On the other hand, stepper lithography uses a lens/lenses between a photomask and a resist layer. The procedure shown in Fig. 3.1(c) is stepper lithography. This lens focuses the laser on the resist layer, which makes it possible to depict smaller patterns on the resist layer than those on the photomask. The minimum size it can depict in stepper lithography is limited by the wavelength of the laser, or

“diffraction limit.” Stepper lithography requires mechanics that can move very precisely as steps.

Excimer laser is used for the irradiated laser in photolithography. An excimer molecule is the source of laser action, and the molecule is consists of noble gases and halogens. Noble gases, such as argon, krypton and xenon, are very inert and it is usually difficult for them to form chemical compounds. Those noble gases, however, can form temporarily bound molecules with halogen, such as fluoride and chlorine, when they are in an atmosphere where electrons are highly charged. This is because those bound molecules do not have ordinal ground states but repulsive ground state. They can be formed only in excited states, and therefore, high power laser is irradiated through spontaneous or stimulated emission. ArF, KrF, XeCl and XeF are famous examples as excimer laser. Table 3.1 shows the corresponding irradiated laser wavelengths of excimers.

Table 3.1. Relationship between excimers and their irradiating laser wavelengths.

Excimer	Laser wavelength
ArF	193 nm
KrF	248 nm
XeCl	308 nm
XeF	351 nm

Those laser wavelength shown in Table 3.1 is directory connected to resolution of the process of photolithography. When resolution is denoted as  $R$ , it is described as Eq. (3.1), referred as Rayleigh criterion.

$$R = \frac{K \cdot \lambda}{NA} \quad (3.1)$$

Here,  $K$  is what is signified with several conditions, such as the system of photolithography, the size of mask and so on.  $\lambda$  is the wavelength of excimer, and  $NA$  represents numerical aperture as in Fig. 3.2. Nicer resolution means to obtain smaller  $R$  here in Eq. (3.1). It can be inducted that small  $\lambda$  or large  $NA$  (or both) leads to small  $R$ . As

shown in Table 3.1, the laser wavelength of excimers are, therefore, important and that has been getting shorter in many photolithography fabrication processes, or CMOS foundries. Using large  $NA$  is also a way to get small  $R$ . Large  $\theta$  means, however, the angle the lens focus becomes large and the area one shot of lithography can draw is limited.  $R$  and  $\theta$  are in inverse proportion. There is a way to increase  $NA$ : to use high refractive index ambience on the top of a resist layer. This is called immersion lithography.

### 3.3 The analysis of PhC hole diameter

Table 3.2. Layer numbers and their corresponding structures the foundry fabricates.

Layer #	Structures	Layer #	Structures
1	Si	13	Contact hole ( $p, n$ )
2	Rib	14	Si $n$ implant
3	PhC	15	Si $p$ implant
4	Silica trench at SSC	16	Si $n+$ implant
5	Clad window at PhC	17	Si $p+$ implant
6	Clad window at Si wire	18	Ge $n$ implant
7	Facet deep trench	19	Si $p$ implant for PD
8	Heater isolation trench	20	Ge window
9	Al wire	21	Probing/bonding pad
10	Contact hole (heater)	22	$Si_3N_4$
11	Heater (upper layer)	23	Grating
12	Heater (lower layer)		

Our PhCs are fabricated with KrF stepper lithography at the wavelength of 248 nm. We used an open CMOS foundry service provided by Institute of Microelectronics (IME,

Singapore). The foundry fabricates several structures that correspond to layer numbers as shown in Table 3.2. Layers number of 1, 14, 15, 32 are fabricated with a high definition mask (HDM). The resolution of HDM is 1 nm. Other layers except 3 are fabricated with a low definition mask (LDM). The resolution of LDM is 5 nm. The mask used for layer 3 is discussed in the following part.

There are two types of PhCs that have been used in our research, and we would like to identify each of them with identifications of KT-1 and KT-2. Characteristics of them are summarized in Table 3.2.

Table 3.3. Identifications for our PhCs. Only the masks are different among the characteristics. HDM: high definition mask. PSM: phase shifting mask.

Name	Excimer	Aligner/Stepper	Mask	Slab thickness	Year delivered
KT-1	KrF (248 nm)	Stepper	HDM	210 nm	2011
KT-2	KrF (248 nm)	Stepper	PSM	210 nm	Apr. 2016
KT-3	KrF (248 nm)	Stepper	PSM	210 nm	Nov. 2016

In the “Mask” column of Table 3.1, there are two types, HDM and PSM; representing high definition mask and phase shifting mask, respectively. With HDMs, minimum resolution of 1 nm can be theoretically patterned, and PSM can pattern as same precisely as HDM. However, a PSM is a photomask that considering proximity effect. This effect is the result of the interference of laser lights passing through a photomask, results in different amount of dose of laser and leads to different size of hole diameter. PSM takes this effect into consideration in advance, and better resolution is expected than HDM.

KT-2 and KT-3 have the same conditions in their fabrication. After KT-2 was fabricated and examined, it was clear that the hole size was different from designed hole size. This difference itself is not a big problem because, when we designed KT-2 and others, we designed many types with different hole diameters for a single pattern, so there is a pattern with desired hole diameter. KT-3 was, however, fabricated and delivered thanks to IME’s effort to find an optimized condition to pattern and etch holes in PhCs.

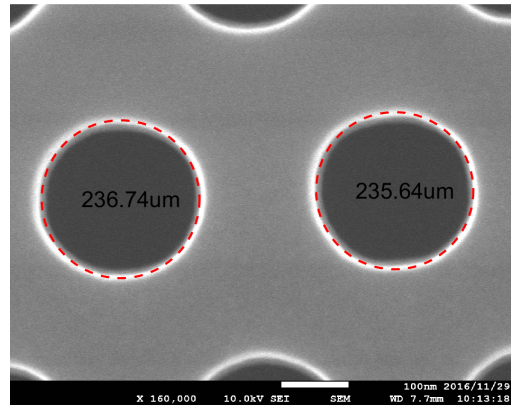
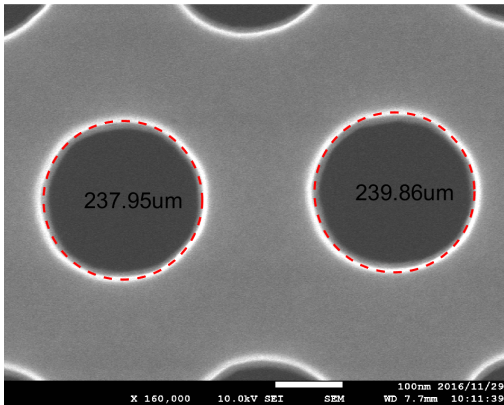


Fig. 3.3. SEM images of KT-1, where hole size is designed as 200 nm. These are two examples of 20 images we took.

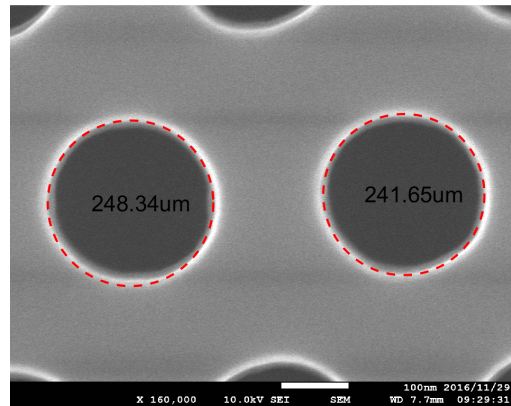
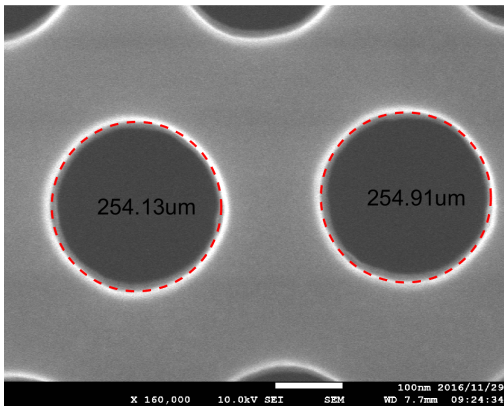


Fig. 3.4. SEM images of KT-1, where hole size is designed as 210 nm. These are two examples of 20 images we took.

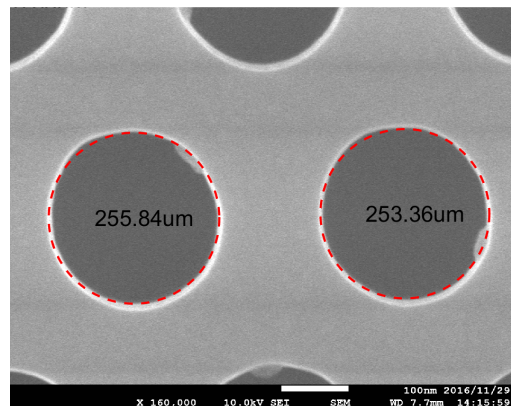
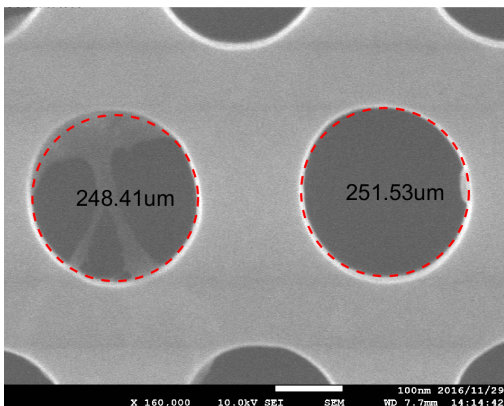


Fig. 3.5. SEM images of KT-2, where hole size is designed as 220 nm. These are two examples of 20 images we took.

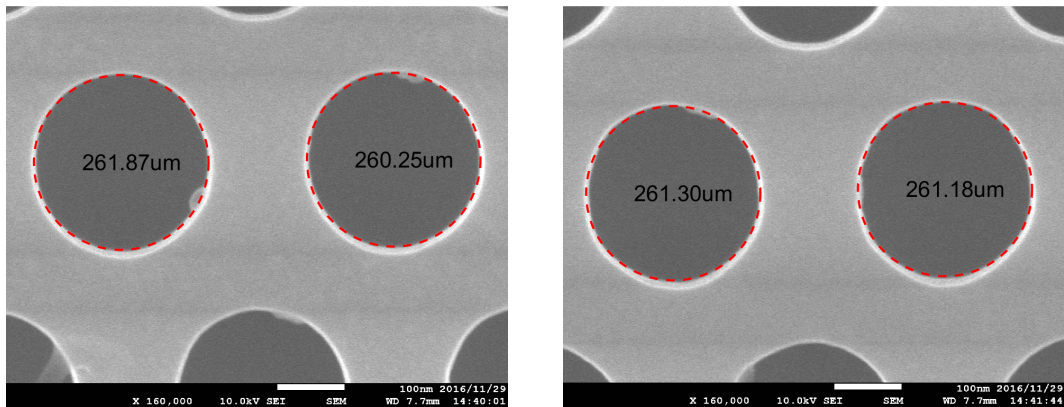


Fig. 3.6. SEM images of KT-2, where hole size is designed as 225 nm. These are two examples of 20 images we took.

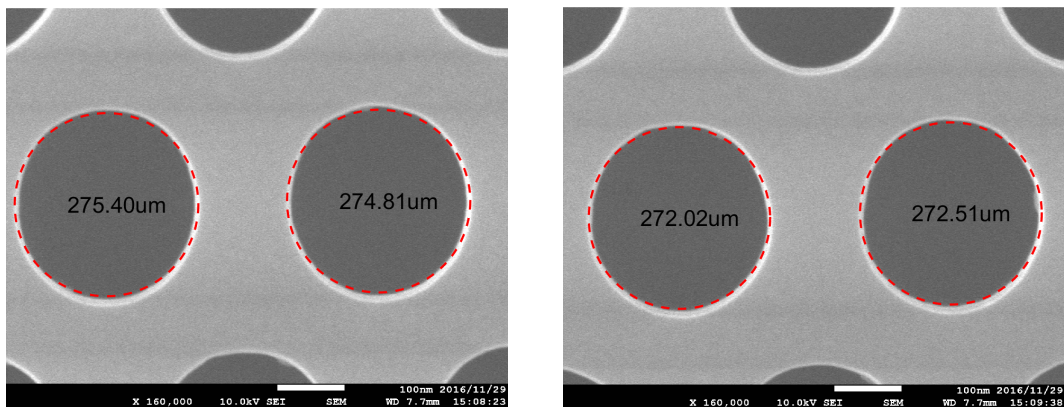


Fig. 3.7. SEM images of KT-2, where hole size is designed as 230 nm. These are two examples of 20 images we took.

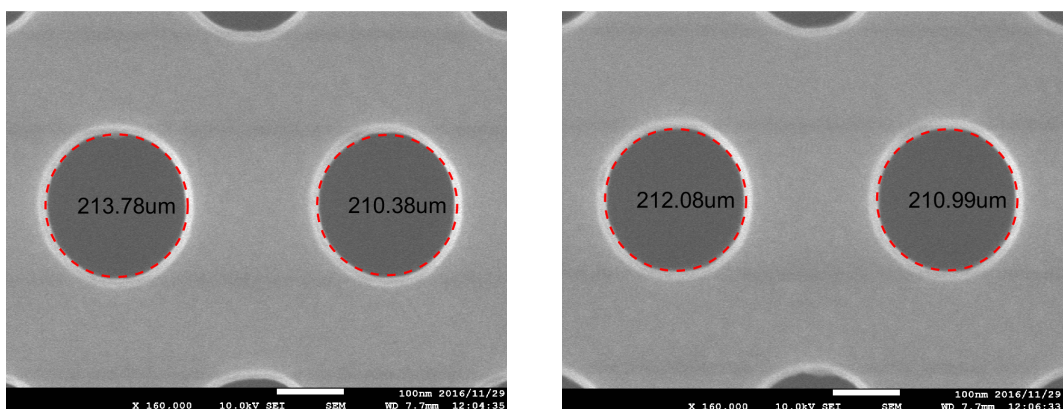


Fig. 3.8. SEM images of KT-3, where hole size is designed as 220 nm. These are two examples of 20 images we took.

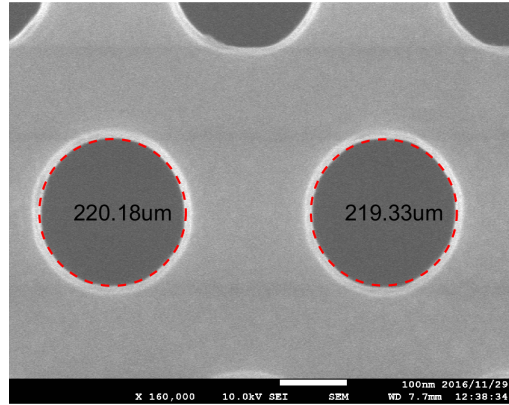
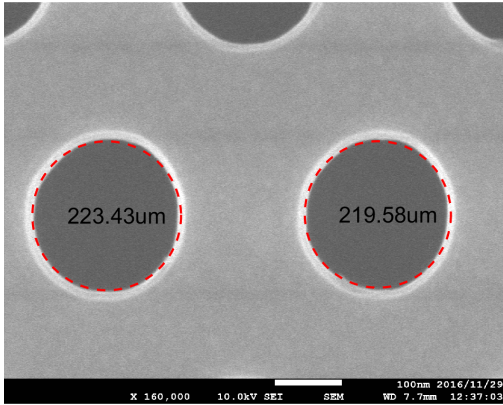


Fig. 3.9. SEM images of KT-3, where hole size is designed as 225 nm. These are two examples of 20 images we took.

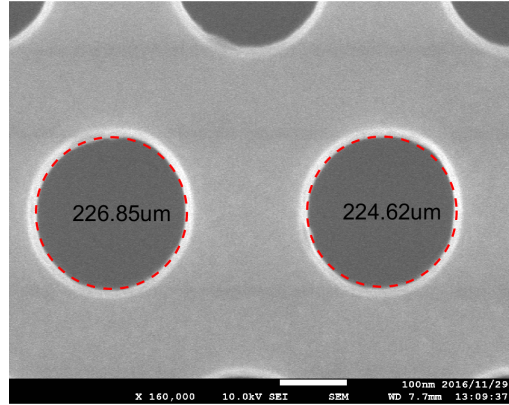
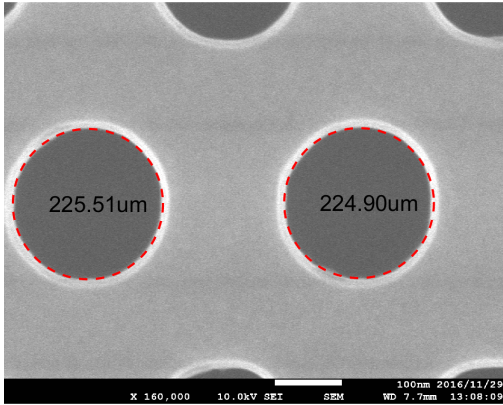


Fig. 3.10. SEM images of KT-3, where hole size is designed as 230 nm. These are two examples of 20 images we took.

Samples of scanning electron microscope (SEM) images are shown in Figs. 3.3-3.10. The measurement was conducted for 40 holes in each chip and each pattern. The fitting circles are overwritten on the SEM images. All of the fitting procedure are managed with a MATLAB code. At first, noise on SEM images are eliminated with a Gaussian filter by using the filter to every pixels in a captured SEM image.

$$\mathbf{G} = \begin{bmatrix} f(-2, -2) & f(-1, -2) & f(0, -2) & f(1, -2) & f(2, -2) \\ f(-2, -1) & f(-1, -1) & f(0, -1) & f(1, -1) & f(2, -1) \\ f(-2, 0) & f(-1, 0) & f(0, 0) & f(1, 0) & f(2, 0) \\ f(-2, 1) & f(-1, 1) & f(0, 1) & f(1, 1) & f(2, 1) \\ f(-2, 2) & f(-1, 2) & f(0, 2) & f(1, 2) & f(2, 2) \end{bmatrix} \quad (3.2)$$

$$f(x, y) = \frac{1}{2\pi\sigma^2} e^{\left(-\frac{x^2+y^2}{2\sigma^2}\right)} \quad (3.3)$$

$\mathbf{G}$  in Eq. (3.2) represent the Gaussian filter, and function  $f$  in  $\mathbf{G}$  is described in Eq. (3.3). We took  $\sigma$  as 1 in our analysis. Next, the gradient at every pixel is calculated with matrixes in Eq. (3.4).

$$\mathbf{G}_x = \begin{bmatrix} -1 & 0 & 1 \\ -2 & 0 & 2 \\ -1 & 0 & 1 \end{bmatrix}, \mathbf{G}_y = \begin{bmatrix} 1 & 2 & 1 \\ 0 & 0 & 0 \\ -1 & -2 & -1 \end{bmatrix} \quad (3.4)$$

The direction and the magnitude of the gradient;  $I_{dir}$  and  $I_{mag}$ , are calculated with Eq. (3.5).

$$I_{dir} = \tan^{-1} \frac{|\mathbf{G}_y|}{|\mathbf{G}_x|}, I_{mag} = |\mathbf{G}_x| + |\mathbf{G}_y| \quad (3.5)$$

And then, it is checked whether a pixel is a candidate for the edge of a hole or not; take  $3 \times 3$  pixels around the pixel, compare  $I_{mag}$  of neighboring two pixels in the direction of  $I_{dir}$ , and take the pixel as a candidate for the edge if its  $I_{mag}$  is bigger than neighbor's one. The candidate is considered as a part of the edge of a hole when its  $I_{mag}$  is bigger than signified threshold,  $T_{max}$ . The edge of a hole is supposed to be connected, so even if a candidate has less  $I_{mag}$  than  $T_{max}$ , it can be considered as a part of edge when its  $I_{mag}$  is over  $T_{min}$  and there is a pixel has  $I_{mag}$  more than  $T_{max}$  in surrounding  $3 \times 3$  pixels.

This algorithm to detect edge is called as Canny edge detection, where we have to signify  $T_{max}$  and  $T_{min}$  in order to define the condition of the edge. These  $T_{max}$  and  $T_{min}$  should not be changed for all SEM images because changing them means the definition of the edge of a PhC hole is changed and it leads to incorrect measurement. Those can be changed, however, when brightness or/and contrast of SEM images are changed.

Finally, a fitting circle is calculated with the information of the edge points. In

Eq. (3.6), coordinates of the center of the fitting circle and the radius represent as  $x_0, y_0$  and  $r$ , respectively.  $X$  and  $Y$  are coordinates of the pixels considered as the edge.

$$[X \ Y \ 1] \cdot \begin{bmatrix} -2x_0 \\ -2y_0 \\ x_0^2 + y_0^2 - r^2 \end{bmatrix} = -(X^2 + Y^2) \quad (3.6)$$

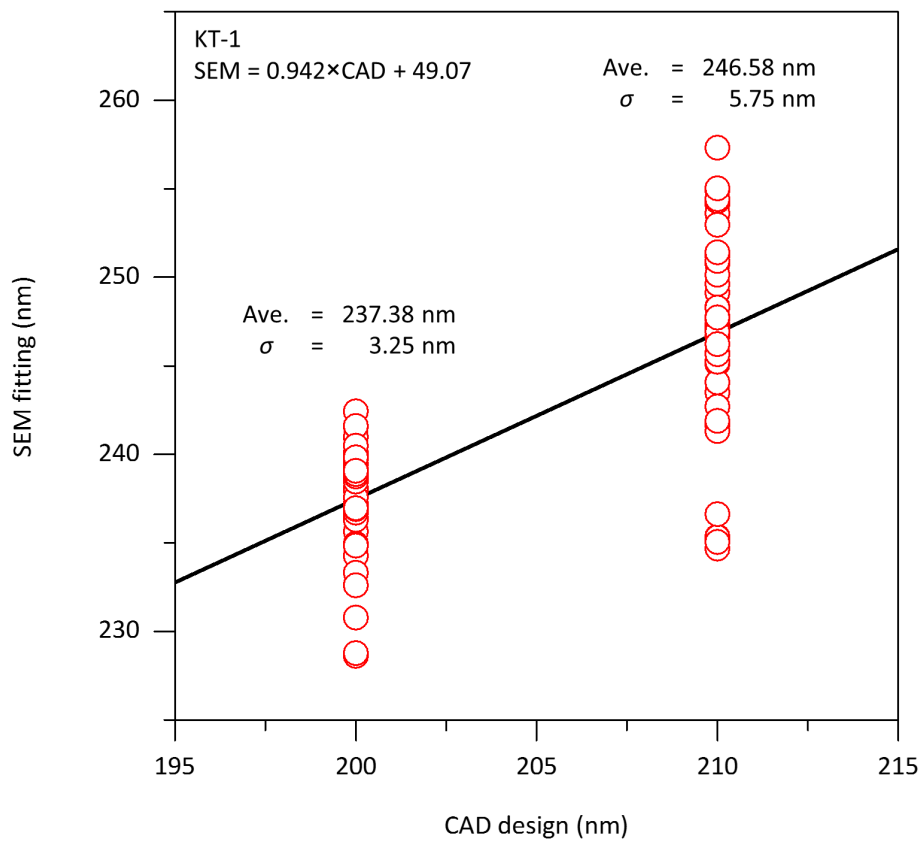


Fig. 3.11. The relationship in KT-1 between the designed hole size in CAD software and the measured hole size with SEM images and fitting.

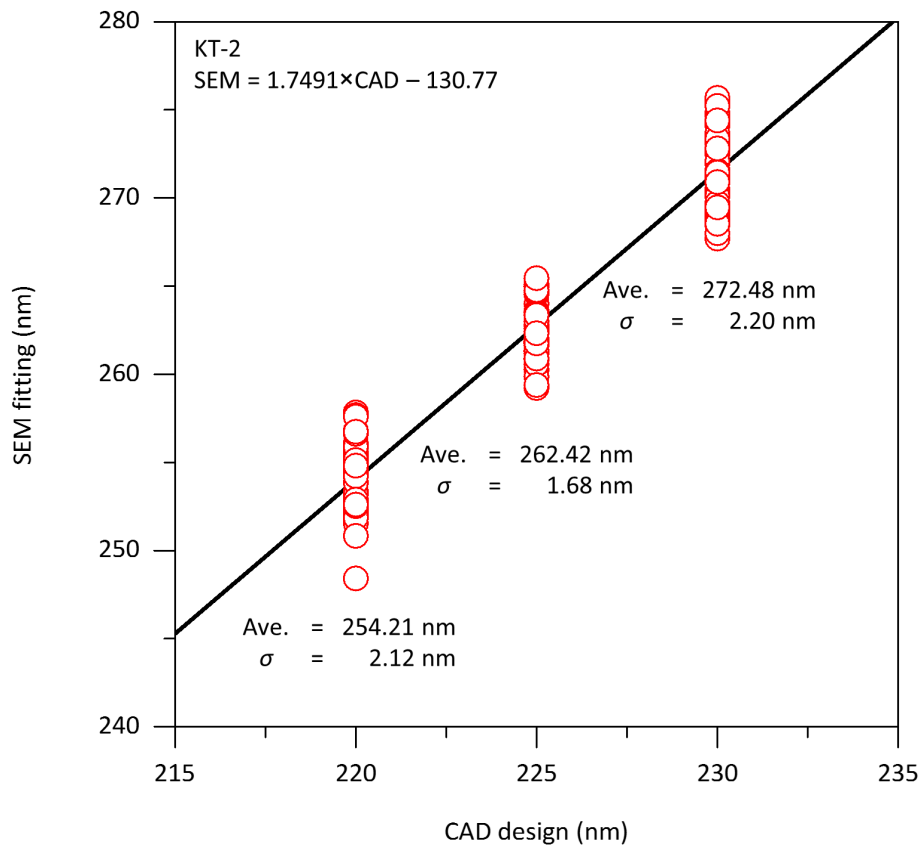


Fig. 3.12. The relationship in KT-2 between the designed hole size in CAD software and the measured hole size with SEM images and fitting.

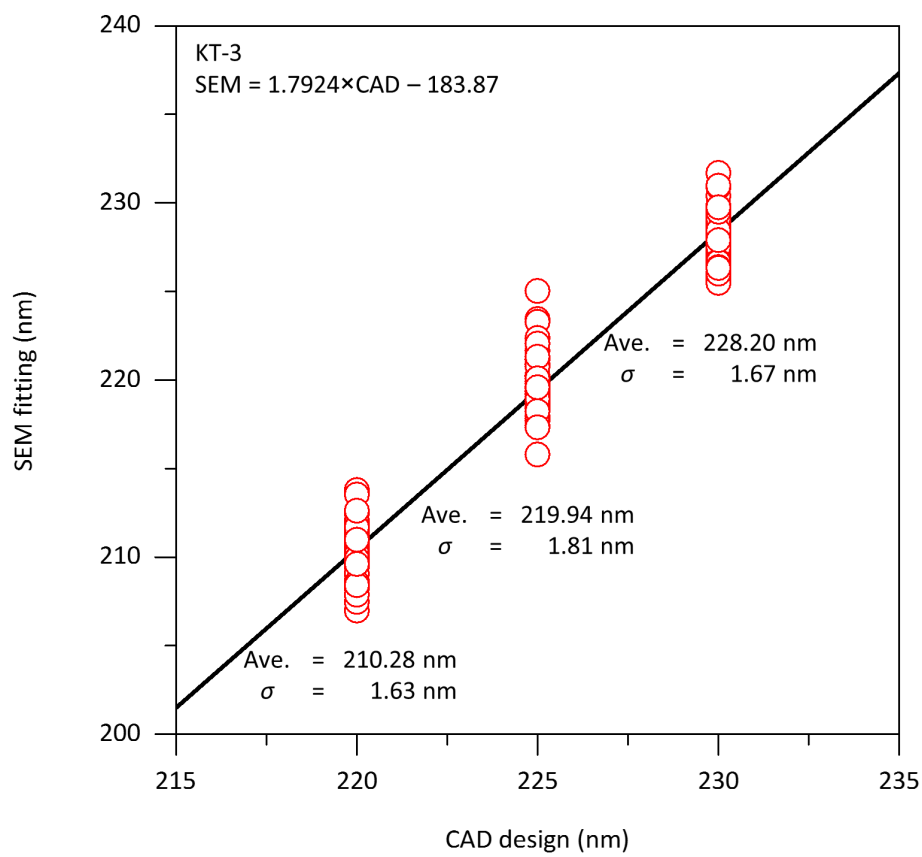


Fig. 3.13. The relationship in KT-3 between the designed hole size in CAD software and the measured hole size with SEM images and fitting.

SEM measurement and the fitting are summarized in Figs. 3.11-3.13. Until the SEM measurement with Canny edge detection was developed, we had used measurement software that has been installed in SEM machines, FEI Inspect F50 and JEOL JSM - 7600F. However, the measurement software could measure distance only in horizontal or vertical direction. We think the results below are more correct than those in Ref. [35] and [92], but still we are not sure how much we can believe those results. This is because we are afraid there may be three problems listed below.

- The shape of a PhC hole is not a perfect circle
- The center positions of PhC holes cannot be evaluated
- Scale bar in the SEM images may be wrong

Our measurement and fitting assume that the shape of a PhC hole is a perfect circle, but the actual shape is not perfect. In Fig. 3.5, for example, it can be seen that there are gaps between PhC holes and fitting circles drawn in red broken lines. PhC holes are somehow ellipses and include ripples along the edge of holes. There have been some researches that consider those disorder effect to PhC waveguides [48,49]. The center of PhC hole's positions cannot be precisely evaluated. In the situation where the positions are measured, it is necessary to capture an SEM image with large area. However, when zooming out, an SEM image has less resolution. We can estimate the order of deviation in the hole position is a couple of nanometers from the deviation in the diameter. It is difficult to detect that nanometer order with a zoomed out SEM image. Finally, the scale bar in the SEM images shown in Figs. 3.3-3.10 is not credible. The lattice constant,  $a$ , is designed to be 420 nm, but it shows 408-411 nm in Figs. 3.3-3.10 when it is measured using the scale bar. We believe that our PhCs are fabricated with  $a$  of around 420 nm because it matches well with the result of three-dimensional finite-difference time-domain (FDTD) calculation [35].

There have been some points yet to be clear, but we think these are reasonable things that should be taken granted through our analysis above.

- KT-1 has deviation of 3.2-5.8 nm
- KT-2 and -3 have deviation of 1.5-2.2 nm
- Lattice constant is around 420 nm

From these points, we should rethink our mention in Ref. [35], where we noted that the deviation in hole diameter is around 1.6 nm. The sample used in that study is KT-1, so the deviation might have been around 3.2-5.8 nm. Interestingly, this value matches more to the calculation results considering the effect of deviation to  $Q$  factor. Average hole diameter is measured as 237.38 nm this time, but we mentioned 244 nm. This difference comes from the fact that we used different samples fabricated in the same process, KT-1. Also, in Ref. [92], we included deviation of 2 nm in hole diameter and position. Although the actual deviation in the position has not been clear, those values are good parameter because the sample used in Ref. [92] was KT-1, and it can be estimated that the effect of 3.2-5.8 nm deviation in hole diameter is as much as that of 2 nm deviation in hole diameter and position.

### **3.4 Summary**

In summary, three different chips of PhCs fabricated with photolithography are observed and analyzed with SEM images. Those chips are named as KT-1, KT-2 and KT-3. KT-1 was fabricated with a HDM, and it has deviation of 3.2-5.8 nm in its hole diameter. KT-2 and KT-3 were fabricated with a PSM, and have deviation of 1.5-2.2 nm. This value is close to the deviation in EB lithography around 0.33-1.1 nm [93,94].

# Chapter 4

## Utilization of randomness in PhCs

In this chapter, the fundamental analysis for randomness in PhC waveguides is conducted with a noble design named as hetero-width (HW) PhC waveguides (PCWG). Using the HW PCWGs, it is set as a target to control and utilize randomness in PhCs. The relationship is investigated between the length of HW PCWG and  $Q$  factor, and between the length of HW PCWG and yield rate. Finally, on the basis of confinement from controlled randomness in HW PCWG, an electro-optic modulator is demonstrated at the speed of 1 GHz.

### 4.1 Introduction

PhCs are a great candidate for future silicon photonics since PhCs confine light strongly (large  $Q$ ) in a small mode volume (small  $V$ ). These abilities of PhCs have been investigated by many studies, which are described in Sec. 1. In order to fully extract their abilities, disorder in PhCs have sometimes been considered as a hindrance. This is because disorder can deteriorate  $Q$ , transmittance and so on. There have been many researches that examine how disorder affects in PhCs and how to reproduce disorder effects in simulation. The history is also described in Sec. 1. On contrary, some studies have been trying to utilize disorders in PhCs for random lasers. Those are based on localization of light that comes from randomness, but it is often difficult to use them in practical application. Those cannot control the position of the localization and the laser

emission direction. I set a target to tackle the difficulties by controlling and utilizing randomness in PhCs.

## 4.2 Model and theory to investigate randomness in PhCs

It has been getting important to understand the effect of randomness, because our PhC devices have been fabricated with photolithography that contains larger fabrication errors than that of EB lithography. Studies on random PhC lasers have often been more based on theoretical than practical motivation, where it is difficult to utilize them as practical devices because they are dominated by probability and cannot be controlled in the position of localization and in the direction of laser emission. Although it is impossible to control randomness completely (this may sound contradictory), PhC devices based on fabrication error, or randomness, can be utilized in practical applications if there is a way to control them.

PCWGs used in this study are almost the same as other studies, but a trick is installed in the structure that is named as a hetero-width (HW) PCWG, where the width of a PCWG is changed at a certain area. This enables to control the effect of randomness. A HW PCWG is based on triangle lattice and consists of W0.98 waveguide at the center area which is 98% of the width of original W1 line defect [Fig. 4.1(a)]. W0.98 waveguide is in between W1.05 waveguides. Figure 4.1(b) shows the dispersion diagram of a HW PCWG, where the horizontal axis represents position of the HW PCWG corresponding to Fig. 4.1(a). Since the width of W0.98 is narrower than W1.05, the mode-gap frequency of W0.98 is higher than W1.05, which is described as the height of colored areas, orange and blue, in Fig. 4.1(b). The mode-gap frequency is ideally flat along with entire W0.98 or W1.05 in the designed structure [Fig. 4.1(b)]. When light at the frequency between mode-gap of W0.98 and W1.05 is injected from left side, the light reflects at the edge of W0.98 and does not transmit to the other side as described as a red arrow in Fig. 4.1(b).

In case of our fabricated device, however, disorder exists in WH PCWG and it fluctuates the mode-gap frequencies. The chips used in this section is KT-1 and it is assumed that deviation of 3.2-5.8 nm is included in its diameter. As a result, light

supposed to reflect at the edge of W0.98 tunnels and reaches the output if the light has frequency close to the mode-gap at W0.98 PCWG, as shown in Fig. 4.1(c). Moreover, light can be confine only at W0.98 PCWG. The point of this design is that randomness in HW PCWG appears only in W0.98 PCWG and the fluctuation of mode-gap frequency in W1.05 does not influence the transmittance of the device since its mode-gap frequency is well-below compared to that of W0.98. It can be said that “randomness” is “controlled” only in arbitral region. This enables an electro-optic (EO) modulator driven by light confinement at W0.98 PCWG with a structure integrated *p-i-n* junction on both side of W0.98 PCWG.

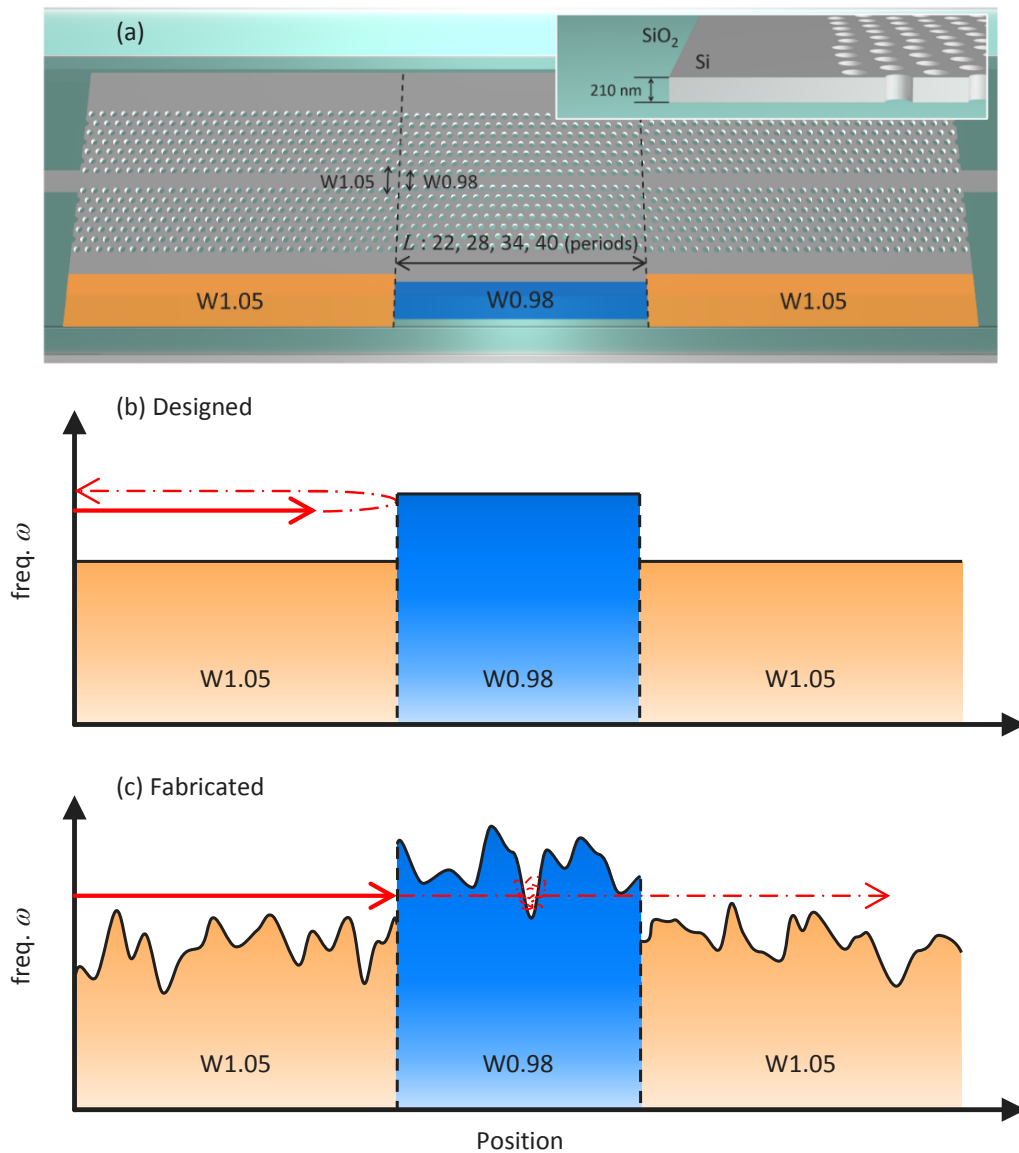


Fig. 4.1. (a) Designed structure of HW PCWG, which consists of a W0.98 waveguide in between W1.05 waveguides. This two-dimensional PhC is based on a silicon slab with a hexagonal lattice clad with SiO<sub>2</sub>. The inset shows the facet structure. (b) Band structure of designed (ideal) HW PCWG. Blue and orange indicate the stop-band of the PCWG. The red arrow indicates the input light injected from the left side of the structure. (c) As (b) for the fabricated device containing disorder [92] [Reprinted with permission from Y. Ooka, N. A. B. Daud, T. Tetsumoto, and T. Tanabe, “Compact resonant electro-optic modulator using randomness of a photonic crystal waveguide,” *Opt. Express* **24**, 11199–11207 (2016).].

There is transition of regimes for slow-light in PCWGs, which was discussed in Sec. 1. Localization length  $l$  is defined as  $l^{-1} = -\langle \ln T \rangle / L$ , where  $T$  and  $L$  is the transmittance and the length of the device, respectively. When  $l \gg L$ , light is in “dispersive regime” where backscattering in a PCWG is dominant. When  $l \approx L$ , it is in “diffusive regime” where backscattered light couples to a PCWG mode and spatial confinement happens. Finally, when  $l \ll L$ , light is in “localized regime” where

Two-dimensional finite-difference time-domain (2D-FDTD) calculation is performed for HW PCWG with different four length ( $L$ : 22, 28, 34 and 40 periods) of W0.98 PCWG. The lattice constant  $a = 420$  nm, the hole radius  $r$  is described as  $r/a = 0.345$ , the effective refractive index of slab  $n_{\text{eff}} = 2.81$  and that of ambient;  $\text{SiO}_2$ ,  $n_{\text{amb}} = 1.44$ . Randomness is taken into consideration in the calculation, where deviation in hole radius  $\sigma_{\text{rad}}$  and position  $\sigma_{\text{pos}}$  are 1 nm and 2 nm, respectively. Figure 4.2 shows schematic of the relationship among designed hole,  $\sigma_{\text{rad}}$  and  $\sigma_{\text{pos}}$ . As discussed in Sec. 3, the amount of deviation estimated here in  $\sigma_{\text{rad}}$  and  $\sigma_{\text{pos}}$  describes the effect of randomness in KT-1 well that, in SEM measurement, has 3.2-5.8 nm deviation in its hole diameter. Hole position shifts with distance of  $\sigma_{\text{pos}}$  and random direction;  $\theta$ . One of calculated transmission spectrum with  $L$  of  $40a$  is shown in Fig. 4.2(b), which has a sharp peak around the band-edge. This sharp peak can be utilized for practical devices because it enhances light-matter interaction. Figure 4.2(c) display a mode profile of the peak. This proves that light at the peak wavelength is confined only in W0.98 PCWG. This is our expected result in which randomness in W1.05 PCWG does not influence.

I performed 18 calculations with different random seeds. From the relationship between  $l$ ,  $L$  and  $T$ , one can calculate in which regimes the peak is.  $\langle \rangle$  signs describe the ensemble average.  $l = 18 \mu\text{m}$  is calculated when  $L$  was  $16.8 \mu\text{m}$  ( $L = 40a$ ), which is in “diffusive regime.” The peak around the mode-gap that appears in Fig. 4.2(b) has high transmittance, which is a good point of a PCWG in diffusive regime.

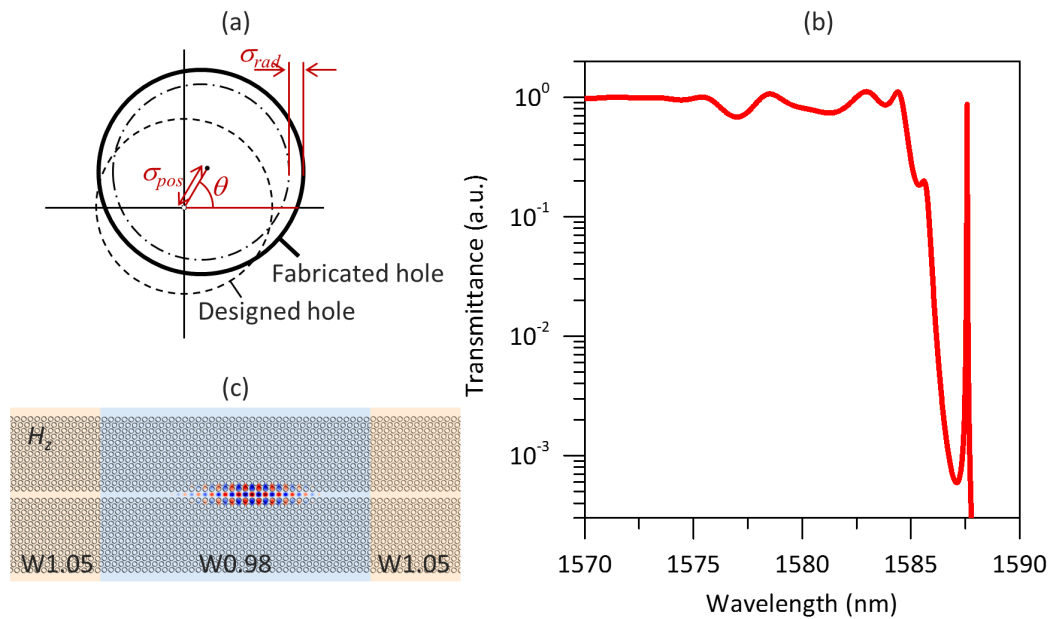


Fig. 4.2. (a) Schematic illustration of the hole position and radius with deviation  $\sigma_{pos}$  and  $\sigma_{rad}$ .  $\sigma_{pos}$  of 2 nm and  $\sigma_{rad}$  of 1 nm is used in our 2D-FDTD calculation. (b) Transmission spectrum for W0.98 length of  $L = 40a$ . A sharp peak appears close at the mode gap at 1587.5 nm. (c) Calculated spatial distribution of  $H_z$  component when light at the wavelength of the peak shown in (b) is excited [92] [Reprinted with permission from Y. Ooka, N. A. B. Daud, T. Tetsumoto, and T. Tanabe, “Compact resonant electro-optic modulator using randomness of a photonic crystal waveguide,” *Opt. Express* **24**, 11199–11207 (2016).].

Through the same procedure, it is confirmed that all four lengths ( $L = 22-40$ ) are in the diffusive regime and light confinement occurs only in the W0.98 PCWG. This limitation for the area where light is confined makes it possible to integrate the HW PCWG with a *p-i-n* diode. Longer PCWGs have low transmittance and get rid of controllability of the position where light confines or localizes. In order to utilize the light confinement in diffusive regime, it is necessary to figure out the relationship between the lengths of W0.98 PCWG versus the yield rates of the light confinement. This provides the probability of the fabrication of HW PCWGs devices successfully. In the next section, experimental results are shown, and the yield rates are discussed.

## 4.3 Experimental results

### 4.3.1 Transmission spectra & confinement area

First of all, the setup to measure the transmission spectra is described. Figure 4.3 shows images of the setup to fix a chip and couple input/output lights to a chip with lenses.

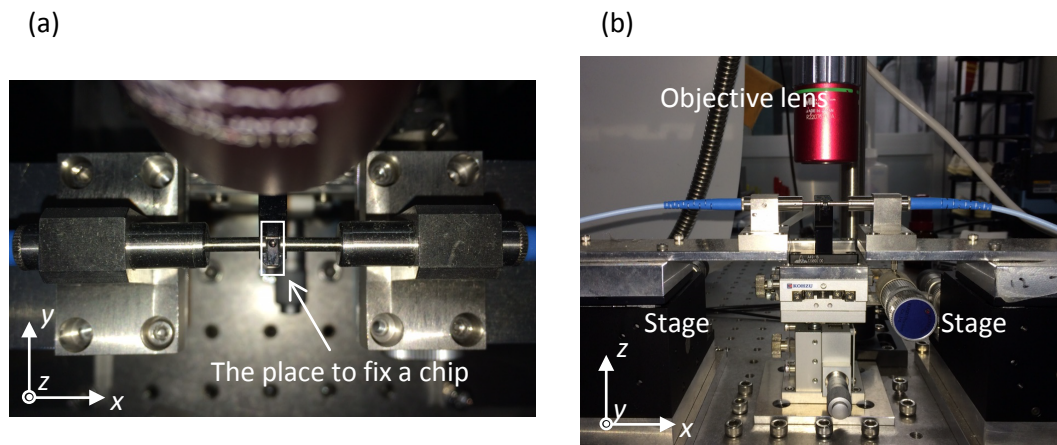


Fig. 4.3. Pictures of the measurement setup to fix a chip from (a) the top of the chip and (b) the front side. A chip is fix with vacuum. The Objective lens capture images with an inferred camera.

Figure 4.3(a) shows a schematic of our HW PCWG integrated with  $p-i-n$  junction. The doping concentration is  $2.4 \times 10^{17} \text{ cm}^{-3}$  and  $1.4 \times 10^{17} \text{ cm}^{-3}$  in  $p$ - and  $n$ -region, respectively. These two regions are implanted at the center of W0.98 PCWG. The width of the regions is  $4a$  and connected to aluminum pads to apply voltage (the results are shown in Sec. 4.3.3 in detail).  $i$ -region is set with distance of  $2.9 \mu\text{m}$  between  $p$  and  $n$ . KT-1 chips has  $r/a = 0.294$ .

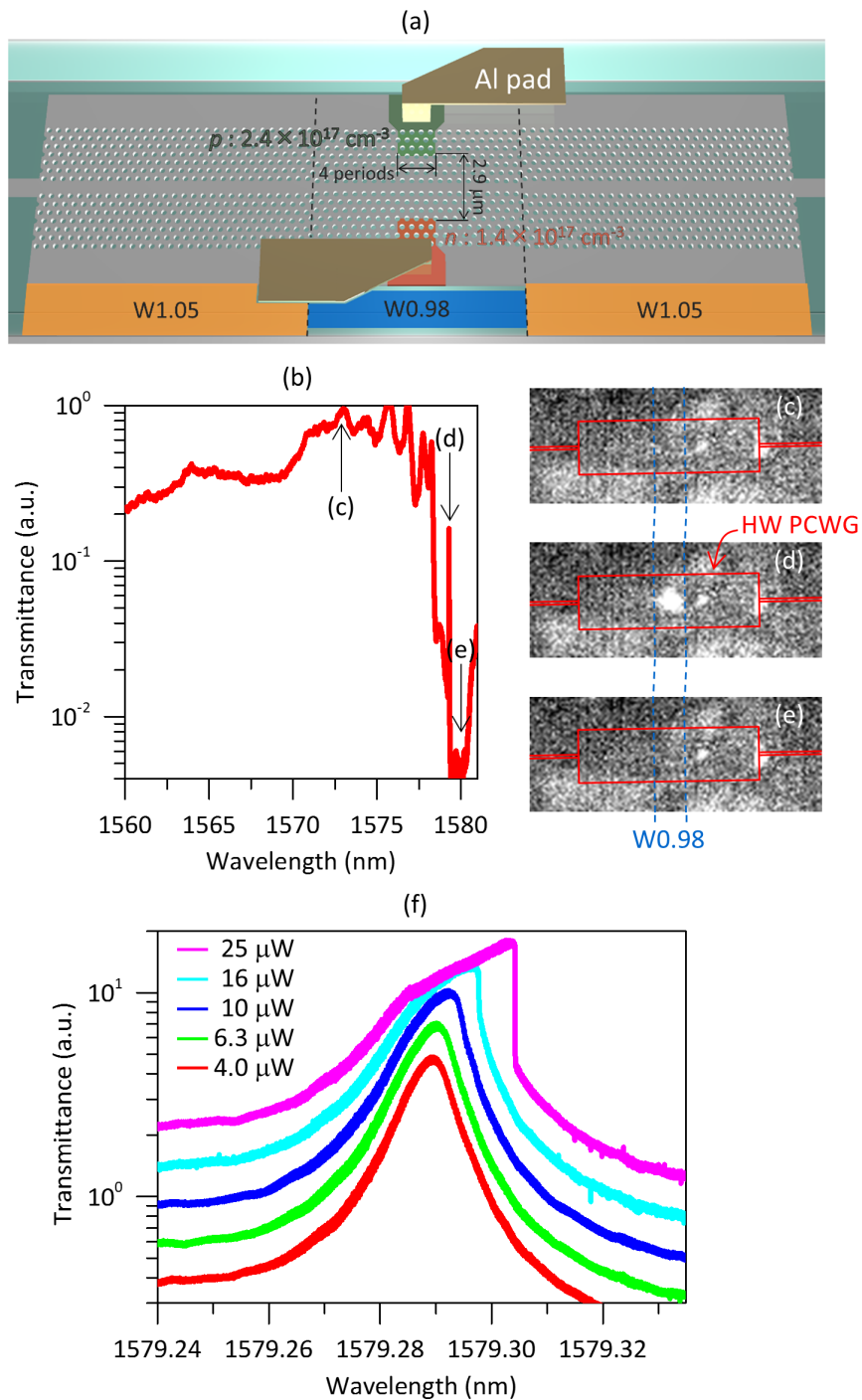


Fig. 4.4. (a) Schematic illustration of the fabricated device. The device is clad with SiO<sub>2</sub>. (b) A transmission spectrum for a device with  $L = 40a$ . The confined mode appears at the mode gap and the  $Q$  value is  $1.5 \times 10^5$ . (c)-(e) Infrared camera images taken from the top of the slab. The corresponding

input wavelength is shown with arrows in (b). Light is injected from the right of the images. Red rectangles denote the area of the HW PCWG and the blue dotted line shows the W0.98 PCWG. The horizontal red lines are the input/output silicon nanowire waveguides. (f) Magnified image of the peak in (b) with different input powers [92] [Reprinted with permission from Y. Ooka, N. A. B. Daud, T. Tetsumoto, and T. Tanabe, “Compact resonant electro-optic modulator using randomness of a photonic crystal waveguide,” *Opt. Express* **24**, 11199–11207 (2016).].

Transmission measurement is conducted with four different lengths of W0.98 PCWG and with 18 devices corresponding each length. One of the transmission spectra is shown in Fig. 4.3(b), where a shape peak around the mode-gap is similar to the calculation shown in Fig. 4.2(b).  $Q$  of this peak is  $1.5 \times 10^5$ , which is enough to demonstrate an electro-optic modulator. The highest  $Q$  obtained through those measurement is  $2.4 \times 10^5$  with a different chip. The transmittance of the peak is over 10%, which indicates that light in the peak is in “diffusive regime.” This matches the calculation results.

Figure 4.3(c)-4.3(e) are infrared camera images taken from the top of the PhC slab when light different wavelengths is injected from right to left. The wavelengths which are injected in each image are shown as arrows in Fig. 4.3(b). When the input wavelength is at the peak, only W0.98 PCWG becomes bright [Fig. 4.3(d)]. This means that light confinement happens in W0.98 PCWG and the area to confine light is controlled.

Here, confinement of light is also investigated, where non-linear effect is measured because it happens when light confined strongly. As the optical power is increased, optical bistable phenomenon is observed, which derives from non-linear effect driven thermo-optic effect. This phenomenon appears when light is well confined in a small area and generates two-photon absorption. The transmission spectra in Fig. 4.3(f) shows the phenomenon, where wavelengths are scanned from blue to red.

### 4.3.2 Yield rate & multi-mode confinement

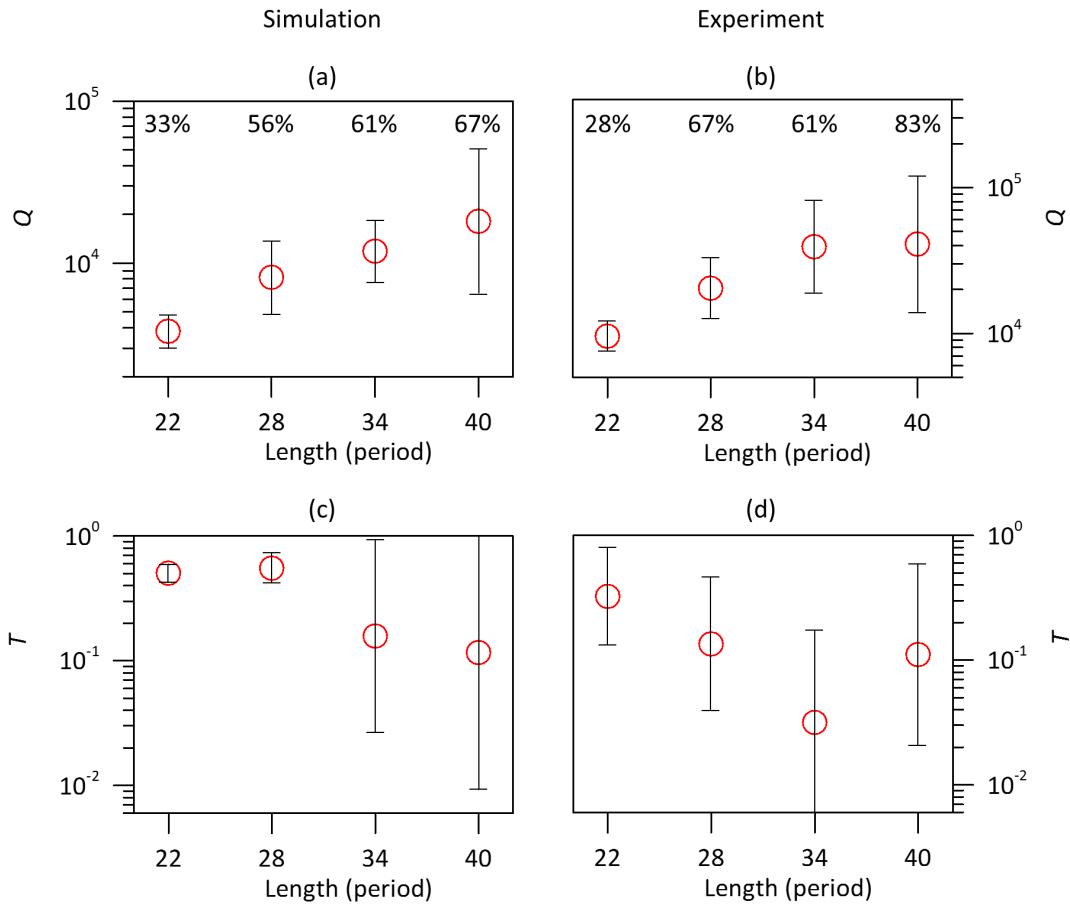


Fig. 4.5. Yield of a sharp peak for a simulation (a) and an experiment (b). Transmittance,  $T$ , corresponding to those peaks are shown in (c) and (d). Red circles exhibit the average and error bars are corresponding to standard deviation [92] [Reprinted with permission from Y. Ooka, N. A. B. Daud, T. Tetsumoto, and T. Tanabe, “Compact resonant electro-optic modulator using randomness of a photonic crystal waveguide,” *Opt. Express* **24**, 11199–11207 (2016).].

In order to further investigation for the applicability to practical situations, transmission measurements are conducted on 18 chips of the same design for each length of HW PCWG. Numerical analysis are conducted as same times as experiment. Figure 4.4 is the summary of the experimental and numerical analysis.  $Q$  values are shown in Figs. 4.4(a) and 4.4(b), and the transmittance  $T$  is shown in Figs. 4.4(c) and 4.4(d) with different lengths of W0.98 PCWGs. Most of experimental  $Q$ s are higher than  $10^4$ , and the highest

$Q$  reaches  $2.4 \times 10^5$ . The percentages in Figs. 4.4(a) and 4.4(b) represent the probability of the appearance of a sharp peak around the mode gap, where a peak is defined when the Lorentzian-fit power differs from the top to the bottom more than 10 dB. Here, it can be seen that the yield rate of a high- $Q$  peak increases when the length of W0.98 PCWG,  $L$ , increases. The trend of  $Q$ ,  $T$  and yield rate of the simulation and experiment agrees well, and it is proven experimentally that over 80% of the HW PCWG with  $L$  of  $40a$  including randomness shows high- $Q$ s. This is great value when practical applications are considered. In addition,  $L$  of  $40a$  is short enough for the center  $p-i-n$  junction to overlap the area of light confinement.

Transmission spectra of HW PCWGs with an  $L$  of  $100a$  are calculated to show longer PCWGs have low transmittance and low controllability of the light confinement position. Figure 4.5 shows one of the results. It shows two sharp peaks around the mode-gap, while just one peak could be seen with  $L$  of  $22a$  to  $40a$ . Moreover, the light confines widely along the W0.98 PCWG, which means that it is difficult to make the  $p-i-n$  junction to overlap the area of light confinement. If a wider  $p-i-n$  junction is implanted along the W0.98 PCWG, it will be difficult to demonstrate high frequency EO modulation because carriers injected by applying the voltage remain along the W0.98 PCWG.

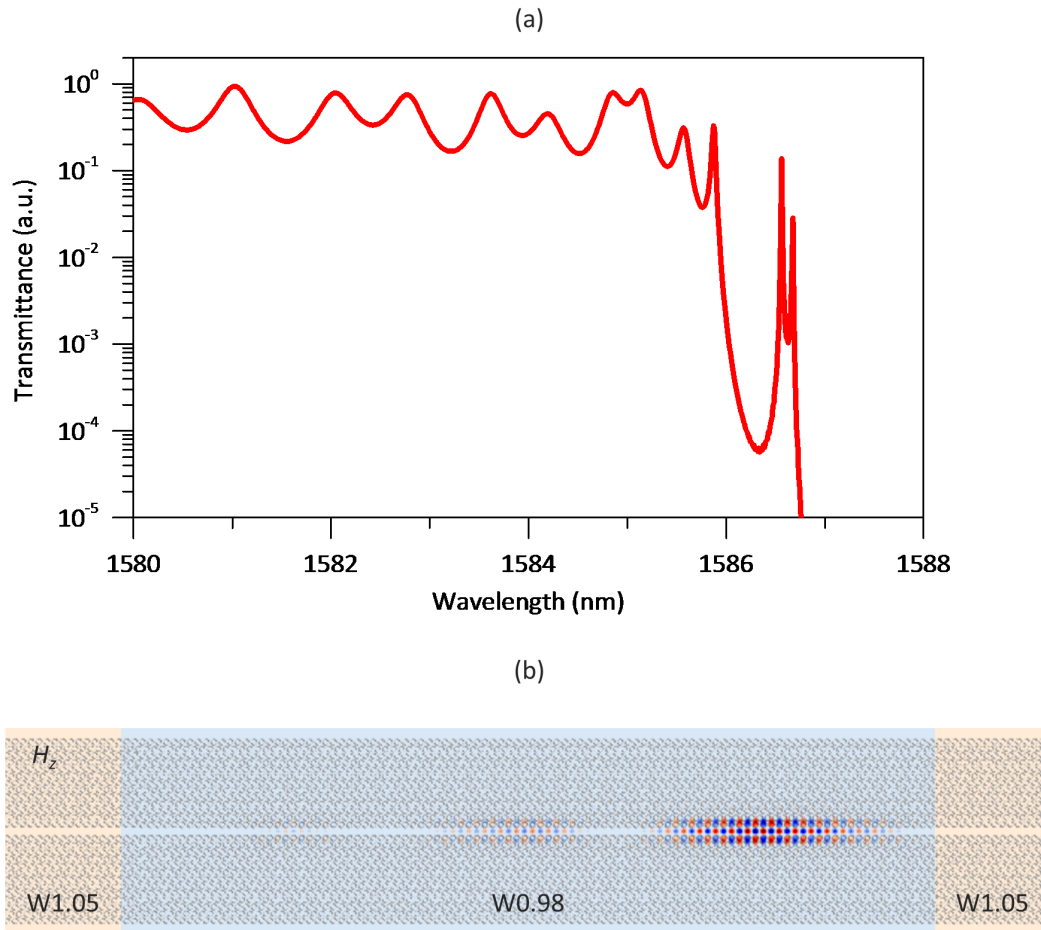


Fig. 4.6. (a) Transmittance spectrum of a PhC-WG with  $L$  of 100 periods, which is obtained with a 2D-FDTD calculation. (b) Field distribution when the structure is excited with  $1586.6 \text{ nm} \pm 0.1 \text{ nm}$  wavelength light [92] [Reprinted with permission from Y. Ooka, N. A. B. Daud, T. Tetsumoto, and T. Tanabe, “Compact resonant electro-optic modulator using randomness of a photonic crystal waveguide,” *Opt. Express* **24**, 11199–11207 (2016).].

### 4.3.3 Electro-optic modulator

EO modulation is demonstrated using devices that have been discussed, where the same device is examined as shown in and discussed with Fig. 4.3(b) and 4.3(f). To show the  $p-i-n$  junction works for the demonstration of EO modulation, the resonance shift is measured when forward bias voltages are applied to the  $p-i-n$  junction. The results are shown in Fig. 4.6(b). It can be seen that the resonance shift occurs towards shorter wavelengths as applied voltage increases. The direction of the shift is due to the carrier-plasma effect, and the drop of the peak transmittance is due to free carrier absorption. This results proves that the  $p-i-n$  junction and the area of light confinement overlap well. The setup used in measurement of the demonstration of EO modulation is shown in Fig. 4.6(a). For this demonstration, continuous-wave laser lights at wavelengths around the confinement mode is employed as an input light, and the input lights are modulated at the random W0.98 PCWG with electrical radio-frequency (RF) signals with square pulse at the speed of 500 MHz or 1 GHz. The RF signals have amplitude of 2 V (-0.5 to 1.5 V). The demonstrations of EO modulation are shown in Fig. 4.6(c) and 4.6(d). Both on-to-off (red line) and off-to-on (black line) show clear modulation depths. The limitation for maximum modulation speed here, 1 GHz, originates in the speed of carrier diffusion in this HW PCWG. It does not in the working function of the randomness-based HW PCWG. The photon lifetime calculated from  $Q$  of  $1.5 \times 10^5$  corresponds to the modulation speed of up to 10 GHz. In addition, the maximum speed in this demonstration is similar to the device where a PhC nanocavity is designed to be fabricate [95]. It can be expected that the demonstration with a higher speed is conducted with this HW PCWG, because using the same photolithographic foundry a study realizes up to 10 GHz with Mach-Zehnder interferometric modulator [96]. This study, however, is based on slow-light PCWG that needs a longer distance ( $L \geq 500a$ ) of PCWG to obtain  $\pi$  phase shift and double PCWG for the interferometric function. Our device has a big advantage in terms of a small footprint. Changing the length of  $i$ -region, the width of  $p$ - and  $n$ -regions and the doping concentration are some of the candidates for optimizing the structure.

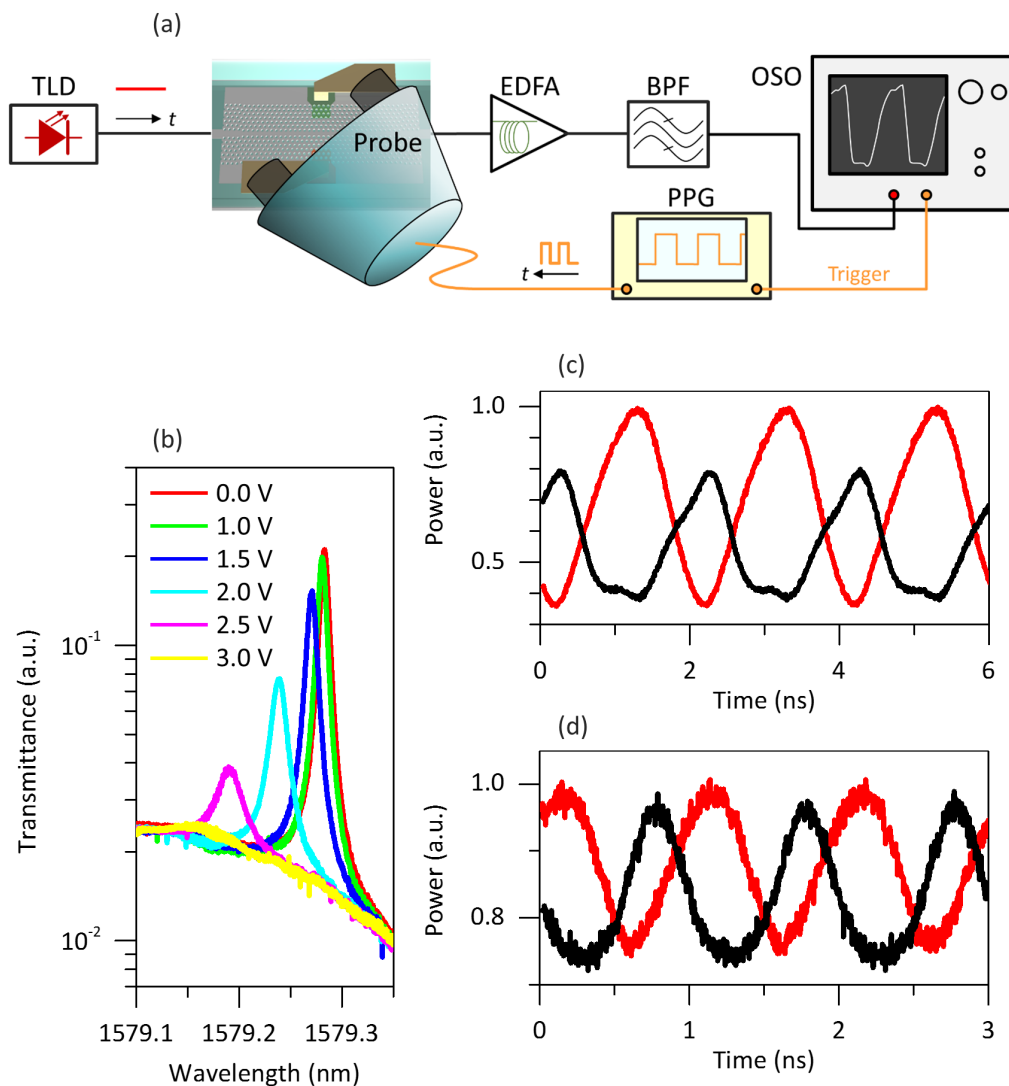


Fig. 4.7. (a) Schematic of the EO modulation demonstration. Input continuous wave laser light is modulated at a random HW PCWG device integrated with a pin junction. TLD: Tunable laser diode, EDFA: Erbium doped fiber amplifier, BPF: Bandpass filter (1-nm width), OSO: Optical sampling oscilloscope (Agilent 86103A), PPG: Pulse pattern generator (Keysight 81134A). (b) Transmittance spectrum of the confined mode at different forward bias voltages. (c) Detected output signals when a 500 MHz radio-frequency signal is applied. The red line is at the peak resonance, and the black line is when the input laser is slightly detuned at a wavelength shorter than the resonance. (d) As (c) but with 1-GHz modulation [92] [Reprinted with permission from Y. Ooka, N. A. B. Daud, T. Tetsumoto, and T. Tanabe, "Compact resonant electro-optic modulator using randomness of a photonic crystal waveguide," *Opt. Express* **24**, 11199–11207 (2016).].

## 4.4 Summary

The noble structure; HW PCWG, can control the appearance of randomness in the position of light confinement and the probability. The calculation model reproduces the experimental results very well. It is shown experimentally  $Q$ s exceed  $10^4$  routinely and that a yield rate is over 80%. The positions of those high- $Q$  modes are only limited in W0.98 PCWGs due to the controlled cut-off frequencies in HW PCWGs. EO modulation is also demonstrated to show the applicability of HW PCWGs. In this demonstration, a HW PCWG with a *p-i-n* junction at the center of a W0.98 PCWG is employed. It shows GHz EO modulation, which means randomness that drives from photolithography can be controlled and utilized in practical applications.

# Chapter 5

## PhC demultiplexers

In this chapter, more integrated devices on the silicon PhC platform are investigated. Previous chapters focus on components in PhCs; fabrication and randomness, which are basics for practical applications. Since the advantage of photolithography is its mass-productivity, integrated devices should be fabricated and analyzed in the next step. As one of integrated devices, demultiplexers (DeMUXs) are chosen in our study. The design this study proposes is described with some calculations, at first. Then optical measurements are shown, where transmittance and tunability of the devices are investigated. Another optical measurement is conducted in time domain, which shows eye-diagrams and crosstalk. To further improve our DeMUXs, optimization of the structure is conducted through FDTD calculations.

### 5.1 Introduction

DeMUXs have been developed in the field of silica arrayed waveguide gratings (AWGs). Silica AWGs have been developing and these are used in many commercial products, but they have been reaching the limit size in fabrication. It is difficult to expand the capacity of data transmittance with silica AWGs, although the expansion of data traffic seems ever-lasting. One of the devices that has been working on this problem is silicon AWGs. This is better for not only compatibility with other silicon photonic devices, but the size due to its higher refractive index. There is another candidate for replacing conventional

silica AWGs, silicon PhC DeMUXs. The main advantage PhC DeMUXs has is their small footprint. On the basis of the periodic structure, a silicon PhC confine light more tightly in a small area than bulk silicon does.

There have been some studies on silicon PhC DeMUXs, but those have some problems when applicability is considered. A DeMUX with the capacity of 32 channel-100 GHz spacing has been realized, and its footprint is  $4050 \mu\text{m}^2$ , which corresponds to  $100 \mu\text{m}^2$  per a channel [78]. Considering the total system in which this DeMUX is used practically, however, the direction of demultiplexed lights is out of a PhC slab and the system needs additional bulky optics. Although in-plane type DeMUXs have been demonstrated, these have a few channels and large spacing [70,74,75]. Thus, it is required to realize an in-plane driven PhC DeMUX with high capacity. In addition to those points, there are points need to be improved. These previous studies fabricated PhCs with EB lithography and with silica-clad, which relates to our target in the first place. PhC DeMUXs proposed in this chapter solve the problems and have great potential to be applied in practical situations.

## 5.2 Design of PhC DeMUXs

### 5.2.1 Design and working functions

A schematic of a proposed eight-channel DeMUX is shown in Fig. 5.1(a). PhCs and input/output nanowires are 210 nm thickness silicon slab clad with silica. This DeMUX consists of eight PhC nanocavities; width-modulated line defect type. Combined signals are first received at an input nanowire and propagate in an input W1.05 PCWG. Signals couple to nanocavities with resonant wavelengths corresponding to carrier wavelength of signals, and drop to output W1.05 PCWG. To tune resonant wavelengths of the nanocavities, the PhC has different lattice constant  $a$  in  $x$ -axis [69,74,76,78], where, technically speaking,  $a$  is not a lattice constant but the neighboring hole-to-hole distance in  $x$ -axis. Although Fig. 5.1(a) shows only eight-channel PhC DeMUX, 16-channel one is also fabricated. The difference of  $a$  in the  $x$ -axis between channels,  $\Delta a$ , is set at 1 nm and

0.5 nm in eight- and 16-channel DeMUXs.  $a_n = a_1 - \Delta a \times (n - 1)$ , where  $n$  is the number of channels and  $a_1$  is set at 420 nm. Eight- and 16-channel DeMUXs consist of  $a$  in  $x$  axis from 420 nm to 413 nm and 420 nm to 412.5 nm, respectively.

The silicon slab has under and over silica cladding and their cross-section is shown in Fig. 5.1(b). Because of silica cladding, the DeMUXs are not only stable to contaminant and mechanical oscillation, but able to integrate titanium nitride heaters above the silicon layer which can directly heat nanocavities to tune their resonant wavelengths.

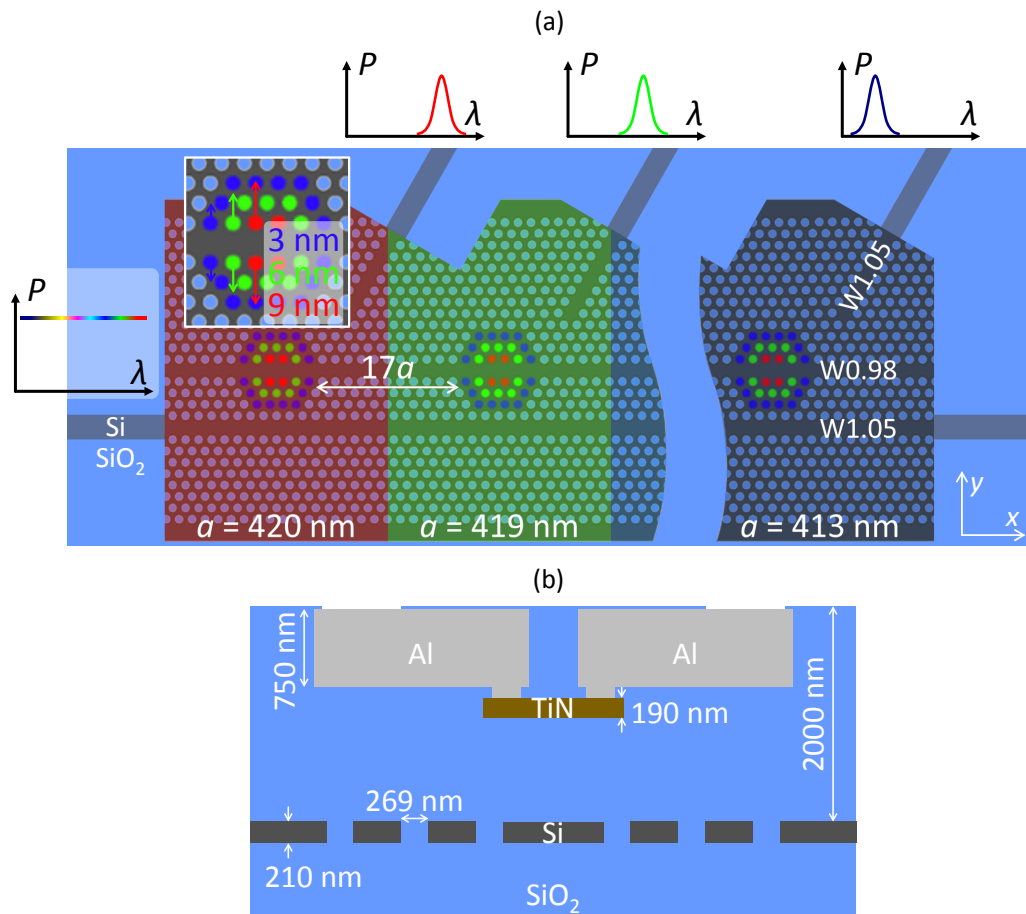


Fig. 5.1. (a) Schematic illustration of an eight-channel DeMUX. The hole diameter is 269 nm and the slab thickness is 210 nm. WM nanocavities are created by shifting the PhC hole positions 9, 6, and 3 nm. An eight-channel DeMUX has a step lattice constants of 1 nm. (b) Cross-section of DeMUX. Silicon PhCs have a 2000-nm-thick silica cladding. Titanium nitride heaters are embedded in the silica cladding and connected with aluminum wires [97] [Reprinted with permission from Y. Ooka, T. Tetsumoto, N. A. B. Daud and

T. Tanabe, “Ultrasmall in-plane photonic crystal demultiplexers fabricated with photolithography,” Opt. Express **25**, 1521–1528 (2017).].

## 5.2.2 Resonant wavelength and $Q$ factor analysis

Figure 5.1(c) summarizes the relationship between  $a$  in  $x$  axis and resonant wavelengths, which is obtained by conducting three-dimensional FDTD calculation. Figure 5.1(b) shows that linear resonance tuning can be achieved with this scheme. Width-modulated (WM) nanocavities are employed, while previous researches employed L3 nanocavities. This is because with L3 nanocavities  $Q$  reaches only the magnitude of  $10^3$  order in silica cladding. Through FDTD calculation, a WM nanocavity at channel 1 wavelength have intrinsic  $Q$  of  $6.1 \times 10^4$ , where the hole diameter, lattice constant and slab thickness are 269 nm, 420 nm and 210 nm, respectively.  $Q$  of more than  $10^4$  is required in dense channel spacing of 100 GHz [78], and moreover, high intrinsic  $Q$  makes high transmittance demonstration.

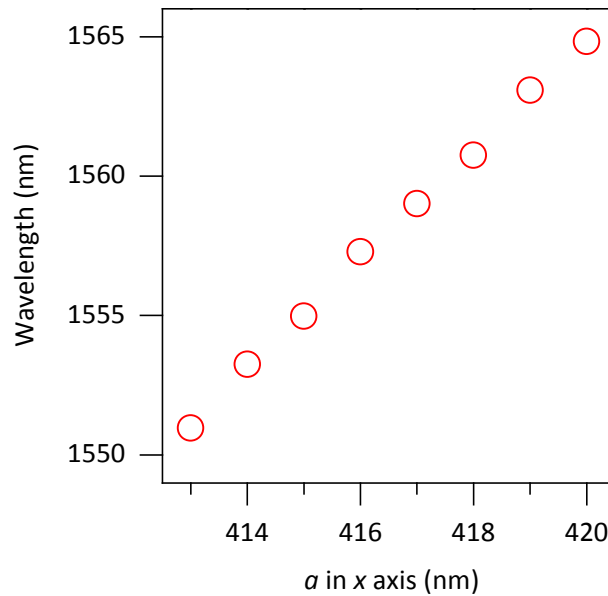


Fig. 5.2. Resonant wavelength of WM nanocavities, calculated with three-dimensional FDTD simulation [97] [Reprinted with permission from Y. Ooka, T. Tetsumoto, N. A. B. Daud and T. Tanabe, “Ultrasmall in-plane photonic crystal demultiplexers fabricated with photolithography,” Opt. Express **25**, 1521–1528 (2017).].

## 5.3 Results

### 5.3.1 DeMUX images

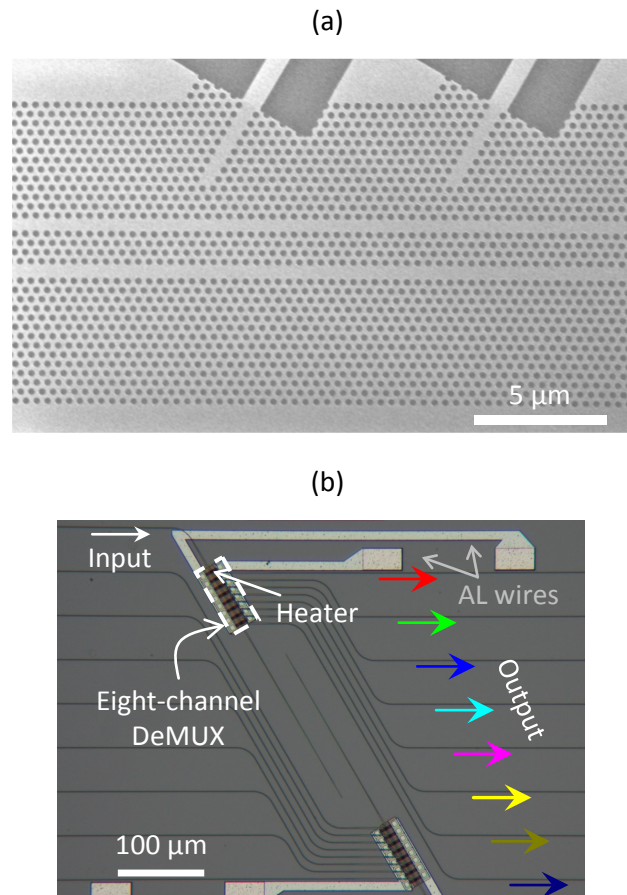


Fig. 5.3. (a) SEM image of a fabricated DeMUX. The silica cladding is removed for the SEM observation. (b) Optical microscope image of an eight-channel DeMUX [97] [Reprinted with permission from Y. Ooka, T. Tetsumoto, N. A. B. Daud and T. Tanabe, “Ultrasmall in-plane photonic crystal demultiplexers fabricated with photolithography,” *Opt. Express* **25**, 1521–1528 (2017).].

Figure 5.3(a) is an SEM image, which is taken after silica cladding of a DeMUX was removed with hydrofluoric acid. Figure 5.3(b) represents an optical microscope image of the entire system of eight-channel DeMUX with heaters. Voltage can be applied via

aluminum pads on the top surface, and titanium nitride heaters tune the resonant wavelengths. To couple input/output light from out of the chip to silicon nanowires, spot size converters (SSCs) are implemented. Coupling loss at a set of SSCs is estimated as 2.8 dB.

### 5.3.2 Transmission spectra & wavelength tuning

The transmission spectra of eight-channel DeMUXs are shown in Fig. 5.4 and 5.5, which correspond to KT-2 and KT-3, respectively. The DeMUXs in the KT-2 and KT-3 chip have hole diameter of 269 nm and 222 nm, respectively. These are calculated from the fitting lines in Figs. 3.12 and 3.13. The average channel spacing in the KT-2 eight-channel DeMUX is 267 GHz, and that of KT-3 is 242 GHz. In the transmittance measurement in Fig. 5.4 and 5.5, optical power of  $-20$  dBm and  $-10$  dBm are input in to the systems.

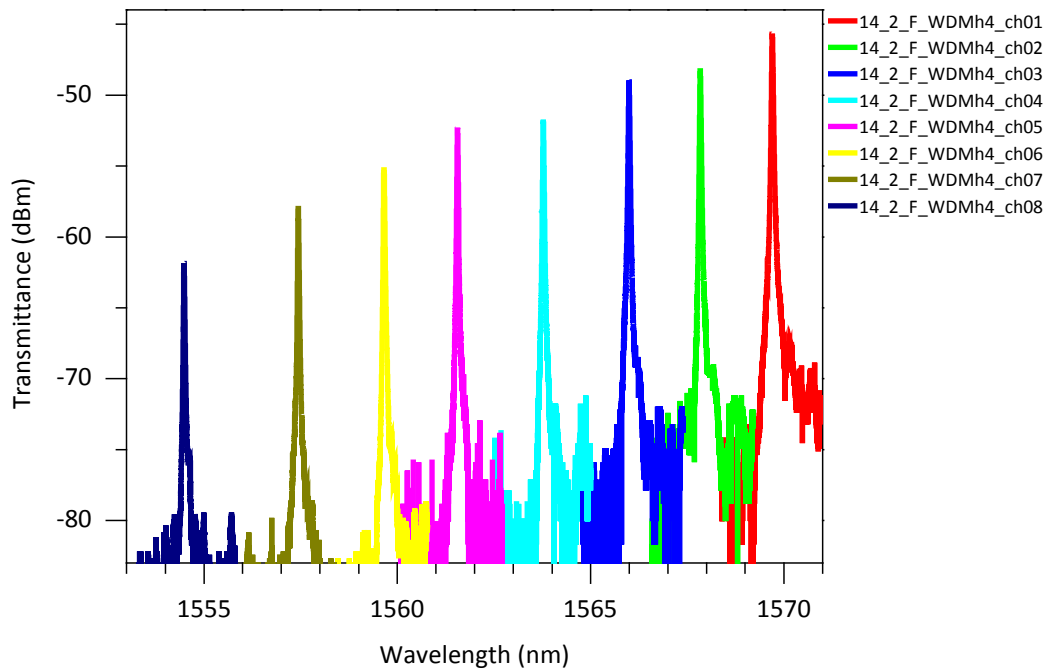


Fig. 5.4. Transmission spectra of an eight-channel DeMUX on a KT-2 chip with channel spacing of 267 GHz. These are measured with input power of  $-20$  dBm [97] [Reprinted with permission from Y. Ooka, T. Tetsumoto, N. A. B. Daud and T. Tanabe, “Ultrasmall in-plane photonic crystal demultiplexers fabricated with photolithography,” *Opt. Express* **25**, 1521–1528 (2017).].

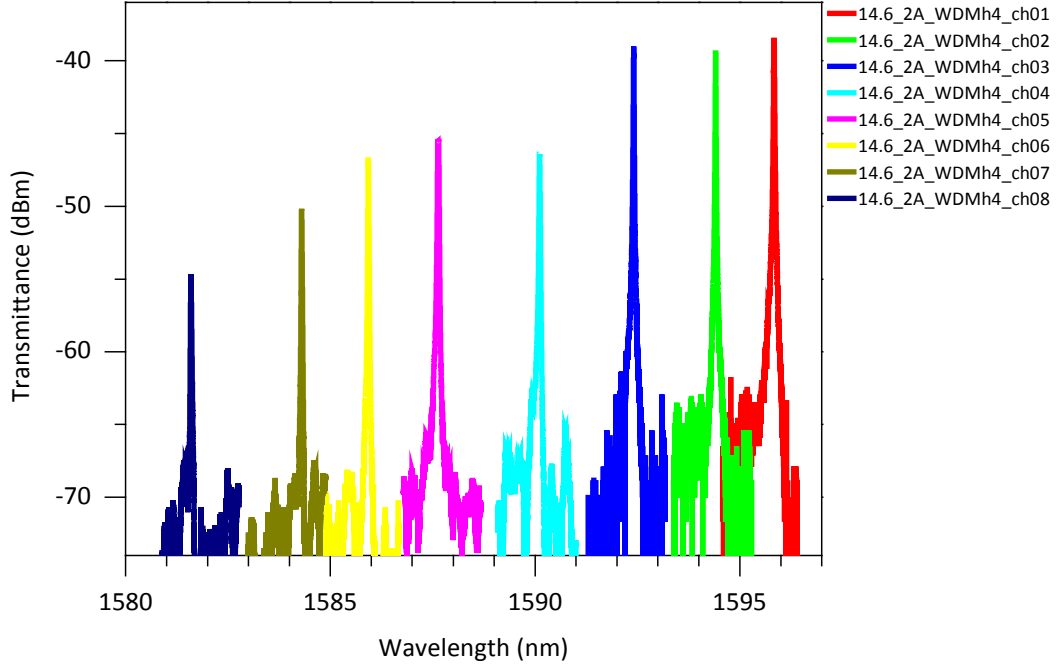


Fig. 5.5. Transmission spectra of an eight-channel DeMUX on a KT-3 chip with channel spacing of 242 GHz. These are measured with input power of  $-10$  dBm.

The average  $Q$  of KT-2 is  $4.6 \times 10^4$ , which means this DeMUX can work at the speed of 4 GHz. Channel 2 in a KT-2 eight-channel DeMUX, for example, has 25.6 dB loss. This loss comes from 1.8 dB at the lens used for coupling to spot size converters (SSCs), 2.8 dB at the SSCs, 0.2 dB at the silicon nanowires, 8.1 dB at the coupling between a WM nanocavity and input/output W1.05 PCWGs, and 12.7 dB at the interfaces between the silicon nanowires and W1.05 PCWGs. From three-dimensional FDTD calculation, intrinsic  $Q$  of channel 1 is calculated as  $6.1 \times 10^4$ , as described in the previous section. Transmittance,  $T$ , of the DeMUX excluding at the interfaces (out of the chip/silicon nanowires/W1.05 PCWG) can be calculated as Eq. (5.1), where  $Q_{int}$  and  $Q_{load}$  are intrinsic  $Q$  and loaded  $Q$ , respectively.

$$T = \left( 1 - 2 \cdot \frac{Q_{load}}{Q_{int}} \right)^2 \quad (5.1)$$

Calculated  $T$  has the similar amount as the coupling loss at into and out of the nanocavity; 8.1 dB.

Figure 5.6 shows the tunability of the KT-2 eight-channel DeMUX. It can be seen that linear tuning is successfully obtained, and that the range of this tuning is larger than the channel spacing.

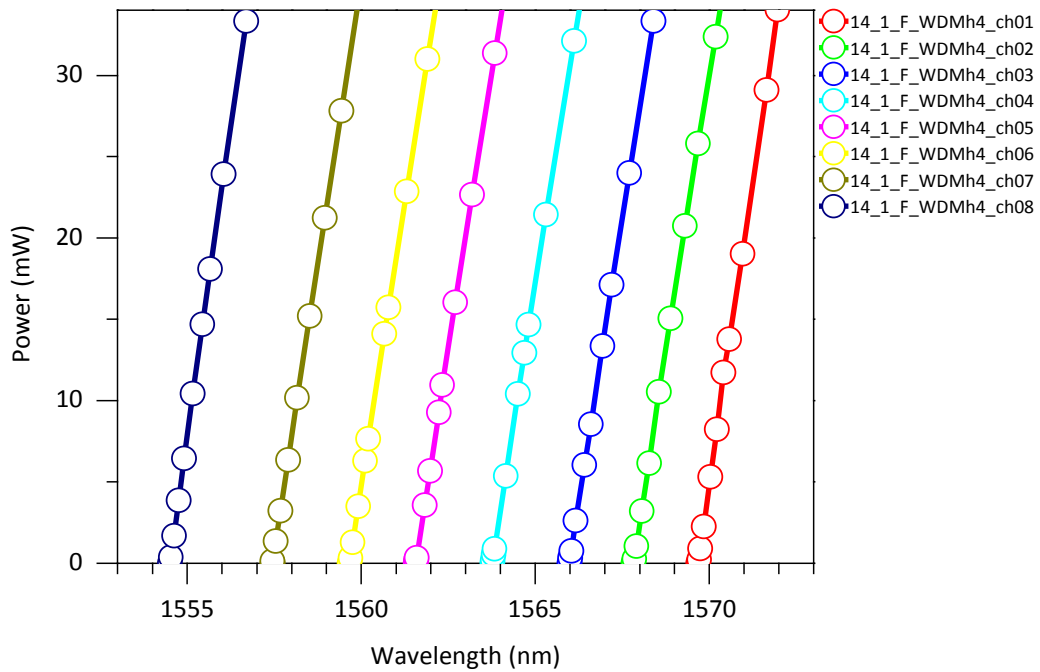


Fig. 5.6. Heater tunability of the eight-channel DeMUX shown in Fig. 5.4. The transmission spectra in Fig. 5.4 is corresponding to 0 mW in this figure [97] [Reprinted with permission from Y. Ooka, T. Tetsumoto, N. A. B. Daud and T. Tanabe, “Ultrasmall in-plane photonic crystal demultiplexers fabricated with photolithography,” *Opt. Express* **25**, 1521–1528 (2017).].

The transmission spectra of our 16-channel DeMUXs on a KT-2 chip and a KT-3 chip are shown in Fig. 5.7 and 5.8, respectively. Since the difference in lattice constants to the next area,  $\Delta a$ , is 0.5 nm in the 16-channel DeMUX whereas eight-channel DeMUXs has  $\Delta a$  of 1.0 nm, the channel spacing of 16-channel is more dense than that of eight-channel. The KT-2 and KT-3 16-channel DeMUX have 136 and 130 GHz, respectively.

It should be noted that the spacing in those two eight- and 16-channel are sufficiently dense to be applied to WDM technology.

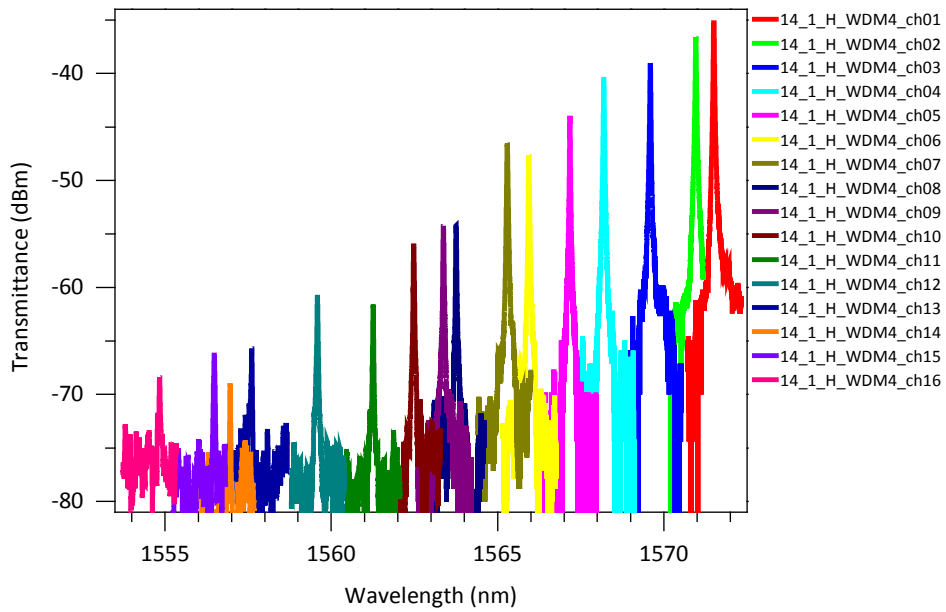


Fig. 5.7. Transmission spectra of a 16-channel DeMUX on a KT-2 chip with channel spacing of 136 GHz. These are measured with input power of  $-20$  dBm [97] [Reprinted with permission from Y. Ooka, T. Tetsumoto, N. A. B. Daud and T. Tanabe, “Ultrasmall in-plane photonic crystal demultiplexers fabricated with photolithography,” *Opt. Express* **25**, 1521–1528 (2017).].

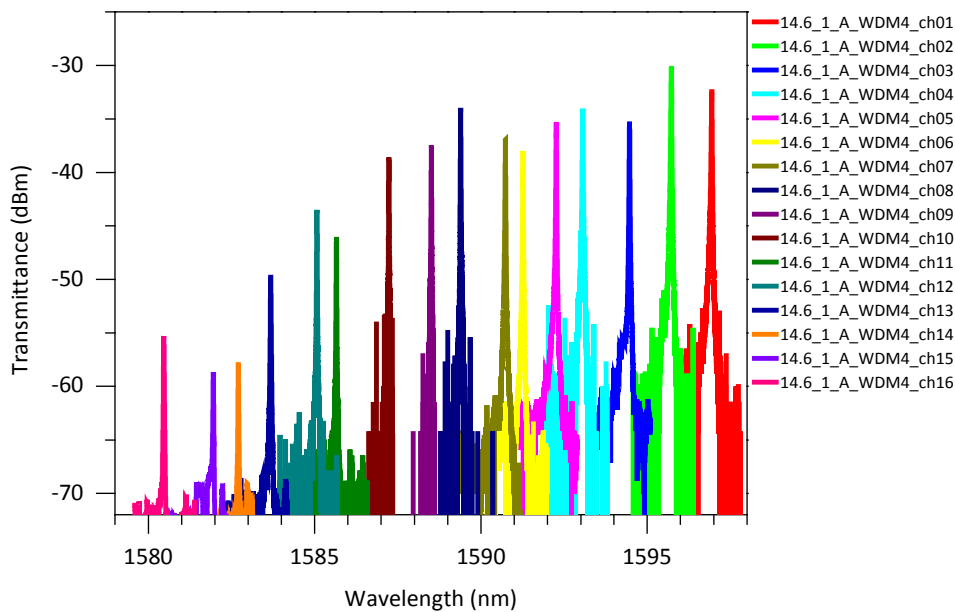


Fig. 5.8. Transmission spectra of a 16-channel DeMUX on a KT-3 chip with channel spacing of 130 GHz. These are measured with input power of

-10 dBm.

### 5.3.3 Eye diagram and crosstalk

The static functions of our DeMUXs have been investigated so far. Here, their dynamic functions are investigated. The setup for this investigation is shown in Fig. 5.9. In the measurement of eye diagrams, input light is created at an electro-optic modulator driven with a non-return-to-zero pseudo-random bit sequence (PRBS) signal of  $2^{10} - 1$ , and then output light from channel 1 is measured with an optical sampling oscilloscope. Results are shown in Fig. 5.10, where 1 Gbps and 2.5 Gbps are chosen as input. The extinction ratio (ER) and signal-to-noise ratio (SNR) at 1 Gbps are 10.7 and 10.3 dB, respectively. The ER and SNR at 2.5 Gbps are 14.1 and 10.9 dB, respectively. The insets show reference eye diagrams when channel 1 of the DeMUX is replaced with an attenuator set to have the same transmittance. It can be confirmed that eyes open clearly and that there is no significant signal distortion, comparing the references and the measured signals.

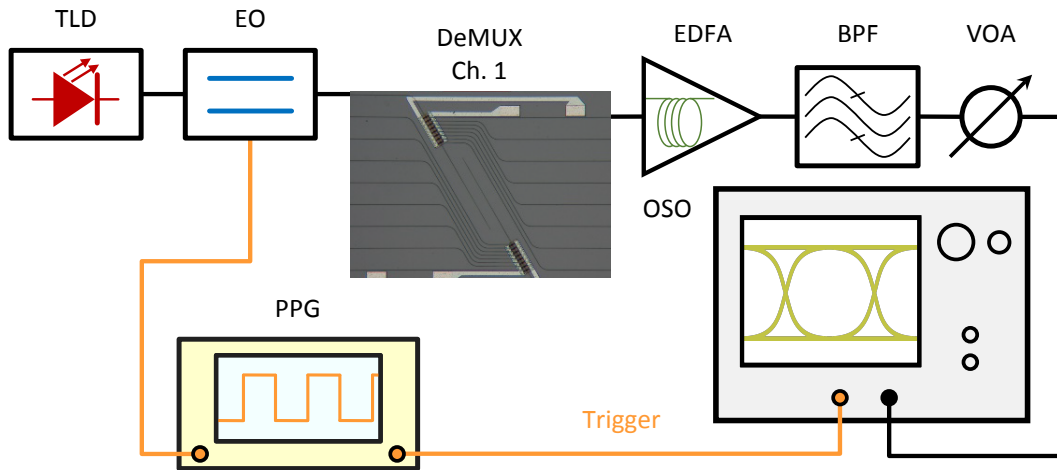


Fig. 5.9. Setup for measuring eye diagrams and crosstalk. TLD: tunable laser diode (Santec TSL-510, linewidth of 200 kHz). EO: electro-optic modulator. EDFA: erbium-doped fiber amplifier. BPF: band-pass filter. VOA: variable optical attenuator. PPG: pulse pattern generator (Keysight 81134A, 3.35-GHz bandwidth). OSO: optical sampling oscilloscope (Agilent 86103A, 2.85-GHz bandwidth) [97] [Reprinted with permission from Y. Ooka, T. Tetsumoto, N. A. B. Daud and T. Tanabe, “Ultrasmall in-plane photonic crystal demultiplexers fabricated with photolithography,” *Opt. Express* **25**, 1521–1528 (2017).].

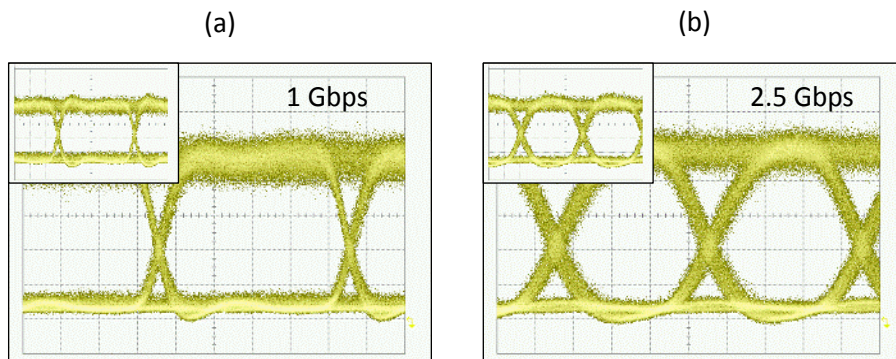


Fig. 5.10. (a), (b) Eye diagrams of the output at channel 1 at 1 Gbps and 2.5 Gbps, respectively, where PRBS of  $2^{10} - 1$  is employed. ER and SNR at 1 Gbps are 10.7 and 10.3 dB, respectively, and those at 2.5 Gbps are 14.1 and 10.9 dB, respectively. Insets are reference eye diagrams when the DeMUX was replaced with another VOA with an attenuation the same as the transmittance of the channel 1 [97] [Reprinted with permission from Y. Ooka, T. Tetsumoto, N. A. B. Daud and T. Tanabe, “Ultrasmall in-plane photonic crystal demultiplexers fabricated with photolithography,” *Opt. Express* **25**, 1521–1528 (2017).].

Crosstalk is measured with the same setup shown in Fig. 5.9, and the result is shown in Fig. 5.11 with one of KT-2 eight-channel DeMUXs. In this measurement, the input PRBS signal is replaced with a square pulse at the speed of 1 GHz. As an input light change its wavelength, it outputs at different channels.

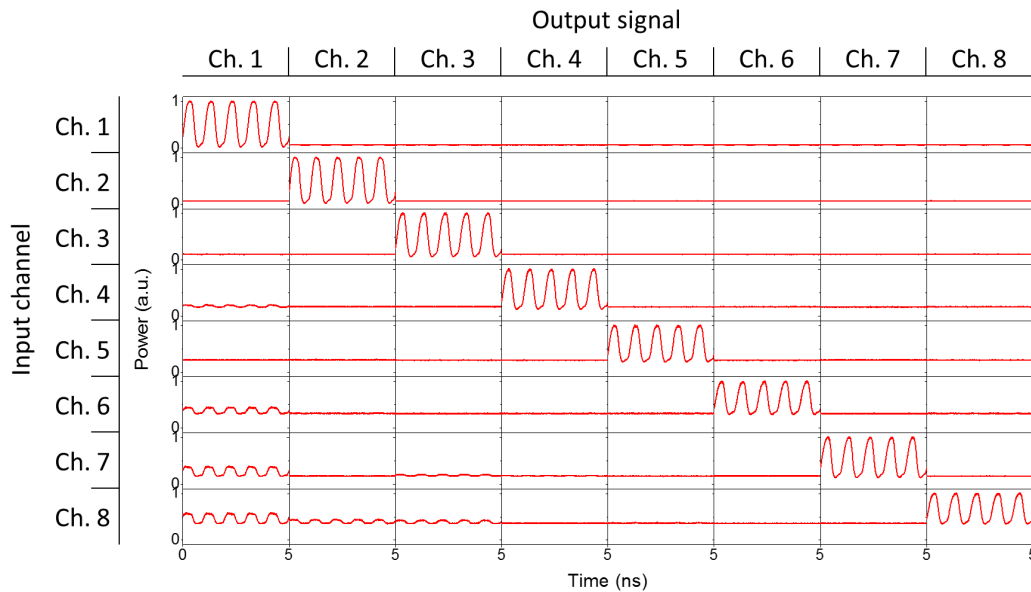


Fig. 5.11. Measured crosstalk with 1-GHz square pulse. Output signals in the same row were measured when the input signal had the same center wavelength. Output signals in the same columns were measured at the same output channels [97] [Reprinted with permission from Y. Ooka, T. Tetsumoto, N. A. B. Daud and T. Tanabe, “Ultrasmall in-plane photonic crystal demultiplexers fabricated with photolithography,” *Opt. Express* **25**, 1521–1528 (2017).].

However, some amount of crosstalk can be observed around the input signal wavelengths set at channels 6, 7 and 8. In the next section, the investigation for crosstalk reduction is conducted with FDTD calculation results.

## 5.4 Optimization of PhC DeMUXs

My optimization process is looking for the structure that reduces crosstalk and keeps high transmittance. Here, four different types of candidates are proposed.

- Barrier : a hole/holes are placed in the W0.98 PCWG
- Stone : a hole/holes are embed on the W0.98 PCWG
- Filter : a PCWG is created on the opposite side against the input W1.05 PCWG
- Couple : position of output W1.05 PCWG is changed

In short, the best candidate for optimization is the “Couple” strategy, but, in the beginning, some results from the other strategies are summarized and then the best strategy “Couple” is discussed.

### 5.4.1 Three failed candidates for optimization

In this section, failed structures for optimization are briefly summarized. Figure 5.12 shows an overlap of transmission spectra of structure with and without “Barrier”. This structure is one of trials, where the position or number of “Barrier” are changed. None of them shows expected optimization.

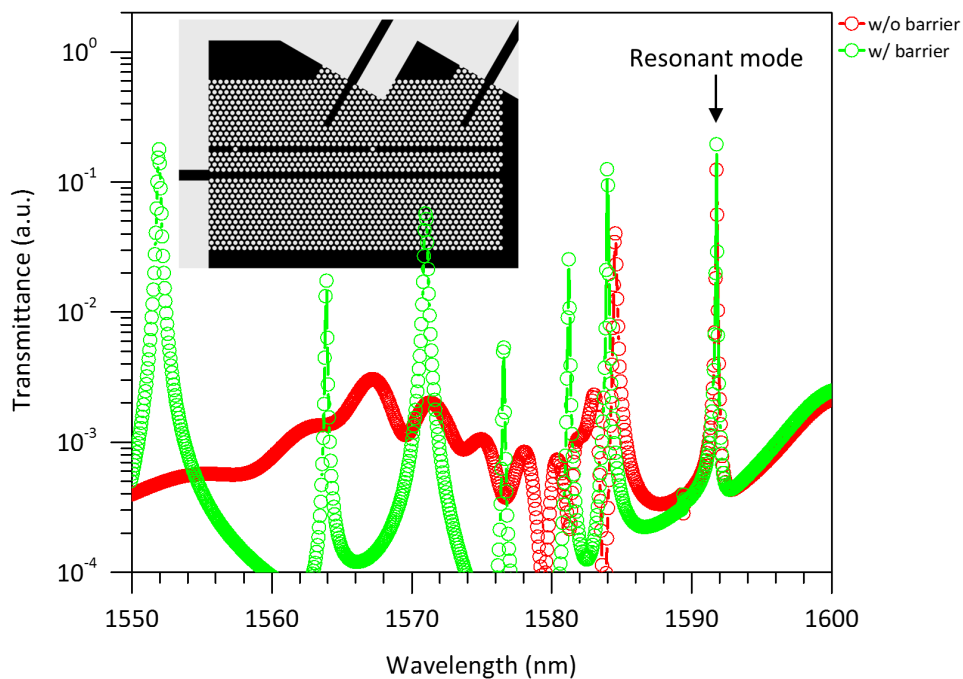


Fig. 5.12. Transmission spectra of failed “Barrier” structure (green) and without “Barrier” structure (red). These structures have only channel 1 and 2. “Barrier” structure shows many peaks assumed to be caused by Fabry-Perot resonances.

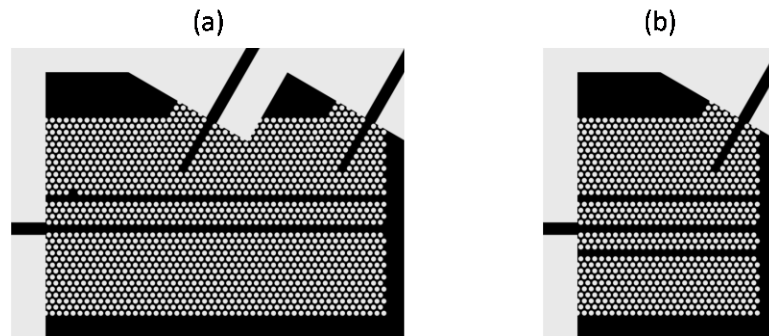


Fig. 5.13. Examples of failed structures. (a) “Stone.” A hole is embedded on the W0.98 PCWG. The position and the number of holes are changed in various patterns. For instance, two holes, right-hand-side of the nanocavity or lower side of W0.98 PCWG are tried. (b) “Filter.” Another PCWG is created on the opposite side against the W1.05 PCWG. The distance from the W1.05 PCWG (how rows the filter PCWG is away from W1.05 PCWG) or the width of the filter PCWG are changed and examined.

Figure 5.13 shows structures of “Stone” and “Filter.” In the trials of “Stone” structure, the position and the number of holes are changed in various patterns. For example, two vertically or horizontally embedded holes, right or left side of the nanocavity or upper or lower side of the W0.98 PCWG are examined. As “Barrier” structure, neither of “Stone” and “Filter” show improvement.

#### 5.4.2 Succeed strategy for optimization

The fact that the peak transmittance drops as the number of channel increases is the main reason why crosstalk happens at channels of larger number. Figure 5.14(a) and 5.14(b) compare the results from experiment and two-dimensional FDTD calculation. The FDTD models the hole diameter of 300 nm to match wavelength range to experimental results, and uses effective refractive index,  $n_{eff}$ , of two-dimensional silicon slab of 2.81. It is proven that this two-dimensional modeling in FDTD calculation reproduces experimental transmission spectra sufficiently.

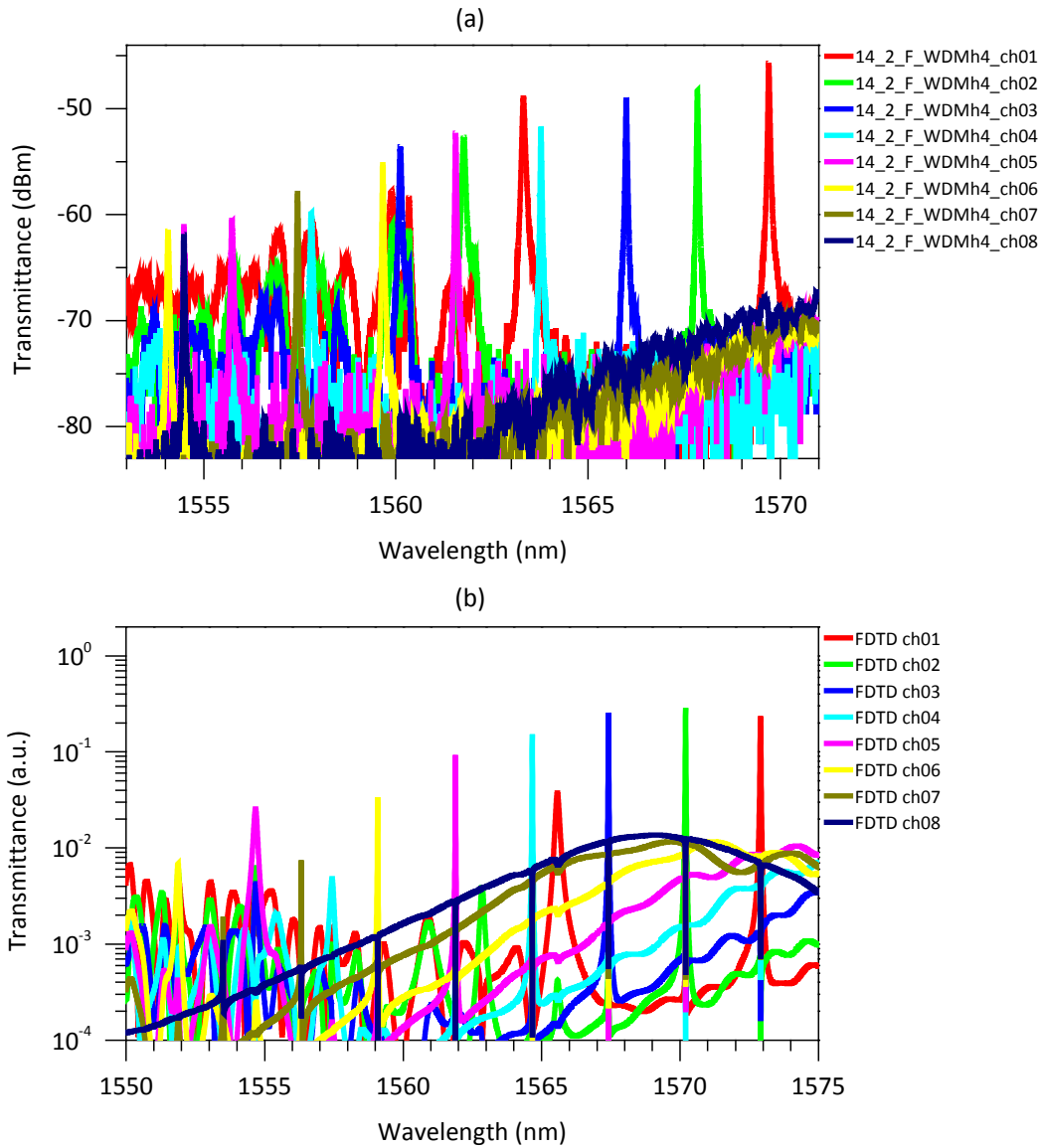


Fig. 5.14. Transmission spectra of eight-channel DeMUXs. (a) One of experimental results that is the same chip as Fig. 5.4. (b) A result from two-dimensional FDTD calculation, where hole diameter is set at 300 nm in order to match wavelength range to experimental results. Effective refractive index,  $n_{eff}$ , of 2.81 is used for silicon slab [97] [Reprinted with permission from Y. Ooka, T. Tetsumoto, N. A. B. Daud and T. Tanabe, “Ultrasmall in-plane photonic crystal demultiplexers fabricated with photolithography,” *Opt. Express* **25**, 1521–1528 (2017).].

The “Couple” strategy finds the best position for output W1.05 PCWGs to reduce crosstalk and obtain high transmittance. Figure 5.15 shows the definition of the positions. The position of the original design is set at (0, 0). Calculation is conducted for (0, -2)-(+5, +3), where some positions are not calculated to save calculation time.

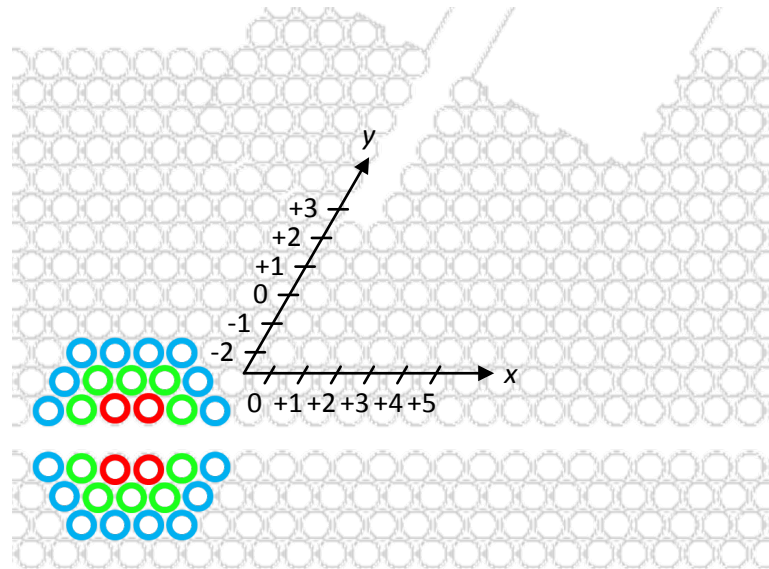


Fig. 5.15. Concept of “Couple” strategy. In this strategy, the position of output W1.05 PCWGs is changed to find the optimized point. The direction of position changing is shown in this figure, (x, y). The fabricated eight-channel DeMUX has (0, 0), and this figure shows (0, +3).

Figure 5.16 shows one of the results of “Couple” strategy is applied to the FDTD calculation, where the amount of position changing is (+3, 0). Comparison between Fig. 5.14(b) and 5.16 shows clearly that crosstalk and transmittance improve. A criteria for crosstalk is set to evaluate it quantitatively as shown in Fig. 5.17. In this criteria, crosstalk is defined as the difference between the peak of a channel and its background close to the channel. Here, the “close” area is set at one channel spacing, as described with broken lines in Fig. 5.17. The reason why one channel spacing is chosen is that the wavelengths of channel peaks fluctuate because of randomness in PhC holes.

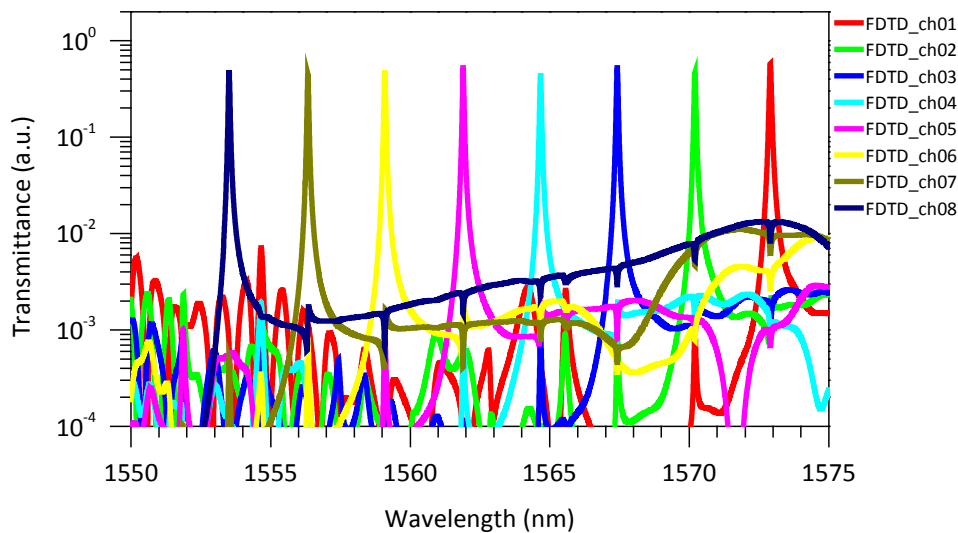


Fig. 5.16. Calculated transmission spectra of an eight-channel DeMUX with position changing of (+3, 0). Parameters are same as Fig. 5.14(b) [97] [Reprinted with permission from Y. Ooka, T. Tetsumoto, N. A. B. Daud and T. Tanabe, “Ultrasmall in-plane photonic crystal demultiplexers fabricated with photolithography,” *Opt. Express* **25**, 1521–1528 (2017).].

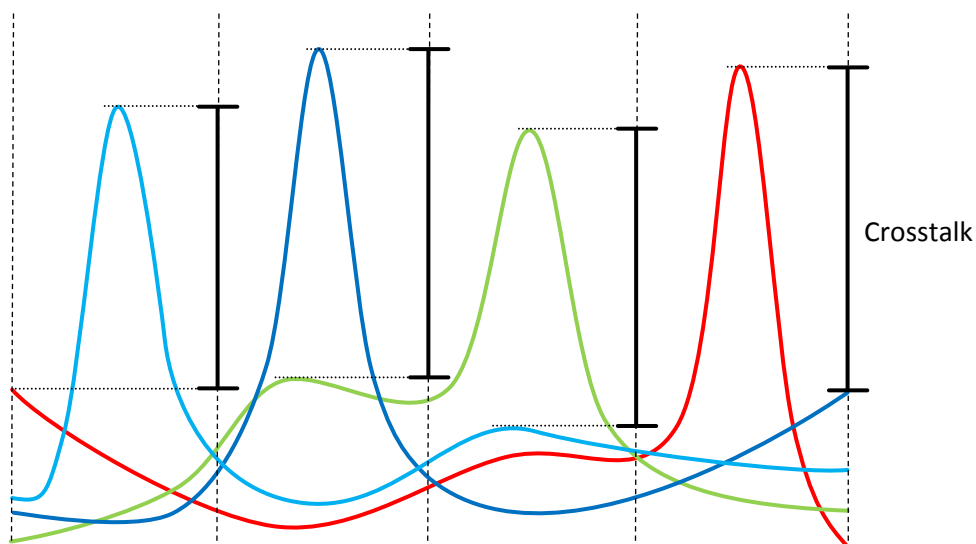


Fig. 5.17. Definition of crosstalk in our optimization process. At the red channel, crosstalk is measured from the difference between the top of the red peak and the blue transmittance. Broken lines represent the channel spacing between channels. For simplicity’s sake, the illustration consists of only four channels.

The “Couple” strategy provides the optimized point to start an output W1.05 PCWG (Fig. 5.18). It shows crosstalk at each point, where displayed crosstalk is defined as the average of crosstalk at eight channels. The best crosstalk position is  $(+3, 0)$ , which has 13 dB or 20 times larger crosstalk than that of the original design at  $(0, 0)$ . Red appearance points (12-20 dB) are placed from  $(-1, 0)$  to  $(+2, +5)$ , which matches the direction of resonant mode. Figure 5.19 shows the summary of optimizing transmittance of eight-channel DeMUXs. The highest transmittance is also obtained at  $(+3, 0)$ . The value of transmittance shown in Fig. 5.19 is the average of eight channels in a structure. Positions for high transmittance place at relevantly lower area  $-2 < y < 0$ . This is because the intensity of resonant modes are strong along a W0.98 PCWG and lower positions are easy to couple the modes.

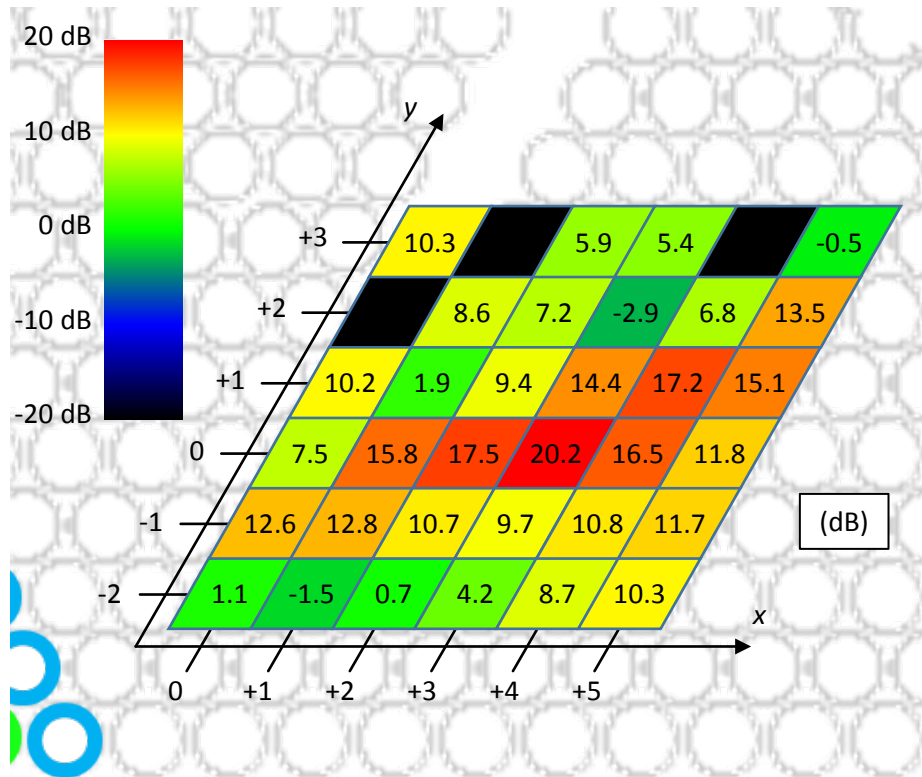


Fig. 5.18. Crosstalk map in the “Couple” strategy. The value of crosstalk is the average of eight channels at each point. At black area,  $(0, +2)$ ,  $(+1, +3)$  and  $(+4, +3)$ , peak transmittance is much lower than transmittance of other channels. The highest crosstalk can be obtained at  $(+3, 0)$ , which is 13 dB or 20 times improved than the original structure,  $(0, 0)$ .

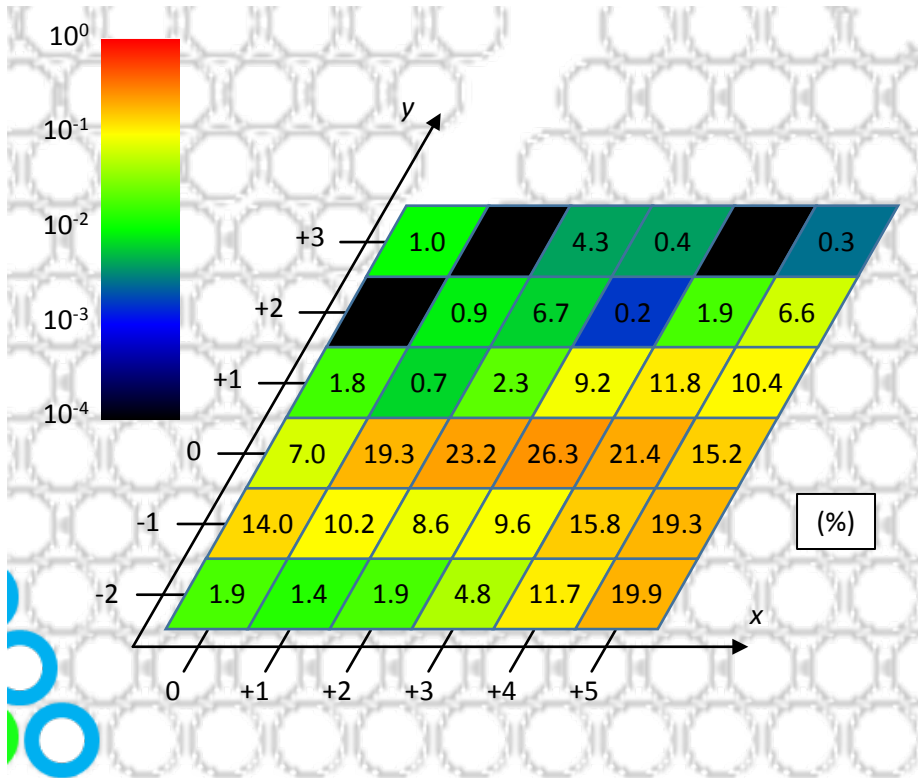


Fig. 5.19. Transmittance map in the “Couple” strategy. The percentage of transmittance is the average of eight channels at each point. At black area, (0, +2), (+1, +3) and (+4, +3), peak transmittance is much lower than transmittance of other channels. The highest transmittance is at (+3, 0), which is 3.3 times improved than the original structure, (0, 0).

There is another discovery that is helpful when large integrated PhC devices. It is revealed that W0.98 PCWGs cause unexpected high transmittance which may lead to crosstalk. Figure 5.19 shows channel 1 of the KT-2 eight-channel DeMUX that has been shown in Fig. 5.4. An unexpected high transmittance is seen at 1563 nm, and this transmittance is the band-edge mode in W0.98 PCWG as shown in Fig. 5.20(a). This high transmittance at 1565 nm is also suppressed by “Couple” strategy. Figure 5.20(b) shows the calculated transmission spectra of (+3, 0) changing. The band-edge mode does not couple to output W1.05 PCWG, because the band-edge mode has destructive direction caused by the interference between the original band-edge mode and a  $\pi/2$ -phase-shift band-edge mode due to the width-modulation at the nanocavity. Insets in Fig. 5.20 show the reduction of the band-edge mode coupling to output W1.05 PCWGs by (+3, 0)

changing.

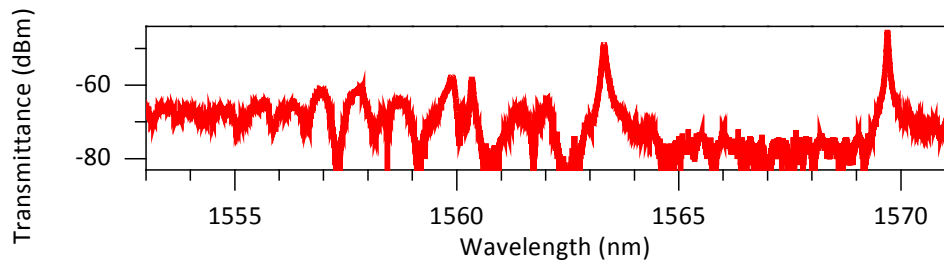


Fig. 5.20. Transmission spectra of channel 1 of the fabricated DeMUX. Same as Fig. 5.4.

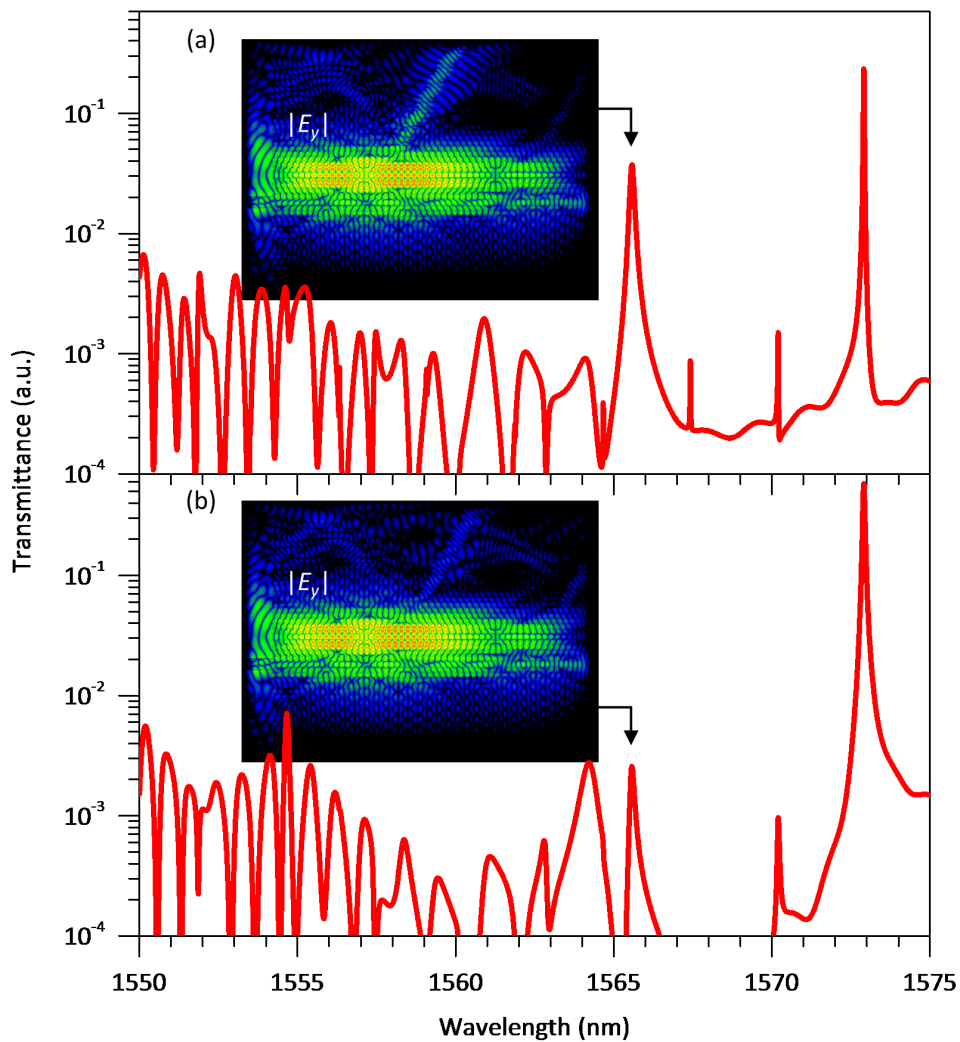


Fig. 5.21. The calculated transmission spectra of channels 1 for (a) (0, 0) and (b) (+3, 0). The inset shows the  $|E_y|$  profile of the band-edge mode, corresponding to the peak indicated with the arrows [97] [Reprinted with

permission from Y. Ooka, T. Tetsumoto, N. A. B. Daud and T. Tanabe, “Ultrasmall in-plane photonic crystal demultiplexers fabricated with photolithography,” Opt. Express **25**, 1521–1528 (2017).].

### 5.4.3 Randomness in PhC DeMUXs

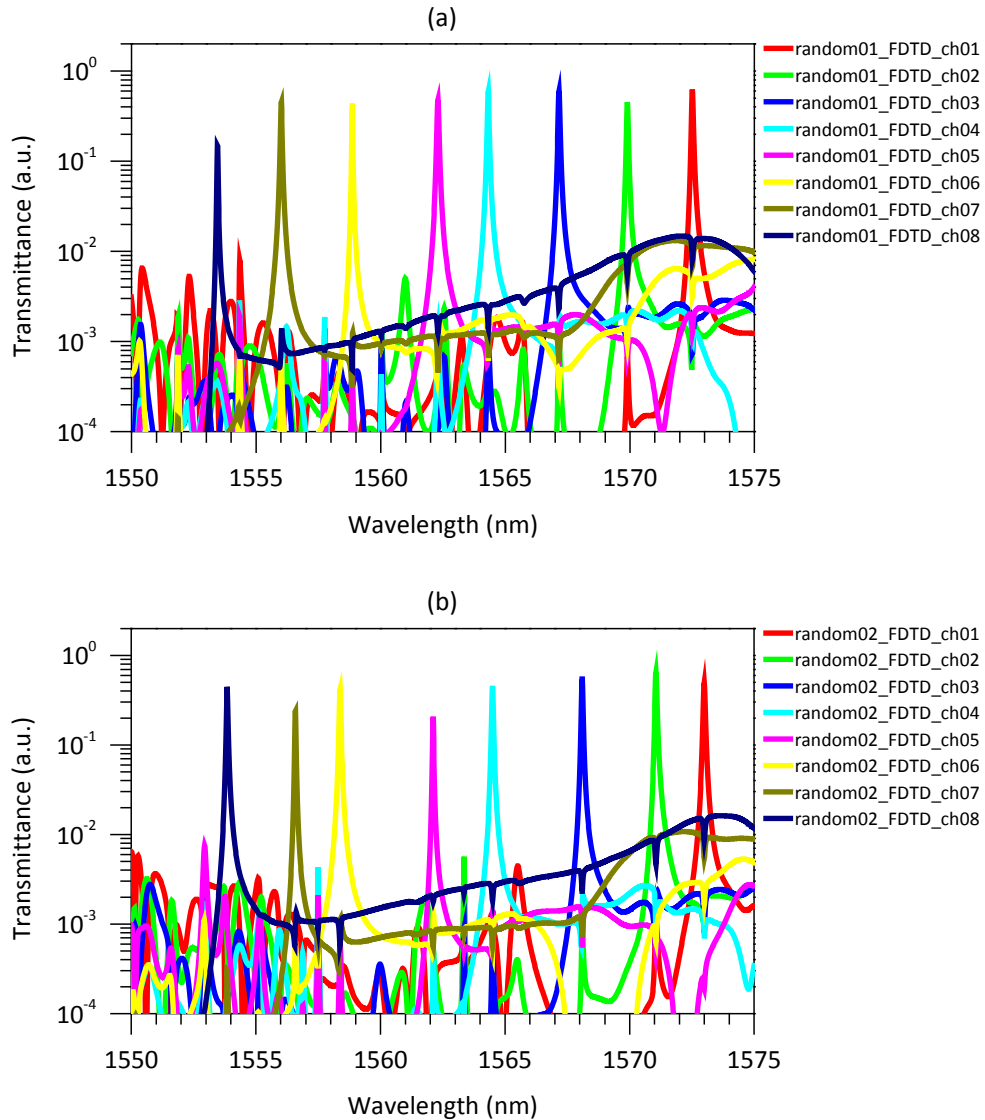


Fig. 5.22. Calculated transmission spectra of eight-channel DeMUXs with deviation of 2 nm in both of hole position and diameter. Random seeds are different in (a) and (b).

Since randomness in PhCs affects their characteristics, effect of randomness on PhC

DeMUX is investigated using two-dimensional FDTD calculation. Figure 5.22 shows results of the calculation where deviation of 2 nm is included in both of hole position and diameter. Each calculation shown in Figs. 5.22(a) and 5.22(b), has different random seeds. It can be seen that transmission wavelengths differ by amount of 50-90 GHz, and that the transmittance of eight channels is not so fluctuated. High transmittance at all channels can be expected even when randomness from photolithography is included in PhC structure.

## 5.4.4 Calculation of large number of channels

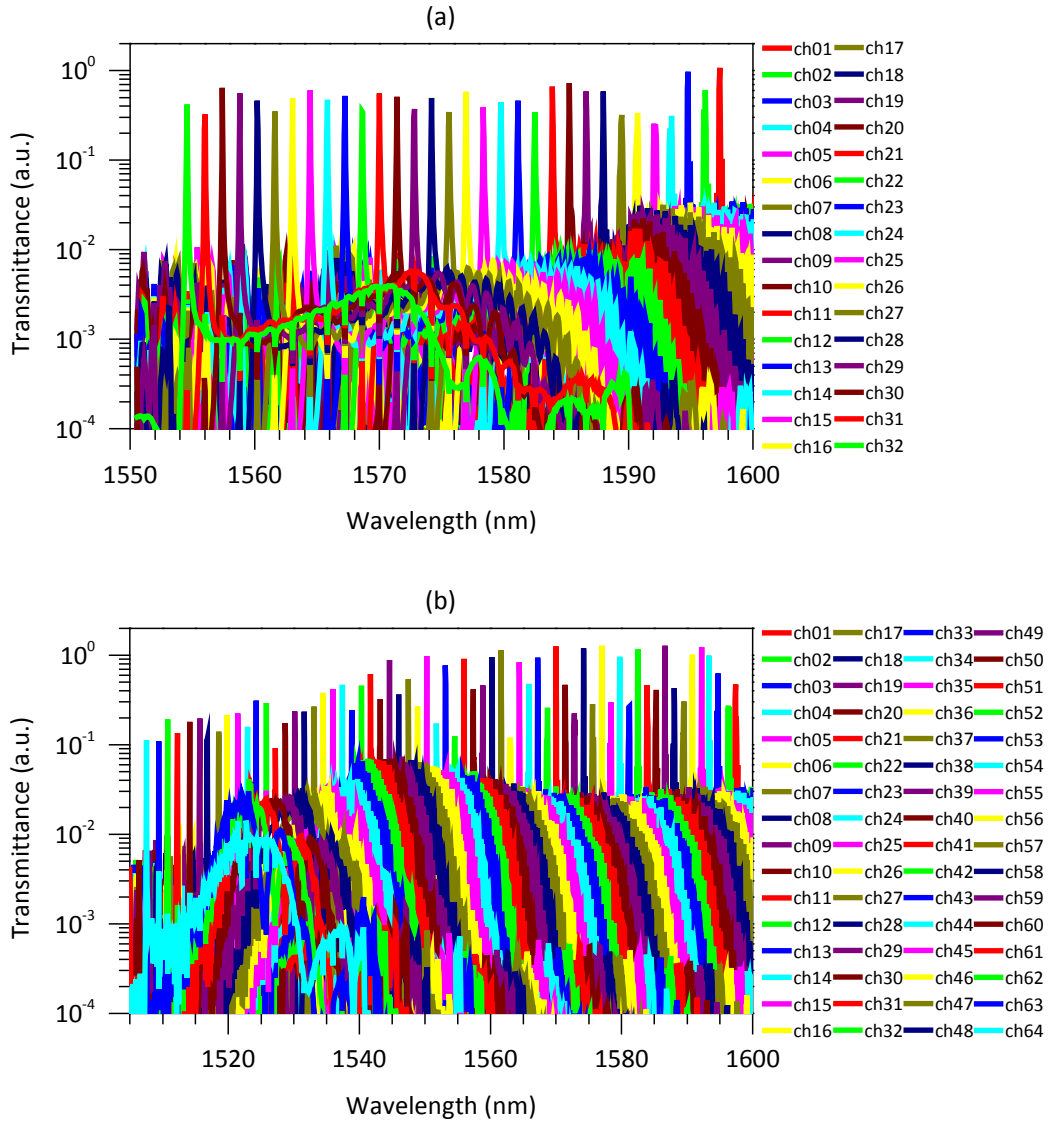


Fig. 5.23. Calculated transmission spectra of a DeMUX with (a) 32 channels and (b) 64 channels, where the hole diameter is 287 nm and  $\Delta a$  is 0.5 nm.

Figure 5.23 shows transmission spectra calculated with two-dimensional FDTD as conducted so far. 32-channel and 64-channel are Figs. 5.23(a) and 5.23(b), respectively. Those results show that our DeMUXs can be applied larger number of channels. The advantage of our DeMUX is its footprint. The 64-channel DeMUX is, for example, only

0.6 mm at its long side.

## 5.5 Summary

The eight- and 16-channel DeMUXs are demonstrated with spacing of 267 and 136 GHz in KT-2 chips and 242 and 130 GHz in KT-3 chips. Those are fabricated with photolithography and clad with silica, which means that those are genuinely compatible with other silicon photonic devices. The PhC DeMUXs are precisely tunable and work at the speed of 2.5 Gbps. Moreover, those have footprint of  $110 \mu\text{m}^2$  per channel, which is tremendously smaller than conventional AWG based DeMUXs. Table 5.1 compares abilities of DeMUXs with this study.

Table 5.1. Comparison to previous works that are one of the best devices in each structure [97] [Reprinted with permission from Y. Ooka, T. Tetsumoto, N. A. B. Daud and T. Tanabe, “Ultrasmall in-plane photonic crystal demultiplexers fabricated with photolithography,” *Opt. Express* **25**, 1521–1528 (2017).].

Stability & Structure	Fabrication method	Capacity	Footprint	Configuration	Reference
High & PhC SiO <sub>2</sub> cladding	Photo-lithography	8 & 16 ch × 267 & 131 GHz	$110 \mu\text{m}^2$	In-plane	This work
Low & PhC air-bridge	EB-lithography	32 ch × 100 GHz	$100 \mu\text{m}^2$	Out-of-plane	[78]
Low & PhC air-bridge	EB-lithography	5 ch × 3.7 THz	$30 \mu\text{m}^2$	In-plane	[75]
High & Silica AWG	Photo-lithography	400 ch × 25 GHz	$20,000,000 \mu\text{m}^2$	In-plane	[63]
High & Silicon AWG	Photo-lithography	8 ch × 250 GHz	$22,000 \mu\text{m}^2$	In-plane	[88]

## Chapter 6

### Summary

I investigated PhCs fabricated with photolithography, and our PhCs are clad with silica. At first, SEM measurement of PhC hole diameter revealed that the three different types of chips have deviation of 3.2-5.8 nm in KT-1 and 1.5-2.2 nm in KT-2 and -3 in its hole diameter. After the fundamental characteristics in photolithography is analyzed, we tackled on randomness in fabricated PhCs. The HW PCWG structures showed their ability to control the position and the possibility of the appearance of light confinement based on randomness. The position of light confinement is only limited in W0.98 PCWGs, and the experiment showed that  $Q$ s of confinement modes exceed  $10^4$  usually and its yield rate is more than 80%. Utilizing this confinement mode, we demonstrated EO modulation at the speed of 1 GHz, where an *p-i-n* junction is integrated with a HW PCWG. Finally, as the combination of what we have been working on, eight- and 16-channel DeMUXs were demonstrated. Those are 267 and 136 GHz on KT-2, and 242 and 130 GHz on KT-3. The biggest advantage of the DeMUXs is the footprint, which is  $110 \mu\text{m}^2$  per channel and highly minimized compared to conventional silica based DeMUXs. In the time domain demonstration, the DeMUXs showed 2.5 Gbps capacity. I believe this thesis summarizes the development of photolithographic PhCs and paves the way to the future practical integrated PhC application.

# Bibliography

1. E. Yablonovitch, "Inhibited spontaneous emission in solid-state physics and electronics," *Phys. Rev. Lett.* **58**, 2059–2062 (1987).
2. S. John, "Strong Localization of Phonons in Certain Disordered Dielectric Superlattices," *Phys. Rev. Lett.* **58**, 2486–2489 (1987).
3. S. John, "Why trap light?," *Nat. Mater.* **11**, 997–999 (2012).
4. E. Yablonovitch, "In the limelight," *Nat. Mater.* **11**, 1000–1001 (2012).
5. D. Y. Chu and S. T. Ho, "Dielectric photonic well and wire and 1-D photonic bandgap structure in photonic wire," in *Optical Soc. Amer. Annu. Meet. Tech. Dig., San Jose, CA* (1991), p. MTS.
6. B. Meade and J. D. Joannopoulos, "Cavities in photonic bandgap material for laser applications," in *Optical Soc. Amer. Annu. Meet. Tech. Dig., San Jose, CA* (1991), p. MTI.
7. P. R. Villeneuve, S. Fan, J. D. Joannopoulos, K. Y. Lim, G. S. Petrich, L. A. Kolodziejski, and R. Reif, "Air-bridge microcavities," *Appl. Phys. Lett.* **67**, 167 (1995).
8. J. S. Foresi, P. R. Villeneuve, J. Ferrera, E. R. Thoen, G. Steinmeyer, S. Fan, J. D. Joannopoulos, L. C. Kimerling, H. I. Smith, and E. P. Ippen, "Photonic-bandgap microcavities in optical waveguides," *Nature* **390**, 143–145 (1997).
9. C. Sauvan, G. Lecamp, P. Lalanne, and J. P. Hugonin, "Modal-reflectivity enhancement by geometry tuning in Photonic Crystal microcavities," *Opt. Express* **13**, 245–255 (2005).
10. A. R. Zain, N. P. Johnson, M. Sorel, and R. M. De La Rue, "Ultra high quality factor one dimensional photonic crystal/photonic wire micro-cavities in silicon-on-insulator (SOI)," *Opt. Express* **16**, 12084–12089 (2008).
11. P. B. Deotare, M. W. McCutcheon, I. W. Frank, M. Khan, and M. Lončar, "High

- quality factor photonic crystal nanobeam cavities," *Appl. Phys. Lett.* **94**, 121106 (2009).
12. Q. Quan and M. Loncar, "Deterministic design of wavelength scale, ultra-high Q photonic crystal nanobeam cavities," *Opt. Express* **19**, 18529–18542 (2011).
  13. Y. Tanaka, T. Asano, and S. Noda, "Design of Photonic Crystal Nanocavity with Q-factor of  $\sim 10^9$ ," *J. Light. Technol.* **26**, 1532–1539 (2008).
  14. J. Chan, T. P. M. Alegre, A. H. Safavi-Naeini, J. T. Hill, A. Krause, S. Groblacher, M. Aspelmeyer, and O. Painter, "Laser cooling of a nanomechanical oscillator into its quantum ground state," *Nature* **478**, 18 (2011).
  15. P. B. Deotare, I. Bulu, I. W. Frank, Q. Quan, Y. Zhang, R. Ilic, and M. Loncar, "All optical reconfiguration of optomechanical filters," *Nat. Commun.* **3**, 846 (2012).
  16. F. Tian, H. Sumikura, E. Kuramochi, H. Taniyama, M. Takiguchi, and M. Notomi, "Optomechanical oscillator pumped and probed by optically two isolated photonic crystal cavity systems," *Opt. Express* **24**, 28039 (2016).
  17. M. Plihal and A. Shambrook, "Two-dimensional photonic band structures," *Opt. Commun.* **80**, 199–204 (1991).
  18. M. Plihal and A. A. Maradudin, "Photonic band structure of two-dimensional systems: The triangular lattice," *Phys. Rev. B* **44**, 8565–8571 (1991).
  19. S. L. McCall, P. M. Platzman, R. Dalichaouch, D. Smith, and S. Schultz, "Microwave propagation in two-dimensional dielectric lattices," *Phys. Rev. Lett.* **67**, 2017–2020 (1991).
  20. R. D. Meade, K. D. Brommer, A. M. Rappe, and J. D. Joannopoulos, "Existence of a photonic band gap in two dimensions," *Appl. Phys. Lett.* **61**, 495–497 (1992).
  21. J. D. Joannopoulos, *Photonic Crystals—molding the Flow of Light* (Princeton University Press, 1995).
  22. T. Krauss, Y. P. Song, S. Thorns, and R. M. Delarue, "Fabrication of 2-D photonic bandgap structures in GaAs/AlGaAs," *Electron. Lett.* **30**, 1444–1446 (1994).
  23. J. M. GERARD, A. IZRAË, J. Y. MARZIN, R. PADJEN, and F. R. LADAN, "PHOTONIC BANDGAP OF TWO-DIMENSIONAL DIELECTRIC CRYSTALS," *Solid. State. Electron.* **37**, 1341–1344 (1994).

24. O. Painter, A. Scherer, O. Painter, J. Vučković, A. Scherer, and J. Vuc, "Defect modes of a two-dimensional photonic crystal in an optically thin dielectric slab," *Opt. Soc. Am. B* **16**, 275–285 (1999).
25. E. Yablonovitch, T. J. Gmitter, R. D. Meade, A. M. Rappe, K. D. Brommer, and J. D. Joannopoulos, "Donor and acceptor modes in photonic band structure," *Phys. Rev. Lett.* **67**, 3380–3383 (1991).
26. O. Painter, R. K. Lee, A. Scherer, A. Yariv, J. D. O'Brien, P. D. Dapkus, and I. Kim, "Two-Dimensional Photonic Band-Gap Defect Mode Laser," *Science* **284**, 1819–1821 (1999).
27. M. Notomi, K. Yamada, a. Shinya, J. Takahashi, C. Takahashi, and I. Yokohama, "Extremely Large Group-Velocity Dispersion of Line-Defect Waveguides in Photonic Crystal Slabs," *Phys. Rev. Lett.* **87**, 253902 (2001).
28. W. Bogaerts, V. Wiaux, D. Taillaert, S. Beckx, B. Luysaert, P. Bienstman, and R. Baets, "Fabrication of Photonic Crystals in Silicon-on- Insulator Using 248-nm Deep UV Lithography," *IEEE J. Sel. Top. Quantum Electron.* **8**, 928–934 (2002).
29. Y. Akahane, T. Asano, B. Song, and S. Noda, "High-Q photonic nanocavity in a two-dimensional photonic crystal," *Nature* **425**, 944–947 (2003).
30. Y. Akahane, M. Mochizuki, T. Asano, Y. Tanaka, and S. Noda, "Design of a channel drop filter by using a donor-type cavity with high-quality factor in a two-dimensional photonic crystal slab," *Appl. Phys. Lett.* **82**, 1341–1343 (2003).
31. T. Tanabe, M. Notomi, S. Mitsugi, A. Shinya, and E. Kuramochi, "All-optical switches on a silicon chip realized using photonic crystal nanocavities," *Appl. Phys. Lett.* **87**, 151112 (2005).
32. V. R. Almeida, C. A. Barrios, R. R. Panepucci, and M. Lipson, "All-optical control of light on a silicon chip," *Nature* **431**, 1081–1084 (2004).
33. B.-S. Song, S. Noda, T. Asano, and Y. Akahane, "Ultra-high-Q photonic double-heterostructure nanocavity," *Nat. Mater.* **4**, 207–210 (2005).
34. E. Kuramochi, M. Notomi, S. Mitsugi, A. Shinya, T. Tanabe, and T. Watanabe, "Ultrahigh-Q photonic crystal nanocavities realized by the local width modulation of a line defect," *Appl. Phys. Lett.* **88**, 41112 (2006).
35. Y. Ooka, T. Tetsumoto, A. Fushimi, W. Yoshiki, and T. Tanabe, "CMOS

- compatible high-Q photonic crystal nanocavity fabricated with photolithography on silicon photonic platform," *Sci. Rep.* **5**, 11312 (2015).
36. K. Nozaki, T. Tanabe, A. Shinya, S. Matsuo, T. Sato, H. Taniyama, and M. Notomi, "Sub-femtojoule all-optical switching using a photonic-crystal nanocavity," *Nat. Photonics* **4**, 477–483 (2010).
  37. Y. Takahashi, Y. Inui, M. Chihara, T. Asano, R. Terawaki, and S. Noda, "A micrometre-scale Raman silicon laser with a microwatt threshold," *Nature* **498**, 470–474 (2013).
  38. J. M. Frigerio, J. Rivory, and P. Sheng, "Photonic bandtail in 1D randomly-perturbed periodic systems," *Opt. Commun.* **98**, 231–235 (1993).
  39. D. Wiersma and a Lagendijk, "Light diffusion with gain and random lasers," *Phys. Rev. E Stat. Phys. Plasmas Fluids Relat. Interdiscip. Top.* **54**, 4256–4265 (1996).
  40. Y. A. Vlasov, M. A. Kaliteevski, and V. V Nikolaev, "Different regimes of light localization in a disordered photonic crystal," *Phys. Rev. B* **60**, 1555–1562 (1999).
  41. S. Hughes, L. Ramunno, J. F. Young, and J. E. Sipe, "Extrinsic optical scattering loss in photonic crystal waveguides: Role of fabrication disorder and photon group velocity," *Phys. Rev. Lett.* **94**, 33903 (2005).
  42. J. Topolancik, B. Ilic, and F. Vollmer, "Experimental Observation of Strong Photon Localization in Disordered Photonic Crystal Waveguides," *Phys. Rev. Lett.* **99**, 253901 (2007).
  43. P. W. Anderson, "Absence of diffusion in certain random lattices," *Phys. Rev.* **109**, 1492–1505 (1958).
  44. J. Topolancik, F. Vollmer, and B. Ilic, "Random high-Q cavities in disordered photonic crystal waveguides," *Appl. Phys. Lett.* **91**, 201102 (2007).
  45. A. Parini, P. Hamel, A. De Rossi, S. Combrié, N.-V.-Q. Tran, Y. Gottesman, R. Gabet, A. Talneau, Y. Jaouën, and G. Vadalà, "Time-wavelength reflectance maps of photonic crystal waveguides: A new view on disorder-induced scattering," *J. Light. Technol.* **26**, 3794–3802 (2008).
  46. M. Patterson, S. Hughes, S. Combrié, N.-V.-Q. Tran, A. De Rossi, R. Gabet, and Y. Jaouën, "Disorder-Induced Coherent Scattering in Slow-Light Photonic Crystal Waveguides," *Phys. Rev. Lett.* **102**, 253903 (2009).

47. S. Mazoyer, J. P. Hugonin, and P. Lalanne, "Disorder-induced multiple scattering in photonic-crystal waveguides," *Phys. Rev. Lett.* **103**, 63903 (2009).
48. M. Patterson, S. Hughes, S. Schulz, D. M. Beggs, T. P. White, L. O'Faolain, and T. F. Krauss, "Disorder-induced incoherent scattering losses in photonic crystal waveguides: Bloch mode reshaping, multiple scattering, and breakdown of the Beer-Lambert law," *Phys. Rev. B* **80**, 195305 (2009).
49. M. Patterson and S. Hughes, "Theory of disorder-induced coherent scattering and light localization in slow-light photonic crystal waveguides," *J. Opt.* **12**, 104013 (2010).
50. N. Le Thomas, H. Zhang, J. Jágerská, V. Zabelin, R. Houdré, I. Sagnes, and A. Talneau, "Light transport regimes in slow light photonic crystal waveguides," *Phys. Rev. B* **80**, 125332 (2009).
51. S. Mazoyer, P. Lalanne, J. C. Rodier, J. P. Hugonin, M. Spasenović, L. Kuipers, D. M. Beggs, and T. F. Krauss, "Statistical fluctuations of transmission in slow light photonic-crystal waveguides.," *Opt. Express* **18**, 14654–14663 (2010).
52. L. Sapienza, H. Thyrrstrup, S. Stobbe, P. D. Garcia, S. Smolka, and P. Lodahl, "Cavity quantum electrodynamics with Anderson-localized modes.," *Science* **327**, 1352–1355 (2010).
53. J. Liu, P. D. Garcia, S. Ek, N. Gregersen, T. Suhr, M. Schubert, J. Mørk, S. Stobbe, and P. Lodahl, "Random nanolasing in the Anderson localized regime," *Nat. Nanotechnol.* **9**, 285–289 (2014).
54. T. S. Kinsel and R. T. Denton, "Terminals for a High-speed Optical Pulse Code Modulation Communication System: II. Optical Multiplexing and Demultiplexing," *Proc. IEEE* **56**, 146–154 (1967).
55. C. Dragone, C. A. Edwards, and R. C. Kistler, "Integrated Optics N×N Multiplexer on Silicon," *IEEE Photonics Technol. Lett.* **3**, 896–899 (1991).
56. H. Takahashi, Y. Hibino, and I. Nishi, "Polarization-insensitive arrayed-waveguide grating wavelength multiplexer on silicon.," *Opt. Lett.* **17**, 499–501 (1992).
57. Y. Hida, Y. Hibino, M. Itho, A. Sugita, A. Himeno, and Y. Ohmori, "Fabrication of low-loss and polarisation-insensitive 256 channel arrayed-waveguide grating

- with 25 GHz spacing using  $1.5\% \Delta$  waveguides," *Electron. Lett.* **36**, 820–821 (2000).
58. Y. Hida, Y. Hibino, T. Kitoh, Y. Inoue, M. Itoh, T. Shibata, A. Sugita, and A. Himeno, "400-channel 25-GHz spacing arrayed-waveguide grating covering a full range of C- and L-bands," in *OSA Trends in Optics and Photonics (TOPS) Vol. 54, Optical Fiber Communication Conference, Technical Digest, Postconference Edition (Optical Society of America, Washington, DC, 2001)*, 3 (2001), p. WB2-1-WB2-3.
  59. S. Kamei, M. Ishii, A. Kaneko, T. Shibata, and M. Itoh, "N x N cyclic-frequency router with improved performance based on arrayed-waveguide grating," *J. Light. Technol.* **27**, 4097–4104 (2009).
  60. T. Fukazawa, F. Ohno, and T. Baba, "Very compact arrayed-waveguide-grating demultiplexer using Si photonic wire waveguides," *Jpn. J. Appl. Phys.* **43**, 673–675 (2004).
  61. Q. Fang, F. Li, and Y. Liu, "Compact SOI arrayed waveguide grating demultiplexer with broad spectral response," *Opt. Commun.* **258**, 155–158 (2006).
  62. Q. Fang, T.-Y. Liow, J. F. Song, K. W. Ang, M. Bin Yu, G. Q. Lo, and D.-L. Kwong, "WDM multi-channel silicon photonic receiver with 320 Gbps data transmission capability," *Opt. Express* **18**, 5106–5113 (2010).
  63. S. Cheung, T. Su, K. Okamoto, and S. J. B. Yoo, "Ultra-Compact Silicon Photonic  $512 \times 512$  25 GHz Arrayed Waveguide Grating Router," *IEEE J. Sel. Top. Quantum Electron.* **20**, 8202207 (2014).
  64. S. Fan, P. R. Villeneuve, J. D. Joannopoulos, and H. A. Haus, "Channel drop filters in photonic crystals," *Opt. Express* **3**, 4–11 (1998).
  65. C. Manolatou, M. J. Khan, S. Fan, P. R. Villeneuve, H. A. Haus, and J. D. Joannopoulos, "Coupling of Modes Analysis of Resonant Channel Add-----Drop Filters," *IEEE J. Quantum Electron.* **35**, 1322–1331 (1999).
  66. S. Noda, A. Chutinan, and M. Imada, "Trapping and emission of photons by a single defect in a photonic bandgap structure," *Nature* **407**, 608–610 (2000).
  67. A. Chutinan, M. Mochizuki, M. Imada, and S. Noda, "Surface-emitting channel drop filters using single defects in two-dimensional photonic crystal slabs," *Appl.*

- Phys. Lett. **79**, 26902692 (2001).
68. Y. Akahane, T. Asano, B. S. Song, and S. Noda, "Investigation of high-Q channel drop filters using donor-type defects in two-dimensional photonic crystal slabs," *Appl. Phys. Lett.* **83**, 1512–1514 (2003).
  69. B.-S. Song, S. Noda, and T. Asano, "Photonic devices based on in-plane hetero photonic crystals," *Science* **300**, 1537 (2003).
  70. H. Takano, Y. Akahane, T. Asano, and S. Noda, "In-plane-type channel drop filter in a two-dimensional photonic crystal slab," *Appl. Phys. Lett.* **84**, 2226 (2004).
  71. Y. Akahane, T. Asano, H. Takano, B.-S. Song, Y. Takana, and S. Noda, "Two-dimensional photonic-crystal-slab channel drop filter with flat-top response," *Opt. Express* **13**, 2512–2530 (2005).
  72. A. Shinya, S. Mitsugi, E. Kuramochi, and M. Notomi, "Ultrasmall multi-channel resonant-tunneling filter using gap of width-tuned photonic-crystal waveguide," *Opt. Express* **13**, 4202–4209 (2005).
  73. A. Shinya, S. Mitsugi, E. Kuramochi, T. Tanabe, G. Kim, G. Kira, S. Kondo, K. Yamada, T. Watanabe, T. Tsuchizawa, and M. Notomi, "Ultrasmall resonant tunneling/dropping devices in 2D photonic crystal slabs," *Optoelectron. Integr. Devices VII* **5729**, 72–85 (2005).
  74. H. Takano, B.-S. Song, T. Asano, and S. Noda, "Highly efficient multi-channel drop filter in a two-dimensional hetero photonic crystal," *Opt. Express* **14**, 3491–3496 (2006).
  75. A. Shinya, S. Mitsugi, E. Kuramochi, and M. Notomi, "Ultrasmall multi-port channel drop filter in two-dimensional photonic crystal on silicon-on-insulator substrate," *Opt. Express* **14**, 12394–12400 (2006).
  76. B. S. Song, T. Nagashima, T. Asano, and S. Noda, "Resonant-wavelength control of nanocavities by nanometer-scaled adjustment of two-dimensional photonic crystal slab structures," *IEEE Photonics Technol. Lett.* **20**, 532–534 (2008).
  77. X. Gan, N. Pervez, I. Kyriassis, F. Hatami, and D. Englund, "A high-resolution spectrometer based on a compact planar two dimensional photonic crystal cavity array," *Appl. Phys. Lett.* **100**, (2012).
  78. Y. Takahashi, T. Asano, D. Yamashita, and S. Noda, "Ultra-compact 32-channel

- drop filter with 100 GHz spacing," *Opt. Express* **22**, 4692–4698 (2014).
79. F. Meng, R. J. Shiue, N. Wan, L. Li, J. Nie, N. C. Harris, E. H. Chen, T. Schröder, N. Pervez, I. Kyriassis, and D. Englund, "Waveguide-integrated photonic crystal spectrometer with camera readout," *Appl. Phys. Lett.* **105**, 51103 (2014).
80. H. Rong, A. Liu, R. Jones, O. Cohen, and D. Hak, "An all-silicon Raman laser," *Nature* **433**, 292–294 (2005).
81. B. J. Offrein, C. Berger, R. Beyeler, R. Dangel, L. Dellmann, F. Horst, T. Lamprecht, N. Meier, R. Budd, F. Libsch, and J. Kash, "Parallel optical interconnects in printed circuit boards," in *Proceedings of SPIE* (2005), Vol. 5990, p. 59900E–9.
82. P. Dumon, W. Bogaerts, D. Van Thourhout, D. Taillaert, R. Baets, J. Wouters, S. Beckx, and P. Jaenen, "Compact wavelength router based on a Silicon-on-insulator arrayed waveguide grating pigtailed to a fiber array," *Opt. Express* **14**, 664–669 (2006).
83. W. Bogaerts, P. Dumon, D. Van Thourhout, D. Taillaert, P. Jaenen, J. Wouters, S. Beckx, V. Wiaux, and R. G. Baets, "Compact wavelength-selective functions in silicon-on-insulator photonic wires," *IEEE J. Sel. Top. Quantum Electron.* **12**, 1394–1401 (2006).
84. H. Rong, S. Xu, Y.-H. Kuo, V. Sih, O. Cohen, O. Raday, and M. Paniccia, "Low-threshold continuous-wave Raman silicon laser," *Nat. Photonics* **1**, 232–237 (2007).
85. K. Maru, Y. Abe, and H. Uetsuka, "Demonstration of Compact and Low-Loss Athermal Arrayed-Waveguide Grating Module Based on 2.5%- $\Delta$  Silica-Based Waveguides," *Jpn. J. Appl. Phys.* **47**, 7903–7908 (2008).
86. Y. Chetrit, J. Basak, H. Nguyen, D. Rubin, and M. Paniccia, "Wavelength division multiplexing based photonic Integrated circuits on silicon-on-insulator platform," *IEEE J. Sel. Top. Quantum Electron.* **16**, 23–32 (2010).
87. I. M. Soganci, A. La Porta, and B. J. Offrein, "Flip-chip optical couplers with scalable I/O count for silicon photonics," *Opt. Express* **21**, 16075 (2013).
88. S. Pathak, D. Van Thourhout, and W. Bogaerts, "Design trade-offs for silicon-on-insulator-based AWGs for (de)multiplexer applications," *Opt. Lett.* **38**, 2961–2964

- (2013).
89. R. Dangel, F. Horst, and D. Jubin, "Development of versatile polymer waveguide flex technology for use in optical interconnects," *J. Light. Technol.* **31**, 3915–3926 (2013).
  90. K. K. Mehta, J. S. Orcutt, J. M. Shainline, O. Tehar-zahav, Z. Sternberg, R. Meade, A. Popovi, and R. J. Ram, "Polycrystalline silicon ring resonator photodiodes in a bulk complementary metal-oxide-semiconductor process," *Opt. Lett.* **39**, 1061–1064 (2014).
  91. R. Dangel, J. Hofrichter, F. Horst, D. Jubin, A. La Porta, N. Meier, I. M. Soganci, J. Weiss, and B. J. Offrein, "Polymer waveguides for electro-optical integration in data centers and high-performance computers," *Opt. Express* **23**, 4736 (2015).
  92. Y. Ooka, N. A. B. Daud, T. Tetsumoto, and T. Tanabe, "Compact resonant electro-optic modulator using randomness of a photonic crystal waveguide," *Opt. Express* **24**, 11199–11207 (2016).
  93. Y. Taguchi, Y. Takahashi, Y. Sato, T. Asano, and S. Noda, "Statistical studies of photonic heterostructure nanocavities with an average Q factor of three million," *Opt. Express* **19**, 11916–11921 (2011).
  94. S. L. Portalupi, M. Galli, M. Belotti, L. C. Andreani, T. F. Krauss, and L. O'faolain, "Deliberate versus intrinsic disorder in photonic crystal nanocavities investigated by resonant light scattering," *Phys. Rev. B* **84**, 45423 (2011).
  95. T. Tanabe, K. Nishiguchi, E. Kuramochi, and M. Notomi, "Low power and fast electro-optic silicon modulator with lateral p-i-n embedded photonic crystal nanocavity," *Opt. Express* **17**, 22505–22513 (2009).
  96. H. C. Nguyen, Y. Sakai, M. Shinkawa, N. Ishikura, and T. Baba, "10 Gb/s operation of photonic crystal silicon optical modulators," *Opt. Express* **19**, 13000–13007 (2011).
  97. Y. Ooka, T. Tetsumoto, N. A. B. Daud, and T. Tanabe, "Ultrasmall in-plane photonic crystal demultiplexers fabricated with photolithography," *Opt. Express* **25**, 1521–1528 (2017).